Little Earth Experiment:A Journey Toward the Earth's Tangent Cylinder

Aujogue, Kelig

Award date:
2016

Awarding institution:
Coventry University

Little Earth Experiment: A Journey Toward the Earth's Tangent Cylinder

Aujogue, K.

COVENTRY UNIVERSITY

The Leverhulme Trust

LITTLE EARTH EXPERIMENT: A JOURNEY TOWARD THE EARTH'S TANGENT CYLINDER

Author	Supervisors	Reviewers
Kelig Aujogue	Prof. Alban Potherat	Dr. Henry-Claude Nataf
	Dr. Binod Sreenivasan	Dr. Graeme Sarson

Thesis submitted in fulfillment of the requirements for the degree Doctor of Philosophy

July 2016

Library Declaration and Deposit Agreement

Title:	**Forename:**	**Family Name:**
Student ID:	**Faculty:**	**Award:**
Thesis Title:		

Freedom of Information:

Freedom of Information Act 2000 (FOIA) ensures access to any information held by Coventry University, including theses, unless an exception or exceptional circumstances apply.

In the interest of scholarship, theses of the University are normally made freely available online in the Institutions Repository, immediately on deposit. You may wish to restrict access to your thesis for a period of up to three years. Reasons for restricting access to the electronic thesis should be derived from exemptions under FOIA.
(Please also refer to the University Regulations Section 8.12.5)

Do you wish to restrict access to thesis/submission:	Choose an item.
Please note: If your thesis includes your publications in the appendix, please ensure you seek approval from the publisher first, and include their approval with this form. If they have not given approval, they will need to be removed from the version of your thesis made available in the Institutional Repository.	
If Yes please specify reason for restriction:	
Length of restriction:	
Does any organisation, other than Coventry University, have an interest in the Intellectual Property Rights to your work?	Choose an item.
If Yes please specify Organisation:	
Please specify the nature of their interest:	
Signature:	**Date:**

For Postgraduate Research Support Unit (Registry) use	
Date Final Thesis Submitted	
Date of Thesis release to Library	

Declaration

The work presented in this dissertation depicts the research I conducted at Coventry University. I declare that the results are the product of my own investigation, except stated otherwise. I further certify that the material contained herein has not been substantially used in any other submission for an academic award or other qualification.

This thesis contains approximately 40000 words and 82 figures.

Abstract

This dissertation presents a theoretical contribution on the onset of rotating magneto-convection and a new experimental setup built to study the onset and the development of convection in the Earth Tangent Cylinder (TC). The theoretical contribution is a linear stability analysis of the onset of convection for an electrically conducting fluid in rotation and permeated by a magnetic field. This work highlighted the importance of the magnetic field as it enforces a specific mode of convection at onset for a certain range of parameters.The apparatus was designed to show for the first time experimentally the significant role played by the magnetic field on the flow structures and bring forward the first evidence of a polar vortex in the TC with a quantitative measurement technique such as particle image velocimetry (PIV). In order to reach these goals, the experimental setup consisted in an hemispherical dome filled with a transparent conducting fluid heated at the center, cooled on the outside and spun inside a high external magnetic field. The hemispherical dome is approximatively 30cm diameter. The fluid used is sulphuric acid at 30% mass concentration, because of its conductivity of approximatively 80S/m and its transparency, allowing both interactions with the magnetic field and visualization for PIV measurements. To compensate against the weak conductivity of sulphuric acid we used a unique 10T magnet. As a result, we were able to study the difference in the convective flow between the magnetic and non-magnetic case. It has been shown that convective structures under a magnetic field at onset become much larger leading to one off axis vortex. Above onset it has also been highlighted that this structure is maintained whereas without magnetic field the flow is very different between onset and developed convection. Indeed at the onset we observe numerous structures that coalesce into one large centered structure far from the onset of convection.

Acknowledgements

I am very grateful to Dr. Binod Sreenivasan and Prof. Alban Potherat for their support and guidance all along this project. Thanks to them I had the chance to conduct my research under the funding of the Leverhulme Trust which I am most grateful for. I have a special thought for the night shifts spent operating the experiment at the CNRS on several occasions and how Prof. Alban Potherat helped me through them, undoubtedly the most exciting and challenging moments of this project. Also, I am indebted to Mr. Ian Bates for his technical knowledge, support and advice that he kindly shared over the past four years.

I am very thankful to the CNRS in Grenoble (CRETA and LNCMI) for their welcome and their fantastic help when it was most needed. I would like to address a very special thank you to Dr. Francois Debray who made it possible for this project to come to a favorable end. I also thank Mr Nathaniel Baker for always keeping us with a smile whether his experiment or mine was being challenging.

Additionally, last but definitively not least, I am forever grateful to my beloved parents Mme Michelle Gouin and Mr Bernard Aujogue who started supporting me and believing in me long before the beginning of my PhD studies. Their trust in me and their own passions have played a significant inspiration to my own creativity and work. On a more recent note, I am grateful to my lovely wife Mrs Haley Allison Beer for sharing with me the last two years of this project and coping with me throughout the emotional roller coaster that the PhD can be. She managed to keep me focussed on the end goal when the time were uncertain.

Finally, I offer my regards to all of those not mentioned here but who were of kind support toward my completion.

Contents

List of Figures

Part I

Theoretical study

Chapter 1

Motivation and Theoretical background

1.1 Introduction

The work presented in thesis is a contribution to the Earth core study and more so the investigation of the Tangent Cylinder. The Earth interior is structured in several layers. From the surface to the center, we have the crust, the mantle and the core. The core is then divided in two specific regions: the solid part at the center and the liquid part on the outside. The liquid part of the Earth core is known to be the source of the Earth magnetic field. Indeed this part reveals strong convective motions as consequences of the compositional and thermal differences between the mantle and the solid part of the Earth core. These convective motions coupled with the Earth rotation are thought to be responsible for the generation of the Earth magnetic field. This process is known as the Geodynamo. Most of the Earth magnetic field is believed to be generated by convective structures known as the Busse's columns [14]. These columns correspond to helical structures parallel to the axis of rotation of the Earth and surrounding the solid part of the Earth core. Unfortunately, these structures are not sufficient to explain specific behaviour of the Earth magnetic field such as the Polar vortex and its drift or the magnetic reversal [36]. To

investigate the roots of this behaviour, it is necessary to focus on a different area of the liquid part of the Earth core: the Tangent Cylinder. The Tangent Cylinder corresponds to an imaginary cylinder defined by the axis of rotation of the Earth and the radius of the solid inner core. In this area, the liquid is confined differently. As a result, the Busse's column can not take place which leads to a very different organization of the flow with strong consequences on the Earth magnetic field within the polar region. The objective of the project is the experimental simulation of the onset of convection inside the Earth Tangent Cylinder, with a special emphasis on the Magnetohydrodynamic (MHD) aspect of the problem. Indeed this particular region is not well known. There are different practical reasons for this. First, most magnetic field is thought to be generated outside the Tangent Cylinder, directing research more towards this area of the Earth core [32]. Second, the Tangent Cylinder corresponds to regions (North and South poles) where measurements are very hard for technical reasons. On dry land, the weather conditions only allow a very limited amount of observatory to monitor of the magnetic field. In space, ballistics constraints lead most of the satellite to orbit only above the equator limiting the access to magnetic field data near the pole. Third, the Earth regimes are still very far from numerical and experimental reach. Indeed, the radius of the Earth core is so large that it is impossible to reproduce the non-dimensional parameters of the system in a laboratory experiment or in numerical simulation. Nevertheless we know certain key features of the Earth Tangent Cylinder thanks to previous studies. For example, we know that a typical feature of the Tangent cylinder is the polar vortex. The polar vortex corresponds to a large convective plume positioned off the Earth axis of rotation in the North pole and South pole areas. The evidences of the polar vortex were shown throughout magnetic field observation [36]. The Tangent

Cylinder was studied in a non-magnetic experiment [8]. Unfortunately, the authors of this study were not able to recover the polar vortex. On the other hand, later numerical simulations [56] were able to recreate the polar vortex and attribute it to a magnetic effect. Indeed in this second study, the authors showed that the presence of the magnetic field has significant consequences on the number of convective structures in the Tangent Cylinder leading to one large vortex. The motivation for the dissertation is to offer a new experimental contribution on the understanding of the Earth liquid core flow in the region of the Earth Tangent Cylinder by combining the effect of convection, rotation and magnetic field in the appropriate geometry. We aim to answer several questions:

- When does the onset of convection occur and how does it evolve above onset without magnetic field?
- What is the effect of the magnetic field on convective patterns at onset?
- Can we experimentally observe secondary instabilities taking place above the onset of convection with a magnetic field?
- What are the parameters to reproduce the polar vortex in our experimental configuration?
- How is the polar vortex affected by the intensity of the convection?
- What is the effect of the magnetic field on general feature such as the heat flux and the thermal wind in the system?

In order to address these pending issues, it is essential to understand the interplay between the flow and the magnetic field from the onset to supercritical regimes of convection. The problem of the rotating magnetoconvection inside

the Tangent Cylinder is usually approached theoretically as a planar rotating magnetoconvection problem to simplify its formalism [43, 19, 10]. Unfortunately, this approach neglects the curvature of the real geometry and the confinement due to the Tangent Cylinder. In this thesis, we present a new experimental approach to study the Tangent Cylinder. This dissertation describes in the present chapter the theoretical corner stones of the project. The second chapter presents a theoretical approach of the onset of convection in plane layer geometry for low Ekman number. The third chapter introduces the experimental apparatus built over the course of the project. The fourth chapter focusses on the experimental results and their contributions from a general MHD perspective. The fifth chapter examines the results under the geophysical scope. Finally, the sixth chapter concludes this work. In the present chapter, we first introduce the Geophysical aspects of the problem by presenting the Earth general structure and the properties of the Earth Core. Then, we discuss the mathematical formalism used to model the Earth liquid core by introducing the equations governing the Fluid motion, Electromagnetism and Thermal energy. Then, we relate the MHD side of the project to the Geophysical one. In order to do so we present the state of the art for the development of the Geodynamo model, the theoretical study of the onset of rotating magnetoconvection and experimental work applied to the Earth Tangent Cylinder. Finally we conclude this chapter and highlight the different gaps in the literature that justify the need for a new experiment.

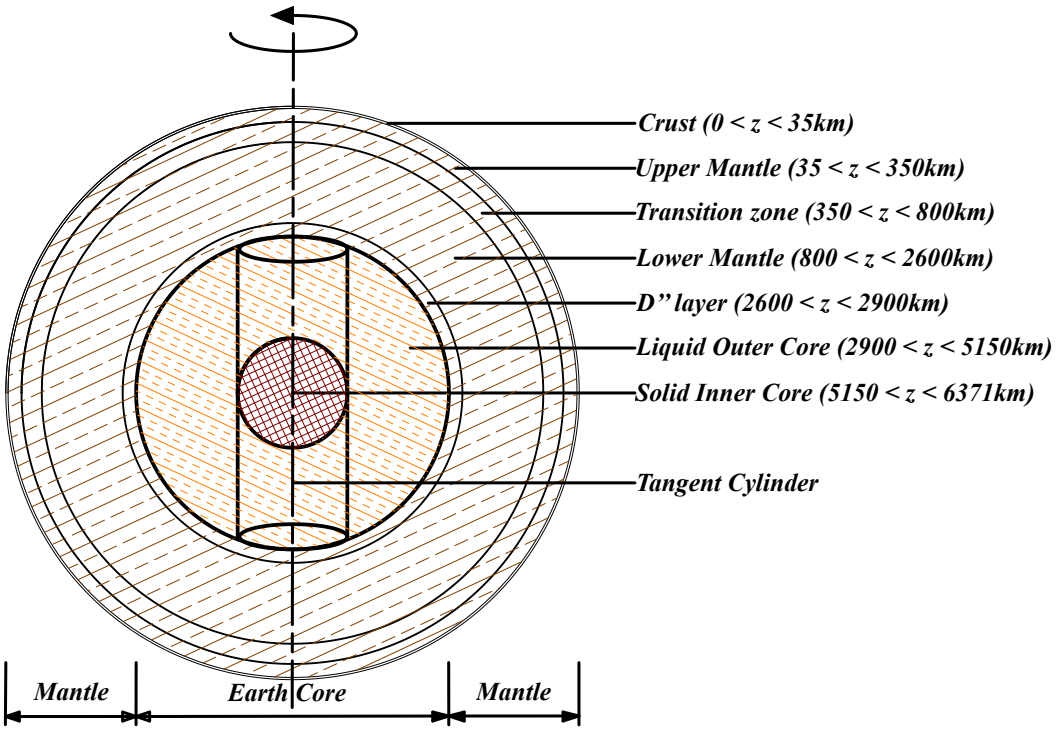

Figure 1.1: Schematic of the Earth internal structure.

1.2 Geophysical Background: from the Crust to the Core.

1.2.1 Earth's Interior

The Earth's structure can be approximated as a multilayered sphere. The knowledge of its structure has been extracted from seismology studies. Indeed the refractions of pressure and shear waves generated by Earthquakes are used to investigate the interior of the Earth [41]. There are 3 main regions from the surface to the center: the crust, the mantle and the core. Each of these regions can then be again divided in subregions as illustrated with figure 1.1. The crustal shell is the most superficial layer in the Earth structure. It is divided in two different types: the continental crust and the oceanic crust.

The first one is around 35 km thick in average. The latter is around 7 km thick. Although the age of the crust isn't uniform, study showed that this layer was present already 4.4 billions years ago [61]. The crust doesn't play any role into the generation of the Earth magnetic field. Nevertheless, the crustal magnetic field is critical to the measurement of the magnetic field at the Earth surface. Indeed, some magnetic anomalies exist that are of the same order of magnitude as the main field generated by the geodynamo [42].

Underneath the Crust is the Mantle. It is 2900 km deep. This layer is characterized by important variation in composition. This has led scientists to commonly distinguish four different sublayers: the Upper Mantle (35 km to 350 km), the Transition zone (350 km to 800 km), the Lower Mantle (800 km to 2600 km) and the D" layer (2600 km to 2900 km). The D" layer plays a determining role in the Core/Mantle coupling. The nature of the coupling is of three types: Topographic, Electromagnetic and Thermal. Finally, the Earth core extends from 2900 km to 6371 km, the center of the Earth.

1.2.2 Physical properties and division of the Core

The Core is subdivided in two areas: the outer core and the inner core. The inner core is a solid. Its boundary with the outer core lies at a depth of 5150 km. The outer core is liquid, mostly made of iron alloys. The motion of this electrically conducting fluid is the main source of the Earth magnetic field. It originates from a balance (MAC balance) between the Coriolis force due to the Earth rotation, the Lorentz force (magnetic forces) and the buoyancy forces (compositional and thermal variations along the radius). The geometry of the outer core naturally divides it in two parts: within the Tangent Cylinder (TC) and outside the TC. The TC corresponds to an imaginary cylinder of axis the Earth's rotation axis and radius the Earth inner core radius. Outside the

Parameters	Notation	Earth core value
Inner core radius	$r_i[m]$	1.22×10^6
Outer core thickness	$d[m]$	2.26×10^6
Outer core mean density	$\rho[kg/m^{-3}]$	1.09×10^4
Inner core mean density	$\rho_i[kg/m^{-3}]$	1.29×10^4
Rotation rate	$\Omega[rad/s]$	10^{-2}
Thermal diffusivity	$\kappa[m^2/s]$	$5 \pm 3 \times 10^{-6}$
Outer core's kinematic viscosity	$\nu[m^2/s]$	$10^{-5\pm2}$
Inner core's kinematic viscosity	$\nu_i[m^2/s]$	$10^{10\pm3}$
Electrical conductivity	$\sigma[S/m]$	$5 \pm 2 \times 10^5$
Magnetic diffusivity	$\eta[m^2/s]$	1.5 ± 0.5

Table 1.1: Physical properties in the Earth core

TC, the MAC balance generates columnar motion in the outer core parallel to the axis of rotation known as Busse's columns. Inside the TC, the symmetry is broken by the solid inner core. Hence the flow behaves differently in that region. With table 1.1 we summarize the main characteristics of the Earth core following [44].

1.3 From Electromagnetism to Magnetohydrodynamics

The Geodynamo can be modelled with magnetohydrodynamics (MHD). Magnetohydrodynamics is at the crossroad between electromagnetism and hydro-

dynamics. In other words, this is the study of conducting fluid dynamics. In this section, we present the main laws of electromagnetism leading to the induction equation and the governing law of fluid dynamic.

1.3.1 Governing laws of Electromagnetism

1.3.1.1 Maxwell's laws and Ohm's law

In MHD, the movement of a conducting fluid is modelled with the help of Maxwell's equations of electromagnetism and Ohm's law. There are 4 laws from Maxwell:

1. Gauss' law:

$$\boldsymbol{\nabla} \cdot \mathbf{E} = \frac{\rho_e}{\epsilon_0} \tag{1.1}$$

2. The solenoidal nature of B:

$$\boldsymbol{\nabla} \cdot \mathbf{B} = 0 \tag{1.2}$$

3. Faraday's law:

$$\boldsymbol{\nabla} \times \mathbf{E} = -\frac{\partial \mathbf{B}}{\partial t} \tag{1.3}$$

4. Post-Maxwell-Ampère's law:

$$\boldsymbol{\nabla} \times \mathbf{B} = \mu_0 \mathbf{J} + \mu_0 \epsilon_0 \frac{\partial \mathbf{E}}{\partial t} \tag{1.4}$$

5. Ampère's law:

$$\boldsymbol{\nabla} \times \mathbf{B} = \mu_0 \mathbf{J} \tag{1.5}$$

where $\mathbf{E}$ is the electric field, ρ_e is the electric charge density, ϵ_0 is the permittivity of free space, $\mathbf{B}$ is the magnetic field, μ_0 is the permeability of vaccum

and $\mathbf{J}$ is the density of current. We note here that following Davidson [25], we can neglect the last term in equation 1.4 and write it as equation 1.5. We note that by applying the divergence operator on Ampère's law we obtain: $\boldsymbol{\nabla} \cdot \mathbf{J} = 0$. It represents the conservation of current. Besides, it appears that Maxwell's equations are an open system. Therefore they require an additional equation for the density of current: Ohm's law. It is given by:

$$\mathbf{J} = \sigma(\mathbf{E} + \mathbf{u} \times \mathbf{B})$$

with σ the electric conductivity and $\mathbf{u}$ the velocity of the fluid.

1.3.1.2 The Lorentz Force

An essential part of the coupling between electromagnetism and the velocity field is the Lorentz force. It represents the action of a magnetic field in a conducting fluid due to the electric current density flowing inside it. The Lorentz force is a volume force. It can be written as:

$$F_{Lorentz} = \mathbf{J} \times \mathbf{B}$$

1.3.1.3 Induction equation

Finally, we shall introduce the induction equation. It expresses the time evolution of a magnetic field advected by a velocity field and diffused. To derive it, one can take the curl of $\mathbf{E}$ from Ohm's law and replace it into Faraday's law (1.3) with $\mathbf{J}$ expressed with Ampère's law (1.5). Hence it yields to:

$$\frac{\partial \mathbf{B}}{\partial t} = \boldsymbol{\nabla} \times (\mathbf{u} \times \mathbf{B}) + \eta \nabla^2 \mathbf{B}, \tag{1.6}$$

when σ and η are constant and with $\eta = \frac{1}{\sigma \mu_0}$ the magnetic diffusivity.

1.3.2 Governing laws of Fluid Mechanics

The fluid mechanics is commonly described by the Navier-Stokes equation (NS). This model is based on two main assumptions: the fluid is a continuous medium and the fields of interest (density, velocity, temperature...) are C^2 differentiable. NS model is derived by applying the conservation principles (momentum and mass) to an arbitrary fluid parcel through time and space with the Reynolds transport theorem. We can write for the conservation of mass:

$$\frac{d}{dt}\int_{\Pi(t)} \rho(\mathbf{x},t)dV = \int_{\Pi(t)} (\frac{d}{dt}\rho(\mathbf{x},t) + \rho(\mathbf{x},t)\boldsymbol{\nabla}\cdot\mathbf{u}(\mathbf{x},t))dV = 0, \tag{1.7}$$

where $\mathbf{x}$ are the space coordinates, t is the time, $\mathbf{u}(\mathbf{x},t)$ is the velocity, $\rho(\mathbf{x},t)$ is the mass density and the $\Pi(t)$ is the volume of the fluid parcel considered. Using the chain rules the total derivative is written:

$$\frac{d}{dt}\rho(\mathbf{x},t) = \frac{\partial\rho(\mathbf{x},t)}{\partial t} + \mathbf{u}(\mathbf{x},t)\cdot\boldsymbol{\nabla}\rho(\mathbf{x},t). \tag{1.8}$$

By keeping in mind that: $\mathbf{u}(\mathbf{x},t)\cdot\boldsymbol{\nabla}\rho(\mathbf{x},t)+\rho(\mathbf{x},t)\boldsymbol{\nabla}\cdot\mathbf{u}(\mathbf{x},t) = \boldsymbol{\nabla}\cdot(\rho(\mathbf{x},t)\mathbf{u}(\mathbf{x},t))$, and that equation (1.7) is valid for any volume Π, we can rewrite the integral formulation locally as:

$$\frac{\partial\rho(\mathbf{x},t)}{\partial t} + \boldsymbol{\nabla}\cdot(\rho(\mathbf{x},t)\mathbf{u}(\mathbf{x},t)) = 0. \tag{1.9}$$

With equation (1.9) we appreciate the consequence of assuming the fluid to be incompressible then ρ becomes a constant. Hence the continuity equation for

incompressible flows takes the following simple form:

$$\boldsymbol{\nabla} \cdot \mathbf{u} = 0. \tag{1.10}$$

For the conservation of momentum, we apply Newton's second law to the mass flux, *i.e.* $\rho\mathbf{u}$. This gives us the following expression:

$$\frac{d}{dt}\int_{\Pi(t)} \rho(\mathbf{x},t)\mathbf{u}dV = \mathbf{F}_{ext}, \tag{1.11}$$

with $\mathbf{F}_{ext}$ the external force applied on the flow. The external forces are divided in two different kind:

1. the surface forces, that are usually expressed throughout the stress tensor

2. the volume forces, such as Buoyancy, Lorentz force or gravity.

They can be expressed as:

$$\mathbf{F}_{ext} = \int_{\Pi} \mathbf{F}_{vol}dV + \oint_{\partial\Pi} \xi dS, \tag{1.12}$$

with ξ the stress tensor and $\mathbf{F}_{vol}$ the volume forces. In our study we are working with an incompressible Newtonian fluid, hence the stress tenor takes the form:

$$\xi = \rho\nu(\boldsymbol{\nabla}\mathbf{u} + (\boldsymbol{\nabla}\mathbf{u})^T) - p\mathbb{1}, \tag{1.13}$$

where $\mathbb{1}$ is the identity matrix, ν is the kinematic viscosity and p is the pressure. Finally by reformulating the time derivative in equation (1.11), using Gauss' divergence theorem in (1.12), replacing ξ with (1.13) and considering ν as

constant, we can write the classic form of the Navier-Stokes equation:

$$\rho(\frac{\partial \mathbf{u}}{\partial t} + \mathbf{u} \cdot \boldsymbol{\nabla}\mathbf{u}) = -\boldsymbol{\nabla}p + \rho\nu\nabla^2\mathbf{u} + \mathbf{F}_{vol}. \tag{1.14}$$

Eqs. (1.10) and (1.14) are the equations governing incompressible flows in general. In our case F_{vol} will be the sum of the Coriolis force, the buoyant force and the Lorentz force.

1.3.3 The Boussinesq approximation

To finish the section on the basics of the models, we address the case of the Boussinesq approximation as we are using it to describes the buoyancy forces [11]. The Boussinesq approximation is an elegant and robust idea in the limits of incompressible flows. It models the differences in density by neglecting their effect on inertia, focussing on the terms that are gravitationally controlled. In other words, the density difference only appears when the density is multiplied by the gravitational constant. The density is then expressed as:

$$\rho = \rho_0(1 + \alpha\Delta T). \tag{1.15}$$

By considering an external gravity force $F = \mathbf{g}\rho$, the Boussinesq approximation adds a new term to the Navier-Stokes equation. This term is given as:

$$F_{Boussinesq} = -\mathbf{g}\rho\alpha\Delta T. \tag{1.16}$$

1.4 From Geodynamo to the Earth Tangent Cylinder: State of the art

1.4.1 Full Magnetohydrodynamic model for Geodynamo

The Geodynamo has been an ongoing problem for more than a century now. It was only thirteen years after the first evidence of the liquid core existence that Joseph Larmor suggested that the Earth magnetic field origin might lie in a dynamo mechanism taking place within the Core. Later in 1946 and based on theoretical assumption, Walter M. Elsasser was able to establish an order of magnitude for the intensity of the flow in the Earth core required to sustain the geodynamo. Thanks to George Backus, who proved the existence of a mean flow compensating the Ohmic losses in the core, and to Raymond Hide and Paul Roberts who developed kinematic dynamo models, the theory was well established by the sixties. It is now accepted that the action of the magnetic field on the liquid outer core induces currents and that these currents produce the magnetic field. According to Hide and Roberts [34] and Braginsky and Roberts [12], the equations governing the geodynamo mechanism can be approximated as:

$$\rho(\frac{\partial \mathbf{u}}{\partial t} + (\mathbf{u}\cdot\boldsymbol{\nabla})\mathbf{u}) + 2\rho\boldsymbol{\Omega}\times\mathbf{u} = -\boldsymbol{\nabla}p - \alpha\rho g T\mathbf{r} + \mathbf{J}\times\mathbf{B} + \rho\nu\nabla^2\mathbf{u}, \quad (1.17)$$

$$\frac{\partial \mathbf{B}}{\partial t} = \boldsymbol{\nabla}\times(\mathbf{u}\times\mathbf{B}) + \eta\nabla^2\mathbf{B}, \quad (1.18)$$

$$\frac{\partial T}{\partial t} + (\mathbf{u} \cdot \boldsymbol{\nabla})T = \kappa \nabla^2 T, \tag{1.19}$$

$$\boldsymbol{\nabla} \cdot \mathbf{u} = 0, \tag{1.20}$$

$$\boldsymbol{\nabla} \cdot \mathbf{B} = 0, \tag{1.21}$$

where $\boldsymbol{\Omega}$ is the rotation, $\mathbf{g} = g\mathbf{r}$ with g the gravitational constant, $\mathbf{r}$ is the position vector, T is the total temperature and κ is the thermal diffusivity of the fluid in the core. We note that this model consists of the Navier-Stokes equation, coupled with the induction equation, and the energy equation. The energy equation (1.19) models the advection and the diffusion of the temperature field in time. It is important to point out the Coriolis term appearing in the momentum equation (1.17): $2\rho\boldsymbol{\Omega} \times \mathbf{u}$ is a consequence of the rotation. We also remark that the compositional buoyancy is not represented in this model. Although it is an active part of the Earth core buoyancy mechanism, the present model only takes into account the thermal buoyancy. Now we can normalize eqs. (1.17-1.21) with reference to lengths d, velocity η/d, pressure $\rho\eta\Omega$, magnetic field B_0, time d^2/η, temperature ΔT and rotation speed Ω. By doing so, we obtain the five non-dimensional number which control the model. They are the following:

- $E = \nu/d^2\Omega$, the Ekman number characterizing the ratio of the viscous force over the Coriolis force.

- $Ra = g\alpha\Delta T d/\eta\Omega$, the modified Rayleigh number typically used in geodynamo and corresponding to the ratio of the buoyancy force over diffusion.

Parameters	Earth core value
E	10^{-15}
Ra	1240
Λ	$[0.1 - 1]$
Pr	10^{-2}
Pm	10^{-8}

Table 1.2: Non-dimensional number in the Earth core following the value given in [56]

where Ra is the modified Rayleigh number.

- $\Lambda = B^2/\mu_0\eta\rho\Omega$, the Elsasser number characterizing the ratio of the Lorentz force to the Coriolis force.
- $Pr = \nu/\kappa$, the Prandtl number which is the ratio of the viscous diffusivity over the thermal diffusivity.
- $Pm = \nu/\eta$, the magnetic Prandtl number which is the ratio of the viscous diffusivity over the magnetic diffusivity.

With the Table 1.2, we gave the non-dimensional number range for the Earth core following [56]. Taking the normalization into account, the equations in their non-dimensional form are:

$$Pm^{-1}E(\frac{\partial \mathbf{u}}{\partial t}+(\mathbf{u}\cdot\boldsymbol{\nabla})\mathbf{u})+2\hat{\mathbf{z}}\times\mathbf{u} = -\boldsymbol{\nabla}p+RaT\hat{\mathbf{z}}+\Lambda(\boldsymbol{\nabla}\times\mathbf{B})\times\mathbf{B}+E\nabla^2\mathbf{u}, \quad (1.22)$$

$$\frac{\partial \mathbf{B}}{\partial t} = \boldsymbol{\nabla}\times(\mathbf{u}\times\mathbf{B}) + \nabla^2\mathbf{B}, \quad (1.23)$$

$$\frac{\partial T}{\partial t} + (\mathbf{u} \cdot \boldsymbol{\nabla})T = PmPr^{-1}\nabla^2 T, \tag{1.24}$$

$$\boldsymbol{\nabla} \cdot \mathbf{u} = 0, \tag{1.25}$$

$$\boldsymbol{\nabla} \cdot \mathbf{B} = 0, \tag{1.26}$$

In the present work, we are interested in 3 different kinds of boundary conditions:

- Stress Free Magnetic (SFM, conditions (1.27)– (1.30) below).
- No-Slip Magnetic electrically insulated (NSM, conditions (1.29)– (1.31) below)
- No-Slip electrically perfectly Conducting (NSC, conditions (1.30)– (1.32) below)

These are given respectively for $z = \pm 1/2$ in the case of two infinite horizontal planes as:

$$u_z = 0 \quad \text{(impermeability)}, \tag{1.27}$$

$$\frac{d^2 u_z}{dz^2} = 0 \quad \text{(stress-free)}, \tag{1.28}$$

$$(\boldsymbol{\nabla} \times \mathbf{B}).\mathbf{e_z} = 0 \quad \text{(electrically insulating)}, \tag{1.29}$$

$$T(z = -1/2) = 1,\ T(z = +1/2) = 0, \tag{1.30}$$

$$\mathbf{u} = 0 \quad \text{(no-slip)}. \tag{1.31}$$

$$\frac{d(\boldsymbol{\nabla} \times \mathbf{B})}{dz}.\mathbf{e_z} = 0 \quad \text{(electrically perfectly conducting)}, \tag{1.32}$$

In our experimental apparatus the boundaries correspond to the materials: glass and ceramic. They can be considered as insulating, indeed their electrical conductivity is of the order of 10^{-14} S/m whereas the conductivity of the electrolyte we use in of the order 1 S/m. The velocity of the flow at the interface with the boundaries is the same as the velocity of the boundaries. Therefore we consider that the experiment follows a no-slip electrically insulated case with fixed temperature. Fixed heat flux would be the other obvious boundary condition but its relevance to the experimental setup would have required a different design. Although experimentally we only model the no-slip insulated case, we compare theoretically the effect of the boundary condition on the onset of rotating magnetoconvection. It is necessary as the Earth core is unlikely to be perfectly insulating. Indeed, we can easily envisage that neither the Earth solid inner core nor the Mantle are perfectly insulating.

1.4.2 Towards the onset of rotating magnetoconvection

In the scope of this dissertation, we are interested in the onset of rotating magnetoconvection in the Earth TC. We approach the problem with a theoretical and experimental angle. To simplify the theoretical problem, studies are often considering the onset of rotating magnetoconvection in plane layer geometry. This type of study have been motivated either by geophysical or engineering applications involving liquid metals [13, 15, 23, 35, 59, 60, 62]. A number of geophysically motivated studies focused on the dynamics outside the TC: an

early study [30] derived theoretical scalings for the critical Rayleigh number and wave number at the onset of convection as a function of the magnetic field intensity and magnitude of the Coriolis force. Other studies [14, 15, 17] showed experimentally and theoretically that, in this region convection and rotation generated tall columns parallel to the rotation axis. A recent study investigated the role of a dipolar magnetic field in enhancing helicity in convection columns [57], which can explain subcritical behaviour as well as the preference for the axial dipole in rapidly rotating dynamos. These studies, however, do not consider the particularities of the TC, which, though imaginary, acts somewhat as a physical boundary because the presence of the solid inner core makes overcoming the Taylor-Proudman constraint more difficult. When convection does set in, motions vary strongly along z as heat and composition fluxes have a substantial component in the z-direction. As a first approximation we considered that the curvature of the top and the bottom boundaries are not expected to play a lead role, at least at the onset of convection. On these grounds, a simple plane geometry is expected to provide a fair, albeit simplistic, representation of the TC. In the plane geometry, it was theorised by Chandrasekhar [19], Podvigina [47] and experimentally observed by Nakagawa [43] that the convection could set off through an instability either of a magnetic or a viscous mode, depending on the values of the Ekman number (Viscous to Coriolis forces) and of the Elsasser number (Lorentz to Coriolis forces). While the magnetic mode has a low horizontal wavenumber, the viscous mode is characterised by thin structures of high horizontal wavenumber parallel to the rotation axis. One would expect the convective flows driven by these two mechanisms to differ significantly. These studies showed that transition between these modes resulted in a change in the wavelength of the observed convective patterns, but concerned only large values of E ($> 10^{-5}$).

Such values may be too far from the asymptotic regimes relevant to the Earth's core ($E \sim 10^{-15}$) to be applicable to it.

1.4.3 Linear stability in plane layer geometry

Inspired by [19], we shall address in chapter two the theoretical aspects of the onset of rotating magnetoconvection numerically. The theoretical approach was conducted by applying a linear stability analysis of the set of equations [1.22, 1.23, 1.24, 1.25 and 1.26]. The general idea is to linearize the equations, to introduce an infinitesimal perturbation in the system and to observe if the perturbation is strong enough to bring the flow to a new state. In the present case, we use this method to derive the value of the Rayleigh number at which the onset of the convection occurs. The problem between 2 infinite planes becomes invariant in the x and y directions and allows us to decompose all physical quantities as $f(z,t) = g_0 + \hat{f}(z)e^{i\mathbf{a}.\mathbf{r}_\perp + \sigma t}$, where $\mathbf{r}_\perp = (x,y)$, $\mathbf{a}$ is the wave number and σ is the growth rate. For all sets of boundary conditions, the system has a simple basic state solution whose linear stability we are interested in. This system is as follows:

$$\mathbf{u} = 0, \tag{1.33}$$

$$T(z) = \frac{1}{2} - z, \tag{1.34}$$

$$\mathbf{B} = B_0 \mathbf{e_z}, \tag{1.35}$$

The perturbation equations are given by:

$$E(D^2 - a^2 + Pm^{-1}\sigma_i)\hat{\omega_z} + 2D\hat{u_z} + \Lambda D\hat{j_z} = 0, \tag{1.36}$$

$$E((D^2 - a^2)^2 + Pm^{-1}\sigma_i)\hat{u_z} - 2D\hat{\omega_z} + \Lambda(D^2 - a^2)D\hat{b_z} - a^2Ra\hat{T'} = 0, \tag{1.37}$$

$$(D^2 - a^2 + \sigma_i)\hat{b_z} + D\hat{u_z} = 0, \tag{1.38}$$

$$(D^2 - a^2 + \sigma_i)\hat{j_z} + D\hat{\omega_z} = 0, \tag{1.39}$$

$$(PmPr^{-1}(D^2 - a^2) + \sigma_i)\hat{T'} + \hat{u_z} = 0. \tag{1.40}$$

Here D is the derivative along $\mathbf{z}$, σ_i is the imaginary part of σ, $\hat{\omega_z}$, $\hat{u_z}$, $\hat{j_z}$ and $\hat{b_z}$ are the z-components of the vorticity, velocity, electric current and magnetic field perturbations and $\hat{T'}$ is the temperature perturbation. The nondimensional wave number is denoted by $a = \| \mathbf{a} \|$. Eq. (1.36) is obtained from $\boldsymbol{\nabla} \times (1.22) \cdot \mathbf{e_z}$, (1.37) from $\boldsymbol{\nabla} \times [\boldsymbol{\nabla} \times (1.22)] \cdot \mathbf{e_z}$, (1.38) from $(\boldsymbol{\nabla} \times (1.23)).\mathbf{e_z}$, (1.39) as $\boldsymbol{\nabla} \times [\boldsymbol{\nabla} \times (1.23)] \cdot \mathbf{e_z}$ and Eq. (1.40) follows from Eq. (1.24).The boundary conditions (1.27)–(1.31) take the form:

$$D^2\hat{u_z} = \hat{u_z} = D\hat{\omega_z} = \hat{j_z} = \hat{T'} = 0 \quad \text{for} \quad z = \pm 1/2, \quad \text{(SFM)} \tag{1.41}$$

$$D\hat{u_z} = \hat{u_z} = \hat{\omega_z} = \hat{j_z} = \hat{T'} = 0 \quad \text{for} \quad z = \pm 1/2\,. \quad \text{(NSM)} \tag{1.42}$$

$$D\hat{u_z} = \hat{u_z} = \hat{\omega_z} = D\hat{j_z} = \hat{T'} = 0 \quad \text{for} \quad z = \pm 1/2\,. \quad \text{(NSC)} \tag{1.43}$$

With the linear analysis, Chandrasekhar [19] was able to show that two different modes can appear at the onset of convection in magnetorotation. These two modes are the viscous and the magnetic modes. The viscous mode is ruled by the rotation rate whereas the magnetic one is controlled by the magnetic field. These two modes are known to be drastically different. The transition has been observed in plane layer experiment. Nevertheless the question remains for the tangent cylinder: is the convection controlled by rotation or mainly by the magnetic field ?

1.4.4 Earth deep interior Experiments

In this section, we give an historical overview of the previous experimental setup leading to our study. Schematically, the literature is divided in 4 groups:

1. The Rayleigh Bénard Convection
2. The magnetic Rayleigh Bénard Convection
3. The rotating Rayleigh Bénard Convection
4. The magnetic Rayleigh Bénard Convection in rotation.

The Rayleigh Bénard Convection has been studied for a long time, with studies focussing on the scaling of the Nusselt number (between heat transfer and convection) in laminar and turbulent convection and the effect of the Prandtl number [18],[39],[20],[23]. The effect of the magnetic field has been investigated for non-rotating convection. The main effect concerns the onset of convection which is delayed compared to the non-magnetic onset. In other words, for non-rotating convection a vertical magnetic field has a stabilizing effect [43]. The effect of the rotation on the convection and its consequences have also been studied intensively. For instance in this dissertation, we will often be referring

to the work of Zhong *et al.* [64] and Goldstein *et al.* [33]. In these experimental and theoretical studies, the authors focussed on a rotating cylinder. In contrary to [43] and [10] where a relatively shallow plane was used, [64] looked at the effect of cylinder with an aspect ratio of one. In addition to the effect of aspect ratio of the cylinder, [64] and [33] were interested in the shape and the origins of the convective mode from onset and beyond. At onset they distinguished two types of modes "fast" and "slow". The fast modes arise from the sides of the cylinder whereas the slow modes appear at the center of the cylinder. These studies point out that for an aspect ratio comparable to the Tangent Cylinder, the plane layer geometry approximation is questionable. Nevertheless, these experiments show consistent results with the Taylor-Proudman theorem which is a direct consequence of rotation and inhibits convective motion. For an incompressible fluid in rotation around the vertical axis, the Taylor-Proudman theorem is given as:

$$\Omega_z \frac{\partial \mathbf{u}}{\partial z} = 0. \tag{1.44}$$

This implies that the convective structures in rotation need to be parallel to the axis of rotation. The precise case of the TC has been also investigated in non-magnetic circumstances Aurnou *et al.* [8]. In this study, the author investigated the flow inside an hemispherical dome filled with water, cooled on the outside, heated up on the inside and spun around the vertical axis. The flow motion was tracked with dye. This qualitative study exhibits the onset of rotating convection predicted by [19] and three types of flows above onset: helical plumes at the lateral boundary of the tangent cylinder, helical plumes throughout the tangent cylinder and fully three-dimensional convection. Although this study only gives a partial picture on the flow by neglecting the Lorentz force, it represents an undeniable precursor to the work presented in

this dissertation. For rotating magnetoconvection, the literature is much thinner. Indeed three main works have been conducted in relation with the TC: Aurnou & Olson [10], Nakagawa *et al.* [43] and King & Aurnou [38]. The third study is dedicated to turbulent regime in a cylindrical geometry with liquid metal. Nevertheless the authors operate in similar regimes of parameters. The two other studies highlight the change in convective structure size induced by the presence of a magnetic field. They also show the behavior of the heat transfer above onset with respect to the magnetic field intensity and the rotation rate. Nevertheless the Tangent cylinder, by its aspect ratio and its curvature, can not be reduced exclusively to a plane layer. By building an experiment that respects the geometry and the interplay between Lorentz force, Coriolis force and buoyancy force, we wish to finally address the question about the nature of the convection in the tangent cylinder.

1.5 Conclusion

In this chapter, we presented the motivation and the structure of this dissertation. We introduced the background of the project with the basic of Geophysics, Electromagnetism and Hydrodynamics. Additionally, we pointed out the model used in Geodynamo [56] and in our experiment and we gave an overview of the literature on the TC studies.

Chapter 2

Theory: Onset of plane layer magnetoconvection

2.1 Introduction

In this Chapter, we present the theory attached to the onset of plane-layer convection governed by the interplay between the magnetic (Lorentz), buoyancy and Coriolis forces. Our objective is to provide a description of the driving mechanism for the convection in the tangent cylinder (TC) region of the Earth's liquid core. In this region, it is considered that intense convection, compositional and thermal, takes place affecting the structure of the magnetic field near the poles [56]. The convective structures in the TC are affected by the Earth's self-generated magnetic field resulting in a strong anticyclonic polar vortices that show up in the secular variation of the geomagnetic field [55]. Our first objective in this chapter is to find out whether the onset of convection is sensitive to the Lorentz force in the regime of strong rotation that characterises the Earth.

There have been experimental studies applicable to the dynamics of the TC for $E = 10^{-4}$[10, 8], but only the viscous mode of convection could be

observed. The link between plane layer magnetoconvection and convection in the Earth's TC was first established by linear onset calculations as well as numerical simulations of the geodynamo [55, 56], where substantial thickening of buoyant plumes under the effect of the magnetic field was noted, albeit at values of E down to 10^{-4} only. Crucially, these studies showed that non-axisymmetric, Earth-like polar vortices are obtained only through the action of the magnetic field.

In this study, we look at plane-layer magnetoconvection at values of E low enough to reach asymptotic regimes [29, 27]. We precisely determine the range of parameters in which these asymptotics become accurate. Although actual regimes of the TC remain beyond the reach of this analysis, asymptotic scalings are relevant to it. In the same spirit, we shall characterise the consequence of using either a no-slip boundary condition or its less computationally demanding stress-free counterpart on these regimes.

Finally, we present an adapted model integrating the potential variation of thermal diffusivity and electrical conductivity. By implementing the variations known for the Earth and for Sulphuric acid, we demonstrate the robustness of the theoretical results to realistic systems.

This Chapter is organized in three distinct sections: the classical model for the Geodynamo, a non-classical model with variable diffusivities, and the discussion. The first section is a contribution of the problem of convection onset for incompressible conducting fluid in the rotating frame. Therefore, it is described by the full incompressible magnetohydrodynamic equations. The second section presents a more elaborate model taking into account the effect of temperature variation on the electrical conductivity and the thermal diffusivity. The objectives are:

1. Recover scaling laws at low Ekman number for the onset of magnetocon-

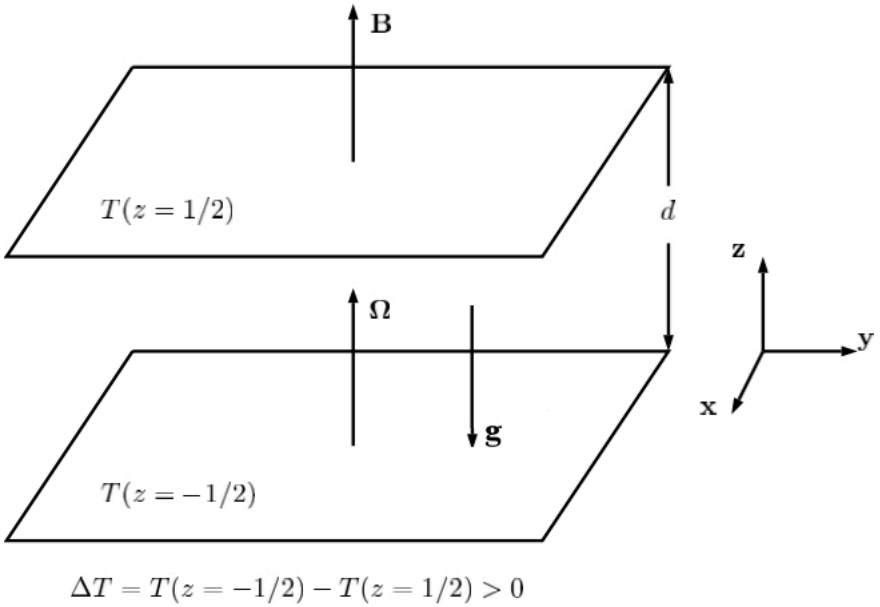

Figure 2.1: Schematic of the plane layer magnetoconvection problem

vection.

2. Address the question of the overstability

3. Develop and study an inhomogeneous model to test the influence of variable conductivities that occurs in experiments.

Finally, we conclude this chapter in a third section.

2.2 Classical Model for Geodynamo

2.2.1 Problem and Geometry

With Figure 2.1, we illustrate the geometry which we solve the perturbation equations [1.36-1.40]. Following Sreenivasan & Jones [56], we shall only seek the shape of the unstable modes, not their growth rate. However, at this stage we shall not exclude oscillatory modes in order to determine the precise conditions of their appearance. The problem becomes a generalized eigenvalue

problem of the form $A(\sigma_i)\mathbf{X} = Ra B\mathbf{X}$, where σ_i is treated as a parameter, A and B are matrices and $\mathbf{X}$ is a vector. The critical Rayleigh number for the onset of convection $Ra_c(\sigma_i)$ is found as an eigenvalue for any given a and minimised over a as in [19]. When the marginal mode is not oscillatory, the critical Rayleigh number is found by setting $\sigma_i = 0$ in Eqs. (1.36) − (1.40). In this case, with help of a formal transformation of $\hat{T}'$ into $\hat{T}'_m = Pm Pr^{-1}\hat{T}'$ and $Ra = Pr Pm^{-1} Ra$, the solution is made independent of the magnetic and thermal diffusivities. The results presented thereafter on the stability of non-oscillatory modes therefore extend to arbitrary values of Pm and Pr. The non-oscillatory modes are also referred to as steady modes [50].

2.2.2 Numerical method

Eqs. (1.36)−(1.40) were solved numerically using a spectral collocation method based on Chebyshev polynomials [53]. In the no-slip case, a boundary layer of thickness $\delta = 2\sqrt{E\pi}$ develops along the walls [1], and therefore we ensured that at least 3 collocations points were in it. Some convergence tests were performed to ensure that the resolution is adequate. The results for $\sigma_i = 0$ are presented in Figure 2.2, where we varied the number of collocations points N between 5 to 3000. In the SFM case, the tests were performed for $\Lambda = 1, \quad E = 10^{-9} \quad$ and $\quad a = 3.149$. NSM and NSC conditions were tested with $\Lambda = 1, \quad E = 10^{-7} \quad$ and $\quad a = 3.333$. We chose these parameters to ensure a good convergence at the lowest E we investigated. We looked at the value of the error ϵ on Ra_c relative to its value obtained for $N = 3000$. For both types of boundary conditions, $N > 100$ gives a small relative error. On the basis of this test, the results presented in the next section have been obtained with $N = 600$ for the SFM case, $N = 1200$ for the NSM case and $N = 1000$ for the NSC case.

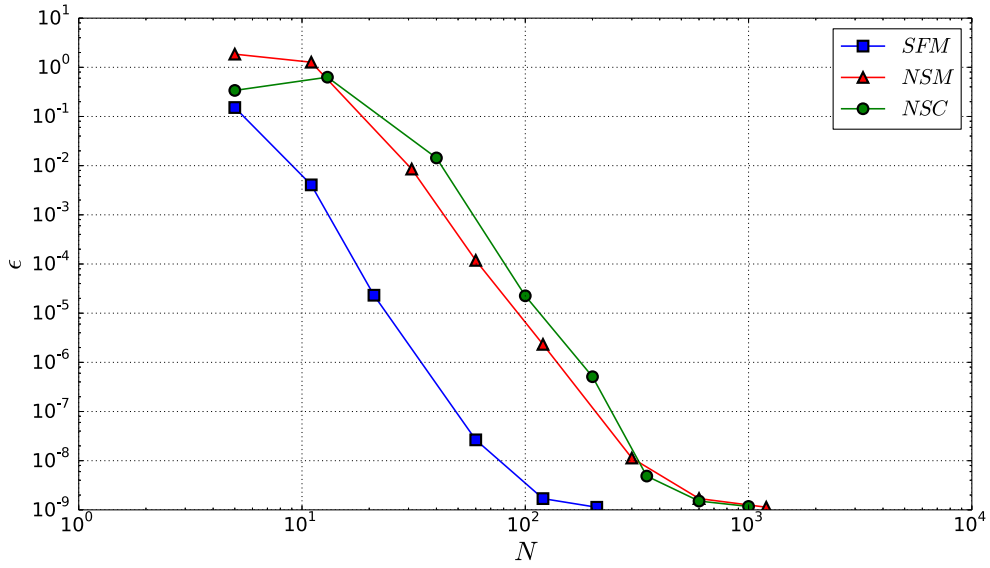

Figure 2.2: Convergence test for three sets of boundary conditions.

We performed a parametric study with $a = [1, 1500]$, $E = [10^{-9}, 10^{-2}]$ and $\Lambda = [10^{-3}, 2]$ for SFM and $a = [1, 1500]$, $E = [10^{-8}, 10^{-2}]$ and $\Lambda = [10^{-3}, 2]$ for NSM and NSC.

2.2.3 Stability of Stationary modes

2.2.3.1 General Properties

In Figure 2.3, we show the typical behavior of the critical Rayleigh number Ra_c with respect to the wave number a. The continuous blue curve corresponds to $E = 10^{-8}$ and $\Lambda = 1$. The dotted green curves are for $E = 10^{-8}$ and $\Lambda = 10^{-1}$ to 10^{-3} and the dashed red curves for $E = 10^{-5}$ to 10^{-7} at $\Lambda = 1$. For each case, we note three specific values for Ra_c. The first is a minimum occurring at low a; its position and value are mostly controlled by Λ and not by E. As such, it is referred to as the magnetic mode which we shall denote by $(Ra_c^m,\ a_c^m)$, where Ra_c^m is the magnetic critical Rayleigh number and a_c^m is the magnetic critical wave number. The second is a local minimum at relatively

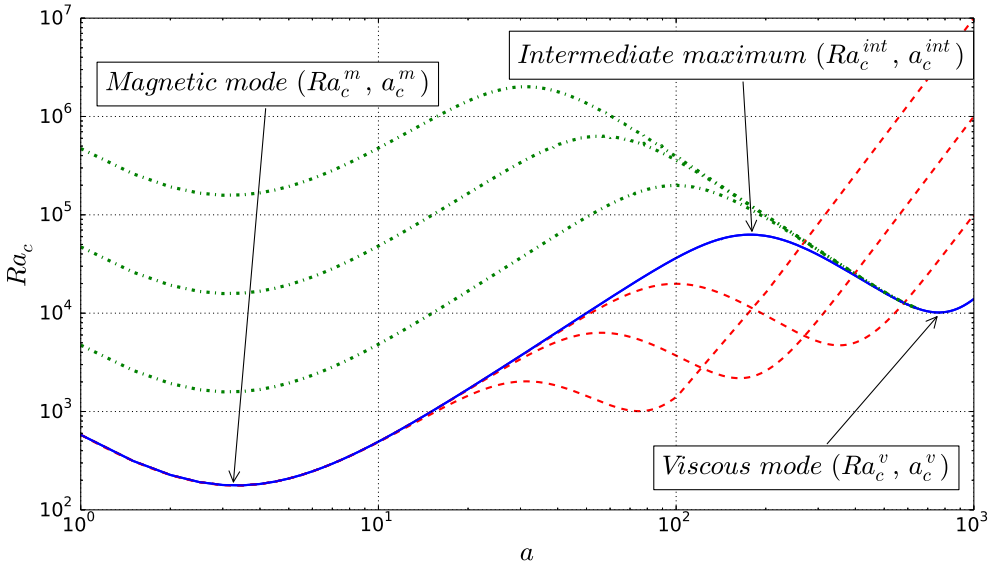

Figure 2.3: Variation of Ra_c with a in the case of SFM boundaries. The continuous blue curve's input parameters are $E = 10^{-8}$ and $\Lambda = 1$. The dotted green curve's input parameters are $E = 10^{-8}$ and $\Lambda = 10^{-1}$ to 10^{-3}. The dashed red curve's input parameters are $E = 10^{-5}$ to 10^{-7} and $\Lambda = 1$.

high a, its position and value depending essentially on E. We shall refer to it as the viscous mode (Ra_c^v, a_c^v), where Ra_c^v is the viscous critical Rayleigh number and a_c^v is the viscous critical wavenumber. Both these modes were first identified by Chandrasekhar [19]. The third feature is a local maximum located between the two previous modes. We call this the intermediate maximum and denote it by (Ra_c^{int}, a_c^{int}). The corresponding mode is always more stable than both the magnetic and the viscous mode and does not reflect any mechanism driving convection. At low E, the value of Ra_c^{int} is several orders of magnitude higher than Ra_c^v and Ra_c^m. The intermediate maximum gives a measure of how much of a separation exists between magnetically controlled modes and modes controlled by viscosity.

2.2.3.2 Scalings for the onset of convection

In Figures 2.4a and 2.4b, we show the variations of Ra_c and a_c with E at $\Lambda = [0.1, 0.3, 1, 2]$ for the viscous mode, magnetic mode and for the intermediate maximum identified earlier with SFM boundary conditions. We note two important results in the limit of $E \to 0$. Firstly, the scalings obtained for the viscous modes reproduce the classical results of non-magnetic convection, that is, $Ra_c^v \propto 22.3E^{-1/3}$ and $a_c^v \propto 1.65E^{-1/3}$; and for the intermediate maximum, $Ra_c^{int} \propto E^{-1/2}$ and $a_c^{int} \propto E^{-1/4}$. Secondly, at low E, convection is initiated by the instability of the magnetic mode. On the other hand, when E increases at a fixed value of Λ, Ra_c^v decreases while Ra_c^m remains constant, so that a crossover value $E_c(\Lambda)$ exists beyond which the viscous mode is more unstable and triggers the onset of convection. Before this point is reached, the clear separation between magnetic and viscous modes progressively starts disappearing. Ultimately, the intermediate maximum merges into the magnetic mode, at which point both disappear, for $E = E_D < E_c(\Lambda)$.

In Figures 2.5a and 2.5b, we report the variations of Ra_c^m, Ra_c^{int}, Ra_c^v, a_c^m, a_c^{int}, and a_c^v with Λ for $E = 10^{-8}$ and $E = 10^{-7}$. Values of the Elsasser number Λ below 10 have been considered but particular attention has been given to Λ around 1, which is relevant to the Earth's core. For higher values of the Elsasser number, Sreenivasan and Jones [56] showed that the Lorentz force had a stabilising effect on the flow so that $Ra_c^m(\Lambda)$ increases instead of decreasing as it does for $\Lambda < 1$. Interestingly, we note the existence of an absolute minimum for Ra_c at $\Lambda \simeq 3.47 \pm 0.08$. The existence of this absolute minimum has been observed in several studies [19, 30, 49, 28]. These studies concerned the outer part of the Earth core, and so the imposed magnetic field was proportional to the distance from the rotation axis and azimuthal. Zhang and Schubert [63] attributed the presence of the minimum to the unphysical nature of the

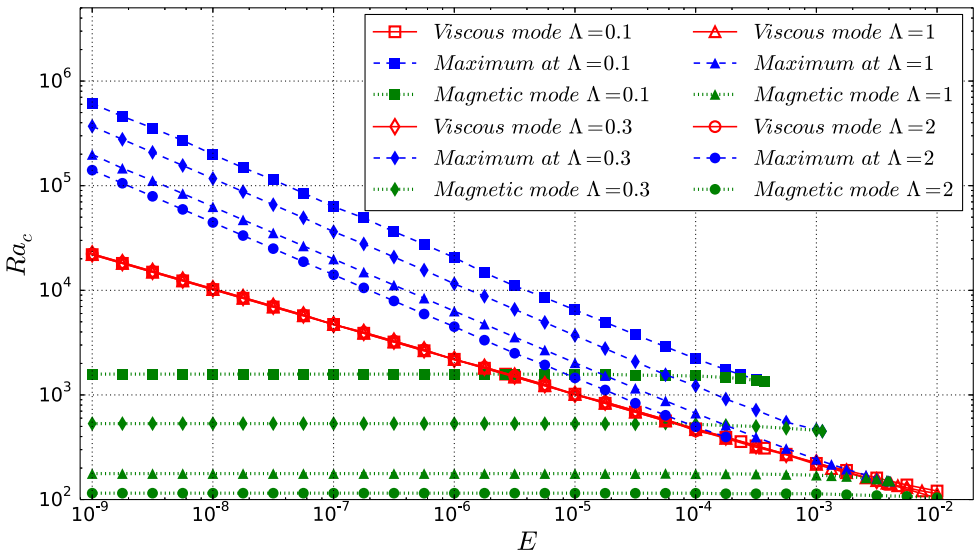

(a)

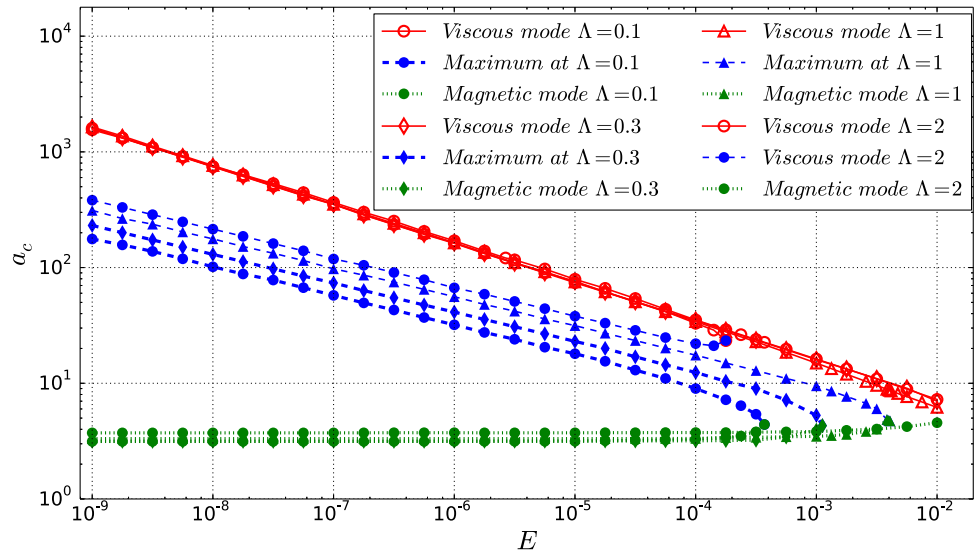

(b)

Figure 2.4: Variation of critical Rayleigh number Ra_c (a) and critical wavenumber a_c (b) with Ekman number E, for SFM boundary conditions.

imposed magnetic field; however, this minimum is a robust feature of plane layer magnetoconvection problems.

In the limit of $\Lambda \to 0$, we observe that the intermediate maximum scales as $Ra_c^{int} \propto \Lambda^{-1/2}$ and $a_c^{int} \propto \Lambda^{1/4}$. For the magnetic mode, on the other hand, $Ra_c^m \propto 160\Lambda^{-1}$ so that the separation between magnetic and viscous modes becomes more and more pronounced as Λ increases. Interestingly, a_c^m is practically independent of Λ and E. The crossover point at which the magnetic mode becomes more unstable than the viscous mode can also be seen.

Figures 2.6a, 2.6b and 2.7a, 2.7b present the counterparts of Figures 2.4a, 2.4b and 2.5a, 2.5b for the problem with NSM boundary conditions, while Figures 2.8a, 2.8b, 2.9a and 2.9b are the corresponding results obtained with NSC boundary conditions. In both cases, the figures indicate that the qualitative behavior of the critical Rayleigh numbers and the critical wavenumbers remains the same as in the configuration with SFM. In particular, the scalings for Ra_c and a_c in the limit $E \to 0$ and $\Lambda \to 0$ remain valid with $Ra_c^v \propto 19.7E^{-1/3}$ (NSM and NSC), $a_c^v \propto 1.55E^{-1/3}$, (NSM and NSC) $Ra_c^m \propto 150\Lambda^{-1}$ (NSM) and $Ra_c^m \propto 75\Lambda^{-1}$ (NSC). Generally speaking, the destabilising effect of the electromagnetic force is significantly stronger with electrically conducting (NSC) than with insulating walls (NSM). First, the stationary modes set in at a significantly lower value of Ra when the boundaries are conducting. Second, the viscous mode is absent for $\Lambda > 0.3$ and $E \lesssim 5 \times 10^{-4}$ with NSC, while it is present at $\Lambda = 2$ with NSM. The minimum of $Ra_c^m(\Lambda)$, on the other hand, takes place at about the same value for both types of electrical boundary conditions.

The results obtained with SFM and NSM boundary conditions corroborate the findings of Sreenivasan and Jones [56] that the mechanical boundary conditions at $z = -1/2$ and $z = +1/2$ have little influence on the onset of convection in these limits. One important difference between the two con-

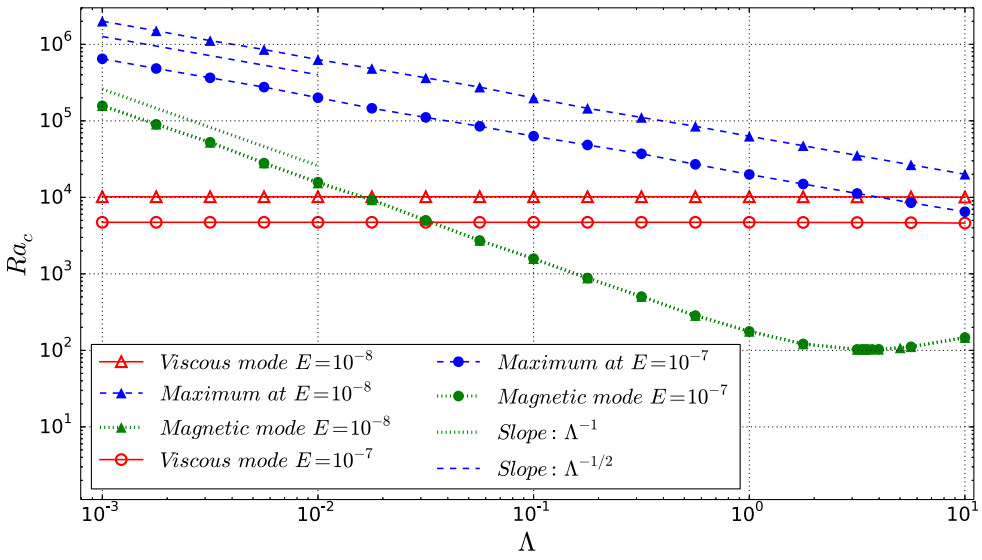

(a)

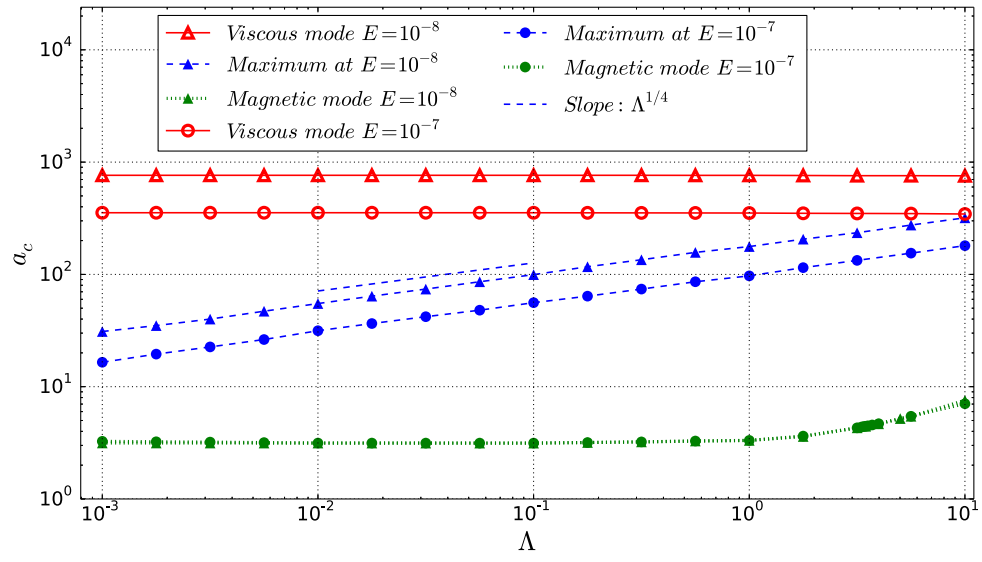

(b)

Figure 2.5: Variation of critical Rayleigh number Ra_c (a) and critical wavenumber a_c (b) with Elsasser number Λ, for SFM boundary conditions.

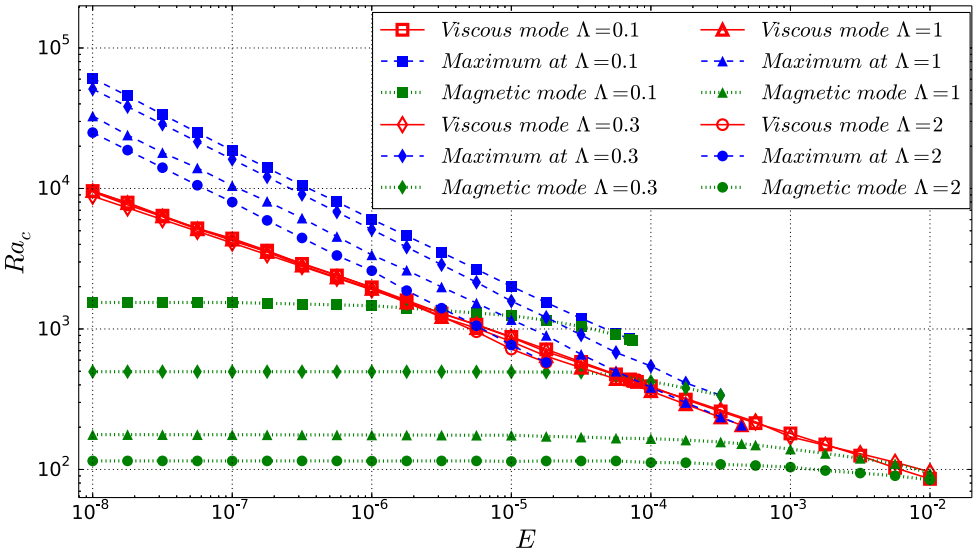

(a)

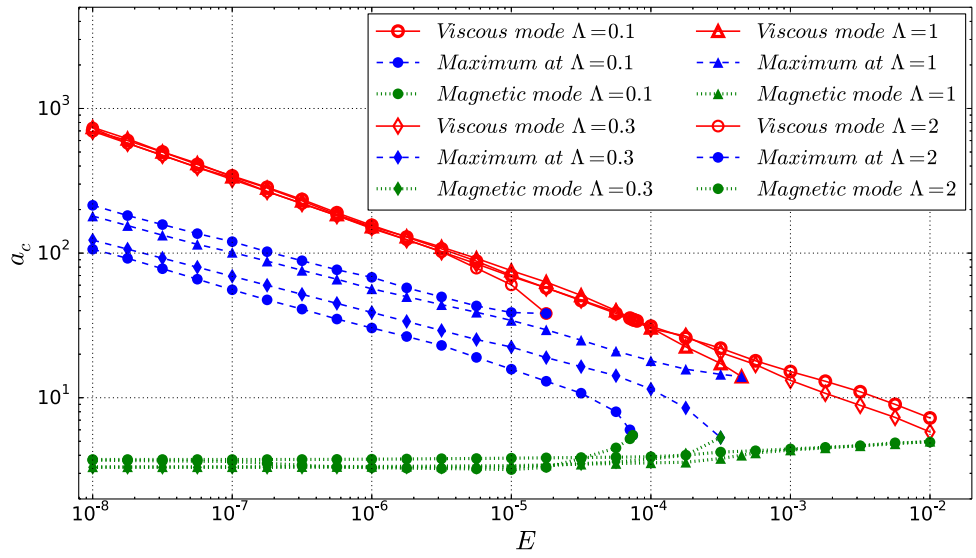

(b)

Figure 2.6: Variation of critical Rayleigh number Ra_c (a) and critical wavenumber a_c (b) with Ekman number E, for NSM boundary conditions.

figurations, however, is that convergence towards the asymptotic scalings is significantly slower with NSM boundary conditions than with SFM boundary conditions (with a typical difference of two decades in E and one decade in Λ). With SFM boundary conditions, at high E and for $\Lambda = 1$, the intermediate maximum merges with the viscous mode rather than with the magnetic mode. This behavior can be expected to take place with NSM boundary conditions too since the wavenumbers of all three modes become closer to each other as Λ increases. Our results confirm the relevance of the problem with SFM boundary conditions to the more realistic problem with NSM boundary conditions. The small influence of the boundaries comes as a useful feature given that simulations with NSM boundary conditions are considerably more computationally expensive than those with SFM boundary conditions.

2.2.3.3 Parametric study of the onset of convection

Figures 2.10, 2.11 and 2.12 map the mechanisms responsible for the onset of convection in the (Λ, E) space. The blue squares represent the area in which only the viscous mode exists. The green triangles characterise the range of parameters where magnetic and viscous modes are present but the most unstable is the viscous one. Finally, the red circles correspond to regimes where both magnetic and viscous modes are present but where the magnetic mode is more unstable than the viscous mode. In these figures, we draw two lines, one marked with dotted red triangles and the other marked with dashed blue triangles. These lines indicate respectively the merging of the intermediate maximum with the magnetic mode where $Ra_c^m = Ra_c^{int}$ and the crossover line where $Ra_c^v = Ra_c^m$. In the limit of $E \to 0$, these respectively obey the scalings

$$\Lambda = 270E, \tag{2.1}$$

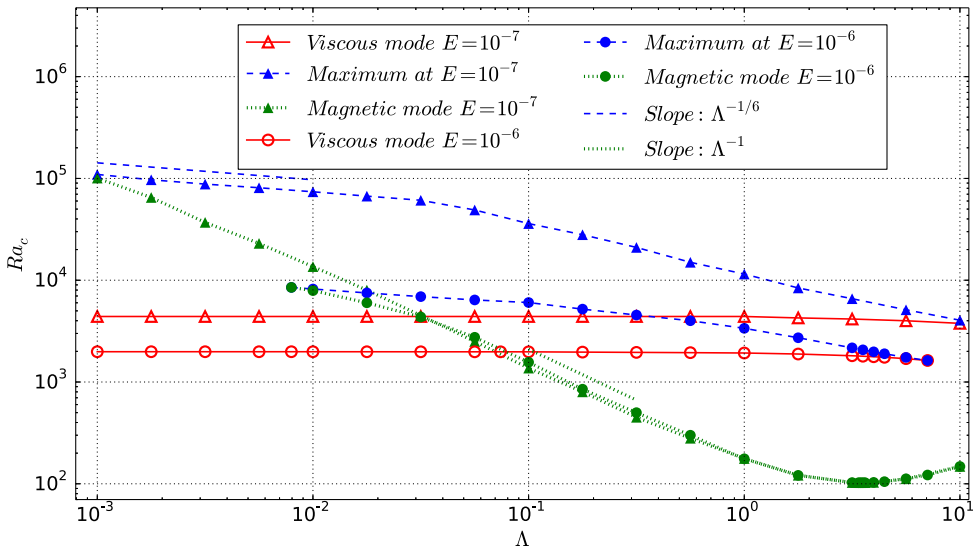

(a)

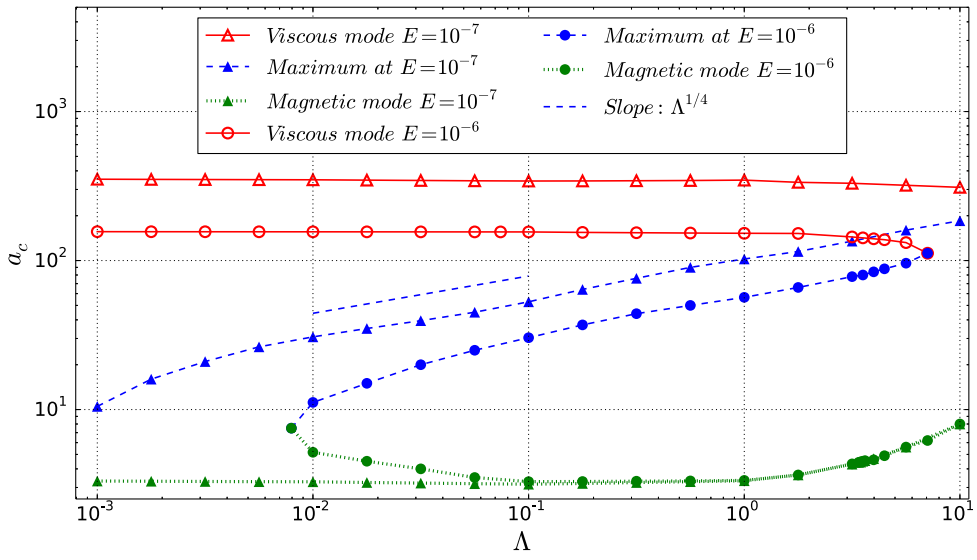

(b)

Figure 2.7: Variation of critical Rayleigh number Ra_c (a) and critical wavenumber a_c (b) with Elsasser number Λ, for NSM boundary conditions.

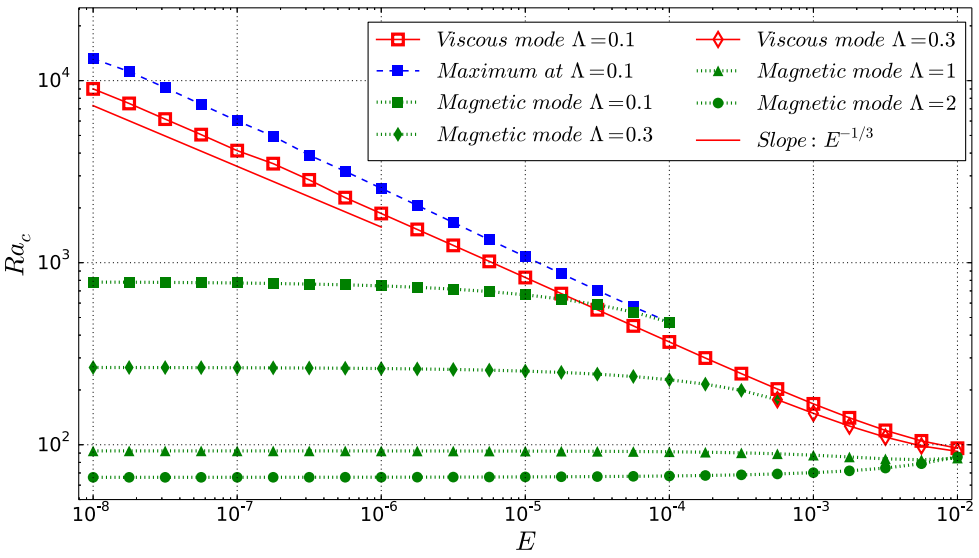

(a)

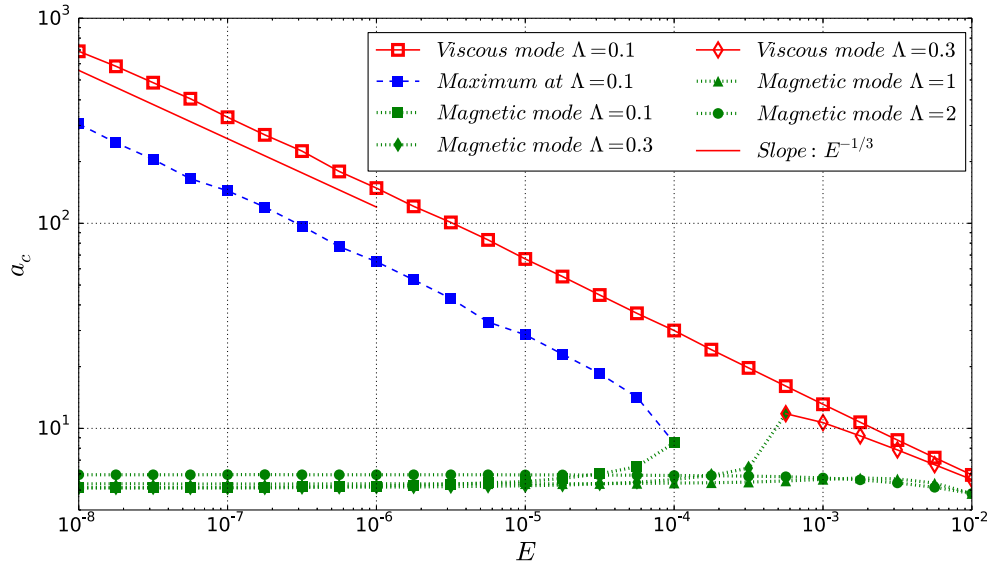

(b)

Figure 2.8: Variation of critical Rayleigh number Ra_c (a) and critical wavenumber a_c (b) with Ekman number E, for NSC boundary conditions.

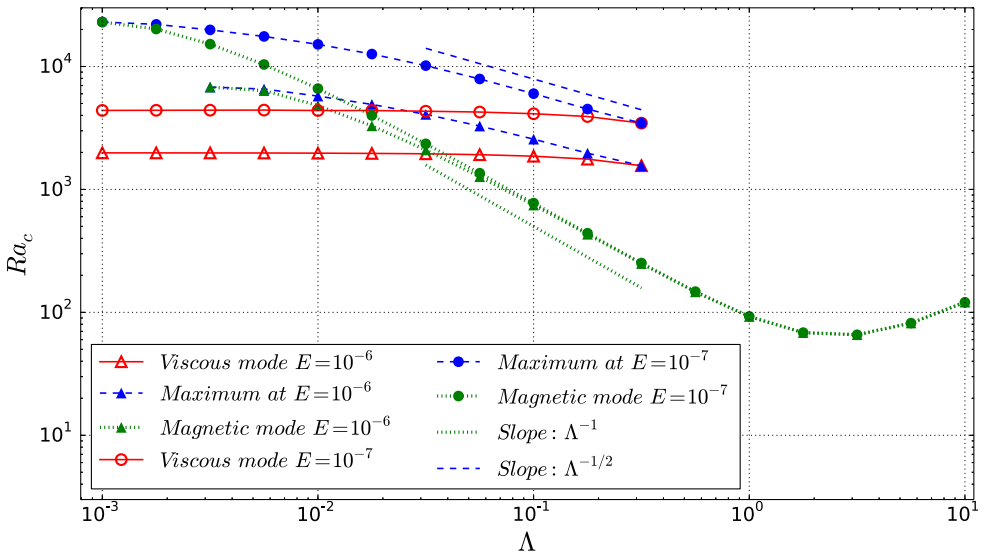

(a)

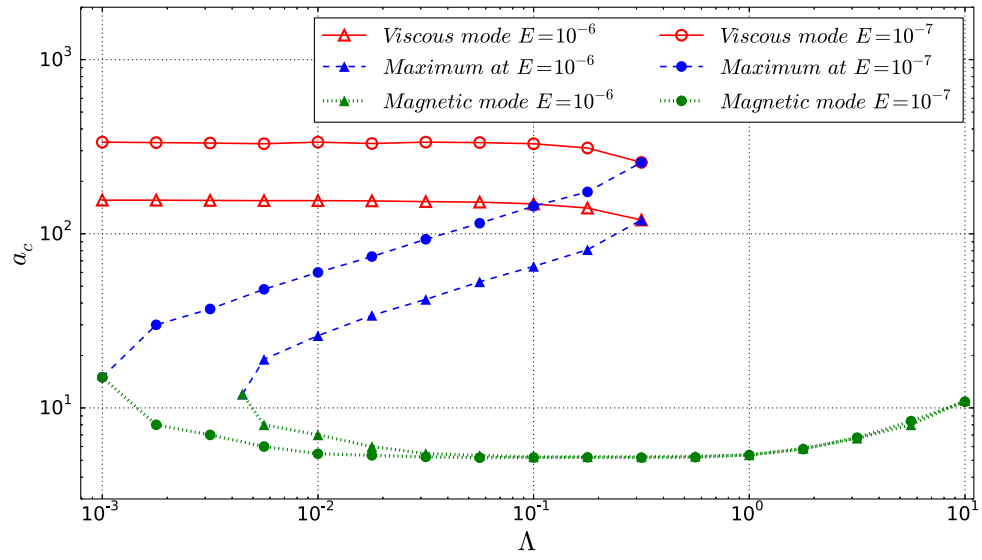

(b)

Figure 2.9: Variation of critical Rayleigh number Ra_c (a) and critical wavenumber a_c (b) with Elsasser number Λ, for NSC boundary conditions.

and

$$\Lambda = 7.22E^{1/3}. \tag{2.2}$$

The exponents in these laws readily follow from the scalings for Ra_c^m, Ra_c^v and Ra_c^{int} obtained earlier. These scalings are noted for all types of boundary conditions, and in agreement with Sreenivasan & Jones [56] and Roberts & King [50]. In the NSM and NSC cases, however, this asymptotic behavior becomes only apparent for $E \sim 10^{-5.5}$ and $E \sim 10^{-4.5}$ respectively. Furthermore, with NSM boundary conditions the transition between magnetic and viscous modes in the non-asymptotic regime still follows a behavior that is qualitatively similar to the asymptotic one, whereas with NSC boundary conditions, the high-E transition strongly departs from the asymptotic transition (see Figure 2.12). Additionally, consistent with the destabilising effect of the conducting boundaries, the transition between magnetic and viscous modes with NSC boundary conditions, while of the same asymptotic nature as with NSM, takes place at noticeably lower Elsasser number. For NSC conditions,

$$\Lambda = 3.6E^{1/3}. \tag{2.3}$$

The scaling with SFM boundary conditions at moderate E is obtained with NSM boundary conditions at very low E. Moreover, the fact that the shape of the Ra_c curve is independent of the diffusivities κ and η allows us to mark out the area of parameters investigated in laboratory experiments [43, 10]. In particular, the experiments of Aurnou & Olson [10] operate outside the viscous–magnetic transition, whereas the experiments of Nakagawa [43] capture this transition. In any case, none of these experiments appears to have reached the asymptotic regime of low E.

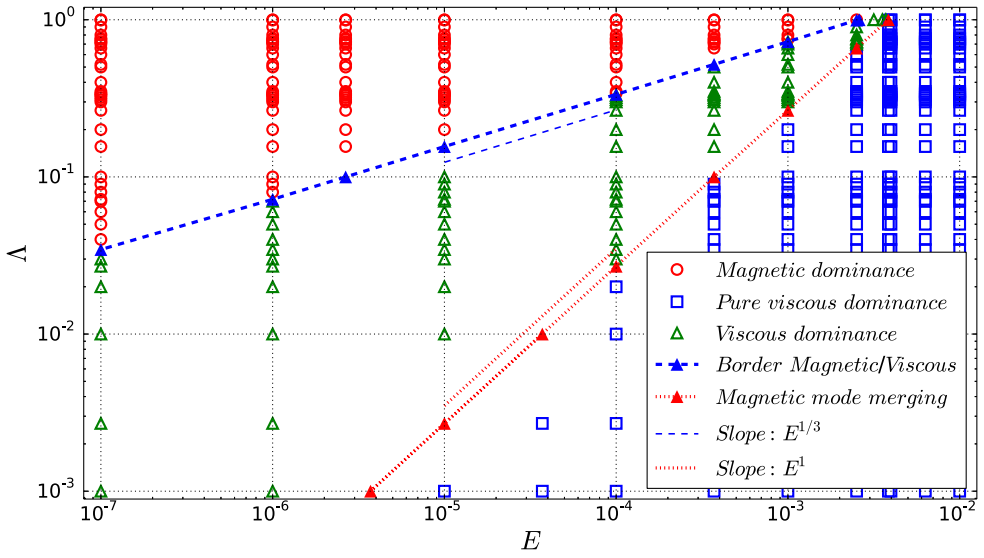

Figure 2.10: Characterisation of modes in the (Λ, E) space with stress-free insulating (SFM) boundary conditions.

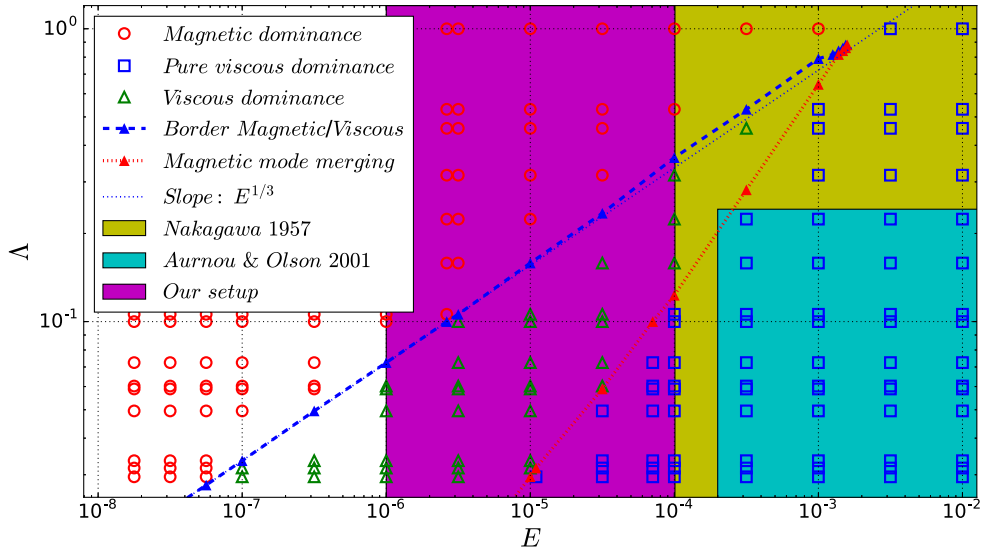

Figure 2.11: Characterisation of modes in the (Λ, E) space with no-slip insulating (NSM) boundary conditions. It is interesting to mention that Aurnou & King [38] operate their experiment in a range of parameters similar to ours. Nevertheless they are not studying the onset; hence they cannot be placed on this mapping. Additionally, we note that the magnetic/viscous border behaves asymptotically for $E < 10^5$ approximately (away from Nakagawa [43] and Aurnou & Olson [10]).

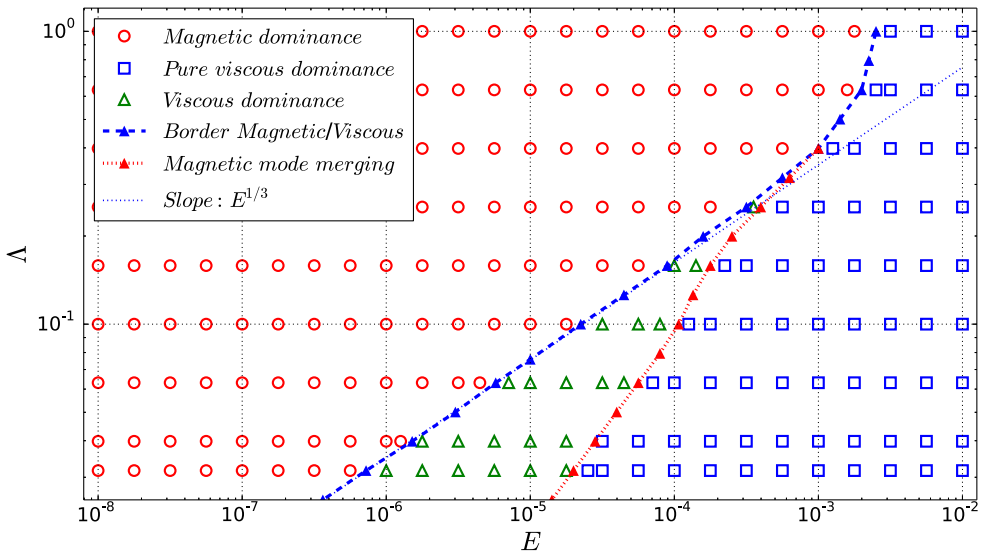

Figure 2.12: Characterisation of modes in the (Λ, E) space with no-slip conducting (NSC) boundary conditions.

2.2.4 Conditions for oscillatory onset

The onset of convection occurs through the destabilisation either of the stationary mode ($\sigma_i = 0$) or of an oscillatory mode (overstability). We shall now determine in which range of parameters the stationary mode, which we calculated in section 2.2.3, is responsible for the onset of convection. The question of overstability is particularly important with electrically conducting boundaries, since without rotation, these have been shown to favor the onset of convection through the generation of thermal Alfvén waves [51].

2.2.4.1 SFM boundary condition

Chandrasekhar [19] gives the equations to derive Ra_c for overstable onset for the rotating magnetoconvective case with SFM boundaries. For a given set of parameters (E, Λ, Pr, Pm), we first determine the set of values of a for which overstability is possible using Equation (66) in page 210 of Chandrasekhar [19]. If overstability occurs, we then use Equation (65), page 210 [19] to evaluate

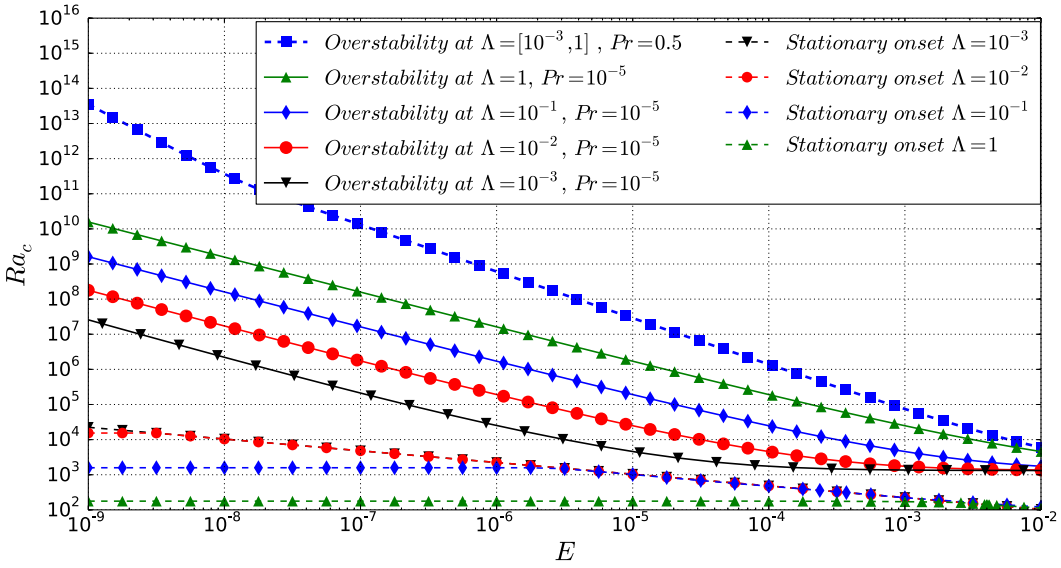

Figure 2.13: Onset of the overstable (oscillatory) and stationary modes at $Pm = 10^{-8}$ for different values of Λ and Pr for SFM boundary conditions. The critical Rayleigh number for the overstable mode is always higher than for the stationary one. This confirms that the stationary mode is the one responsible for the onset of convection in the range of parameters analysed.

the corresponding value of the critical Rayleigh number $Ra_c(E, \Lambda, Pr, Pm, a)$, and minimize this value over the interval spanned by a. Finally, we compare this result with the critical Rayleigh number of the stationary case obtained in the previous section. If the stationary Ra_c is lower, the onset is considered non-oscillatory. In Figure 2.13, we show the critical Rayleigh numbers for the most unstable stationary mode and the most unstable overstable mode for selected sets of parameters. This analysis was performed for $E = [10^{-9}, 10^{-2}]$, $\Lambda = [10^{-3}, 1]$, $Pr = [10^{-5}, 1]$ and $Pm = [10^{-5}, 1]$. It turns out that in this range of parameters, the stationary mode is always the most unstable and therefore determines the onset.

2.2.4.2 NSM and NSC boundary conditions

For these types of boundary conditions, there is no simple analytical way to determine the border between overstable and stationary onsets. Instead, we solve the full system of equations $(1.36)-(1.40)$ with time dependence, varying σ_i in the range $[0, 10^{-1}]$. This way, we can numerically determine whether the critical Rayleigh number obtained for $\sigma_i = 0$ is a minimum. When this is the case, the critical mode is obtained when $\sigma_i = 0$ so the onset does not occur through the overstability route. This technique offers a convenient (although not strictly rigorous) way to determine the overstability condition without incurring the cost of solving the full stability problem for σ as a complex eigenvalue and with Ra as a parameter.

Figures 2.14 and 2.15 show respectively the variations of $Ra_c(\sigma_i)$ around $\sigma_i = 0$ for selected values of E, Λ and Pm for NSM and NSC boundary conditions. We have performed this analysis for $E = [10^{-8}, 10^{-4}]$, $\Lambda = [10^{-3}, 1]$, $Pm = [10^{-8}, 10^{-5}]$ and found a minimum for $Ra(\sigma_i)$ at $\sigma_i = 0$ in all cases. This confirms that the stationary route discussed in section 2.2.3 gives the actual scenario for the onset of convection with both NSM and NSC boundary conditions.

Interestingly, for $\Lambda = 0$, it is known that overstability may occur for $Pr < 0.6766$ (see Table X, page 119 of Chandrasekhar [19]). The reason for this difference between the magnetic and non-magnetic case is most likely that in the limit $E \to 0$, the magnetic mode is always more unstable than the viscous mode and it is stationary. This holds in all cases we considered here ($\Lambda > 10^{-3}$), but overstability may occur for low enough values of Λ, which are not relevant to the Earth's core. Rotating magnetoconvection strongly differs from pure magnetoconvection too where the onset is strongly determined by Alfvén waves [51]. With rotation, the most unstable mode is always stationary,

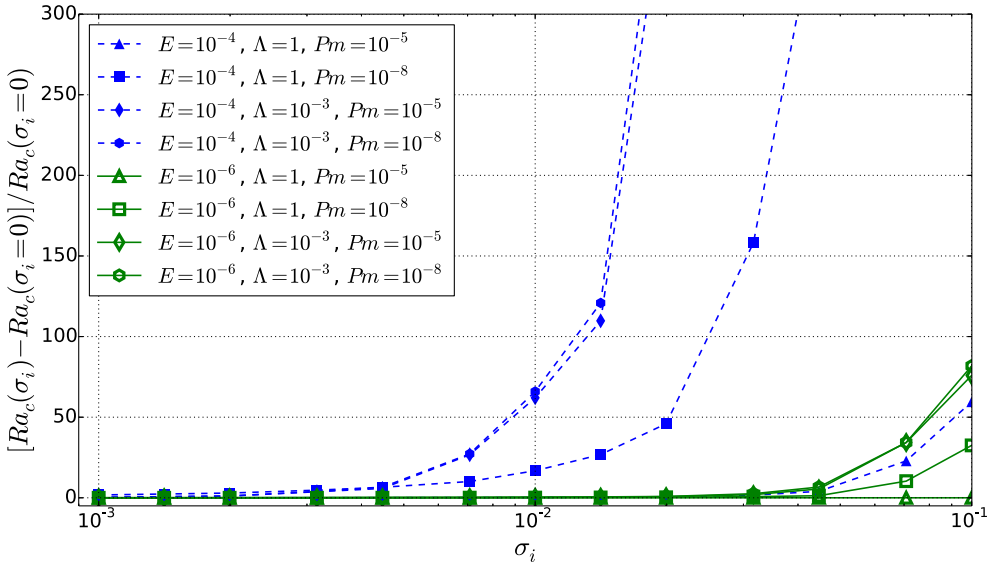

Figure 2.14: Normalised difference between the Rayleigh numbers for the marginally stationary cases and marginally overstable cases for NSM boundary conditions.

so waves cannot play such a prominent role as in the pure magnetoconvective case. We found this to be true in the range of Elsasser number we considered, for which rotation tends to dominate. We anticipate that in regimes of significantly higher Elsasser numbers, electromagnetic effects would dominate and the mechanisms acting in pure magnetoconvection may come to the fore.

2.3 Onset of convection in an inhomogeneous fluid

2.3.1 New form of the general model

In order to derive a model taking into account the variation of thermal diffusivity and electrical conductivity with respect to the temperature field, we introduce the following functions:

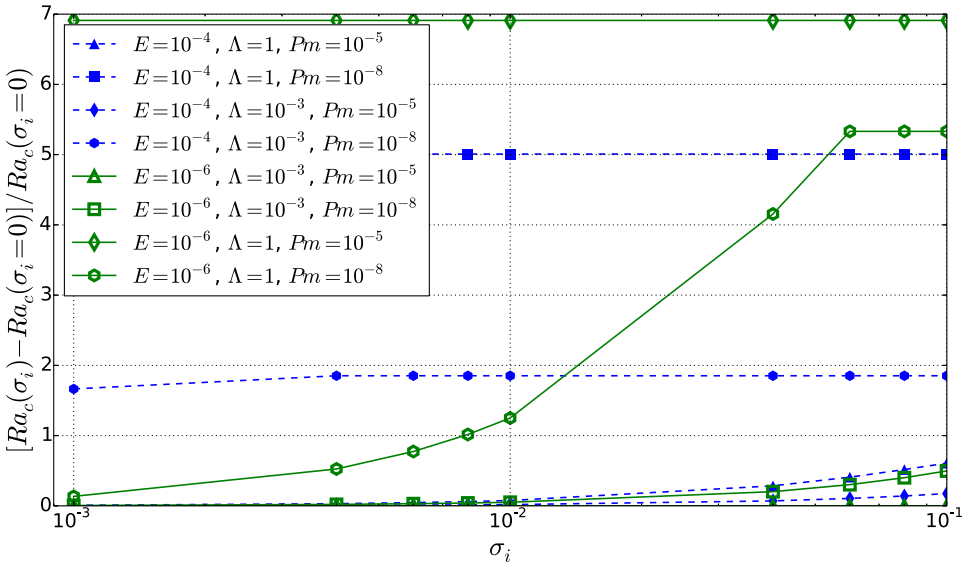

Figure 2.15: Normalised difference between the Rayleigh numbers for the marginally stationary cases and marginally overstable cases for NSC boundary conditions.

- $\Sigma(T)$ the electrical conductivity as a general function of the Temperature normalized by $1/(\mu_0\eta_0)$

- $\eta(T)$ the magnetic diffusivity as a general function of the Temperature normalized by η_0

- $\kappa(T)$ the thermal diffusivity as a general function of the Temperature normalized by κ_0

where κ_0 is a reference thermal diffusivity and η_0 is a reference magnetic diffusivity depending on the investigated fluid. By introducing this dependance in temperature, we have to work with a different initial set of nondimensional equations as follows:

$$Pm^{-1}E(\frac{\partial \mathbf{u}}{\partial t}+(\mathbf{u}\cdot\boldsymbol{\nabla})\mathbf{u})+2\hat{\mathbf{z}}\times\mathbf{u}=-\boldsymbol{\nabla}p+RaT\mathbf{r}+\Lambda(\boldsymbol{\nabla}\times\mathbf{B})\times\mathbf{B}+E\nabla^2\mathbf{u}, \quad (2.4)$$

$$\frac{\partial \mathbf{B}}{\partial t} = \boldsymbol{\nabla} \times (\mathbf{u} \times \mathbf{B}) + \eta \nabla^2 \mathbf{B} + \nabla \Sigma \times \frac{\boldsymbol{\nabla} \times \mathbf{B}}{\Sigma^2}, \tag{2.5}$$

$$\frac{\partial T}{\partial t} + (\mathbf{u} \cdot \boldsymbol{\nabla}) T = PmPr^{-1}(\kappa \boldsymbol{\nabla}^2 T + \boldsymbol{\nabla}\kappa.\boldsymbol{\nabla} T), \tag{2.6}$$

$$\boldsymbol{\nabla} \cdot \mathbf{u} = 0, \tag{2.7}$$

$$\boldsymbol{\nabla} \cdot \mathbf{B} = 0, \tag{2.8}$$

We remark that adding the dependence in temperature for the thermal diffusivity, the magnetic diffusivity and the conductivity does not affect the boundary conditions. Therefore eqs. [1.27-1.31] remain valid with this new set of equations.

2.3.2 Linearization of the eqs.[2.4-2.8]

We follow the same method as [19] and [56] explained to derived eqs[1.36-1.40]. We introduce the different variables as the sum of a basic state and a perturbation such as $\mathbf{u} = \mathbf{u_0} + u$, $\mathbf{B} = \mathbf{B_0} + b$ and $T = T_0 + T'$. Again, we choose the following basic state:

- $\mathbf{u_0} = 0$
- $\mathbf{B_0} = B_0.\mathbf{e}_z$
- $\nabla.(\kappa \nabla T_0) = 0,$

Just as explained for the homogeneous case, we make the assumption of stationarity and we focus on the z-direction as the other direction are considered

periodic. Hence, the general form for the disturbance can be written as previously: $f(z) = \hat{f}(z)e^{i\mathbf{a}.\mathbf{r}_\perp}$. Following the method described previously, we seek for a system of five equations. The details to derive such equations are in the Annex chapter appended to this dissertation.

2.3.3 Perturbation equations from the inhomogeneous model

After deriving the linear analysis, we can write the set of perturbations equation in the case of an inhomogeneous fluid with $B_0 = 1$ and $PmPr^{-1} = 1$:

$$E(D^2 - a^2)\hat{\omega_z} + 2D\hat{u_z} + \Lambda D\hat{j_z} = 0 \tag{2.9}$$

$$-2D\hat{\omega_z} - Raa^2\hat{T'} + E(D^2 - a^2)^2\hat{u_z} + \Lambda(D^2 - a^2)D\hat{b_z} = 0 \tag{2.10}$$

$$\eta(T)(D^2 - a^2)\hat{b_z} + D\hat{u_z} = 0 \tag{2.11}$$

$$D\hat{\omega_z} + \eta(T)(D^2 - a^2)\hat{j_z} + \frac{d\eta(T_0)}{dT_0}DT_0D\hat{j_z} = 0 \tag{2.12}$$

$$\frac{d\kappa(T_0)}{dT_0}DT_0D\hat{T'} + \kappa(D^2 - a^2)\hat{T'} + \hat{u_z}DT_0 = 0 \tag{2.13}$$

The system is still solved as an eigenvalue problem as previously. Therefore, we look for the most unstable Rayleigh number and its wavelength.

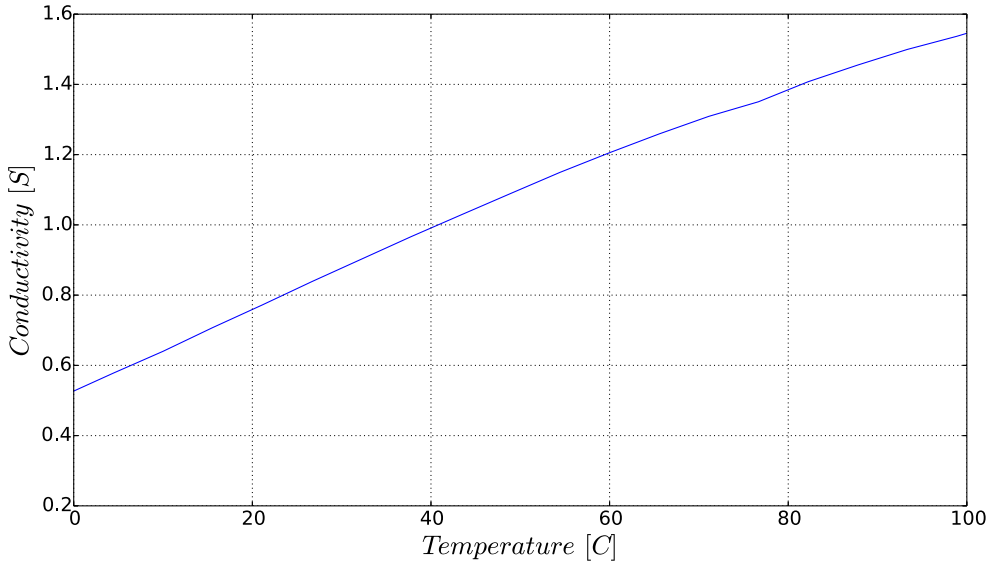

Figure 2.16: Variation of conductivity in Sulphuric acid with respect to temperature at 30% mass concentration extracted from [24]. Note that we did not have access to the data for $\kappa(T)$ or $\sigma(T)$ for this type of concentration.

2.3.4 Scalings for the onset of convection with Sulphuric acid properties

2.3.4.1 Calculation with Sulphuric Acid properties

Lastly, we present the scalings for the onset of convection with sulphuric acid as the fluid. The objective of these calculations is to relate the theoretical results to our experimental setup. Our interest is to observe if the general behavior at the onset can be reproduced although the sulphuric acid conductivity can be strongly affected by the temperature field. Unfortunately, we were not able to access data for the variation of thermal conductivity or viscosity at our given concentration. Hence we did not implement these variations in the present case although it is known that the viscosity of pure Sulphuric acid varies strongly with temperature. Indeed it loses up to a factor 6 from 25 to 100°C. With figure 2.16, we show the the behaviour of the conductivity with respect to the

temperature in sulphuric acid that we used in our computations. The following results correspond to computation with no-slip insulating boundary conditions as they are the one implemented in the apparatus. On figures 2.17a and 2.17b, we compare the scaling of the critical Ra_c and a_c with respect to the Ekman number for the homogeneous case and the sulphuric acid case. Likewise, figures 2.18a and 2.18a compare the critical Rayleigh and wave length at onset with respect to the Elsasser number.

Interestingly for us, we observe that the properties of the onset with the sulphuric acid are very close to the classic theoretical case. Indeed, the maximum difference on the Ra_c is 1.4% and on the wavelength it is 2.85%. This conclusion is of a great significance for us as this is a confirmation that our experimental setup can be trusted to reproduce the physics we are investigating.

2.4 Discussion

As a first section of this chapter, we have presented a detailed parametric study of the linear stability problem governing the onset of plane magnetoconvection down to asymptotic regimes in the limit $E \to 0$. This led to the following results:

1. We were able to precisely verify and quantify the theoretical scalings for the onset of the magnetic and the viscous convection modes, $Ra_c^m \propto \Lambda^{-1}$ and $Ra_c^v \propto E^{-1/3}$, for NSM, NSC and SFM boundary conditions.

2. Our parametric analysis led us to establish a map in the space of parameters (E, Λ) and to distinguish three regions: one where only the viscous mode exists, one where both viscous and magnetic modes exist but the magnetic mode is more unstable, and one where both exist but the viscous mode is more unstable. The crossover between instabilities due to

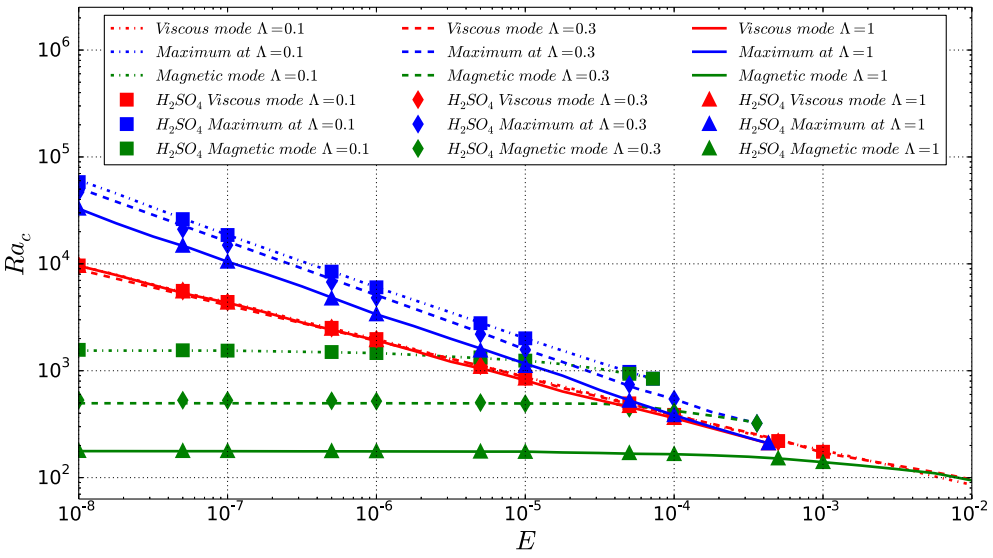

(a)

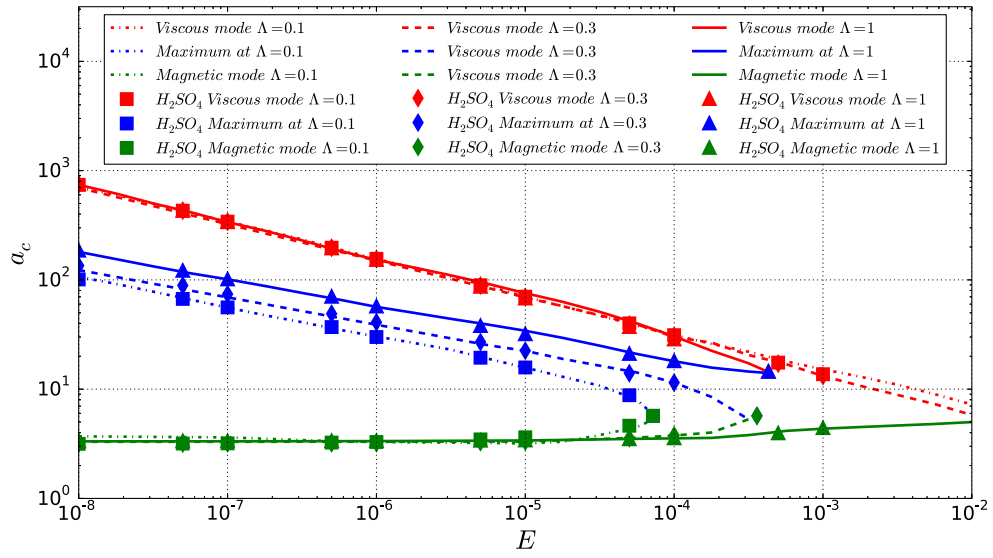

(b)

Figure 2.17: Variation of critical Rayleigh number Ra_c (a) and critical wavenumber a_c (b) with Ekman number E, for NSM boundary conditions. Comparison between the classical model results (solid lines) and the non-classical model with Sulphuric acid properties.

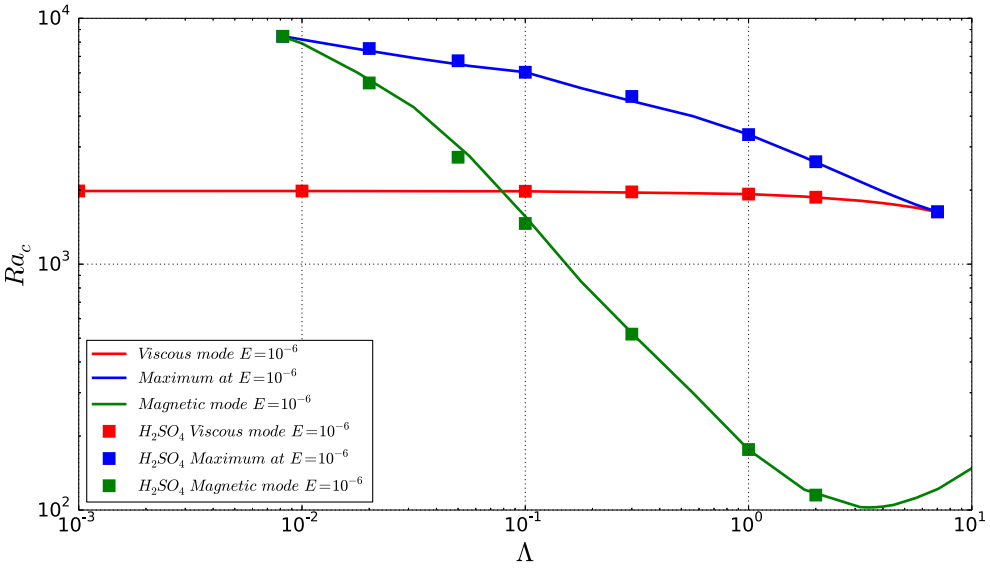

(a)

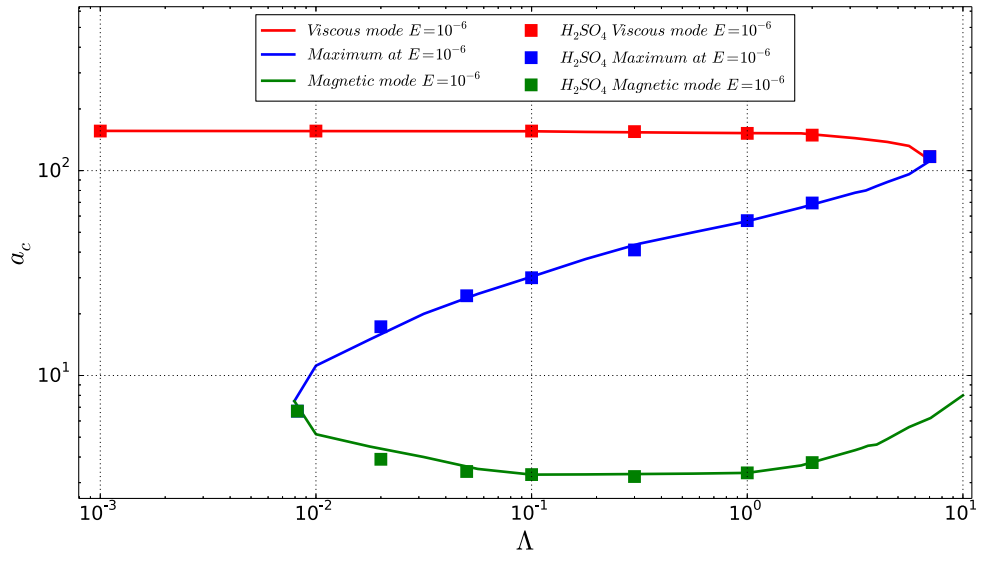

(b)

Figure 2.18: Variation of critical Rayleigh number Ra_c (a) and critical wavenumber a_c (b) with Elsasser number Λ, for NSM boundary conditions. Comparison between the classical model results (solid lines) and the non-classical model with Sulphuric acid properties.

the magnetic mode and instabilities due to the viscous mode occurs for Λ=7.22$E^{1/3}$ in the limit $E \to 0$, in agreement with [56] for SFM and NSM boundaries.

3. In the case of no-slip, electrically conducting boundaries (NSC), the cross-over occurs for Λ=3.6 $E^{1/3}$, i.e. lower than when the boundaries are electrically insulating (NSM). In this sense, electrically conducting boundaries are more destabilizing.

4. The Λ–E regime diagram for NSM conditions (Figure 2.11) explains why the viscous–magnetic transition was observed in the experiments of [43] and not in the experiments of [10].

5. The long-standing question of the occurrence of overstability has been clarified. We have shown that for a wide range of parameters ($E = [10^{-9}, 10^{-2}]$, $\Lambda = [10^{-4}, 1]$, $Pr = [10^{-5}, 1]$ and $Pm = [10^{-5}, 1]$), convection sets in through the instability of the stationary mode. This remains true even under the destabilising effect of electrically conducting boundaries. As such, rotating magnetoconvection at moderate Elsasser number occupies an intermediate ground between rotating convection at low Pr (< 0.6766) and pure magnetoconvection in the low diffusion limit, as in both cases, convection occurs through oscillatory modes (Alfvén waves in the second case [51]).

6. We proved that the classical set of equation of MHD with the Boussinesq approximation is a reasonable assumption for system close to real systems when ignoring the compressibility. Indeed the variation of physical properties were shown not to have a significant effect. This very last point is of great interest because it suggests that the Experiment built with sulphuric acid has the same characteristics around onset. It

also confirm that the experimental results can be legitimately related to the theoretical results. Finally, these results show that the convection is a phenomena arising from global properties of the fluid and not local variations.

Convection in planetary cores is one of the main motivations for the study of rotating magnetoconvection. Yet, it would be somewhat over-optimistic to expect ideal studies such as these to provide definite answers on the actual mechanisms underlying such a complex system. Nevertheless, it is tempting to try and extrapolate our results to planetary systems. Using values of Λ between 0.08 and 1, and $E = 10^{-15}$, our results would suggest that the onset of the convection inside the Earth's TC would be magnetically controlled. In the same way, our analysis can be applied to Mercury, for which $\Lambda \sim 6 \times 10^{-5}$ [26] and $E = 10^{-12}$ [52]. Then, the asymptotic law (2.2) suggests that the convection in Mercury's TC would set off in the viscous mode. The direct implication on the flows is the existence of more numerous and thinner columns instead of large isolated ones in the magnetic case.

Part II

Experimental apparatus and results

Chapter 3

Little Earth Experiment: The Experimental Setup

3.1 Introduction and Challenges

This chapter describes the experimental setup designed and operated over the course of this project. It represents the foundation and the largest part of the time devoted to the present work. As emphasized in the introduction chapter, the apparatus has been designed to model the flow inside the Earth TC. Its purpose is to reproduce the geometry of the problem and the interplay of forces (magnetic, rotating, buoyancy, viscous and inertial) at work in the TC with the possibilty to allow flow visualization. In order to achieve this, we used a glass dome filled with sulphuric acid, heated up on the inside, cooled on the outside and spun inside a high magnetic field. This leads to 3 major challenges:

1. the high magnetic field: it constrains the operational material to be non-conductive to avoid the Joule effect and torque generation.

2. the rotation: exchanging data and fluid between the rotating frame and the main cell is more challenging.

3. the sulphuric acid at high concentration: materials have to be chemically resistant and the setup handled securely.

The magnetic field is provided by strong superconductive and resistive magnets available at the "Laboratoire National des Champs Magnétique intense" - LNCMI. Because of the presence of a magnetic field, we designed the experimental apparatus with as few metallic part as possible. We used almost exclusively plastic or glass and in some places aluminum. The rotation is driven by an electric direct current motor. The consequences of combining rotation and magnetic field are very constraining. Indeed, we had to install the driving motor and the recording system far away from the center of the magnetic field to avoid interferences with the stray fields. Finally, we used sulphuric acid to interact with the magnetic field and be transparent. We required a transparent liquid to implement a Particle Image Velocimetry (PIV) measurement system on our experiment. Implementing an electrolyte such as sulphuric acid turned out to be another difficulty as it implied that all the plastic on the experiment had to be highly resistant to acid. Typically, we used Polytetrafluoroethylene (PTFE) or Polyvinylidene fluoride (PVDF). Additionally, we developed a very strict procedure to setup and operate the experiment in all safety.

This chapter is divided in three main sections: the details of the experiment's design, the description of the instrumentation, and finally the layout of our experimental procedure. To present the apparatus, we show the general design of the system and the different operating configurations. Next, we describe the key elements of the system reproducing the balance between Coriolis Force, Buoyancy Force and Lorentz Force. Then we summarize the achievable range of parameters allowed by our setup. Finally, we conclude by describing the instrumentation with the different measurement systems implemented on the setup and we report our procedures.

3.2 Design of the Experimental Setup

3.2.1 General schematic of the Experiment

Our experiment can be simply described as an hemispherical glass dome filled with sulphuric acid and spun inside a high magnetic field. The apparatus can be divided into different sub-systems: the magnet, the driving system, the main cell and the acquisition system. Although the last three sub-systems were always used in the same configuration, they were implemented in two separate magnets. On Figure 3.1, we present a schematic of the experiment inside a 10 Tesla magnet. It shows the four different sub-systems from bottom to top: the driving system, the main cell, the magnet and the acquisition system. The driving system is composed of:

- A motor (DOGA Model 111 E 22) to produce the torque
- A belt and pulley arrangement to transmit the motor's torque
- A rotary union designed specifically as part of our heating system.

In main cell, we find:

- A 30cm diameter PVC-turntable (Polyvinyl chloride)
- An outer shell (cylindrical container) that helps with the cooling system, visualization and as a mechanical protection for the dome
- A glass dome of a 0.276m inner diameter and 4mm thickness to contain the Sulphuric acid.
- A heating element place at the center of the center of the dome to generate convection. This part is made out of a PVDF base (figure 3.11) and a high thermal conductivity ceramic lid (made of SHAPAL®)

Finally, the acquisition system contains:

- A charge coupled device (CCD) camera (Point Grey Flea 3)
- A control system for the low-power (180mW) diode laser (532 nm)
- A rotating laptop (Lenovo T440) used to recorded the data from the camera and controlled through an ad hoc network with an other computer.

The whole system is approximately 5 meters high. On figure 3.2, we show the electrical system on the setup to power the measurement systems and to communicate with the non-rotating frame.

Figures 3.3 and 3.4 show pictures of the experiment in real situation in a 10 Tesla and 4 Tesla magnet respectively. Because of the size of the magnet the picture in the 10 Tesla magnet only allows us to see the Acquisition System, the magnet and the measurement area. The picture in the 4 Tesla magnet reveals the Driving module underneath the magnet. The 4 Tesla magnet is a cryogenic magnet.

3.2.2 Key elements

3.2.2.1 Generating the Coriolis force

The Coriolis force is produced by spinning the experimental setup. The rotation is driven by a DC-motor placed at the very bottom of the setup. The reason for the position of the motor is that it needs to be kept as much as possible away from the center of the magnet to minimize its exposure to the stray field. On figures 3.5 and 3.6, we present the driving module with a schematic and a picture respectively. These figures highlight the different components of

Figure 3.1: Left panel: Schematic of the complete system inside a 10 T, 376mm bore Magnet (scale: 1:50). Right panel: Detailed drawing of the main vessel. A. Driving module B. 10T magnet C. Main Vessel D. Measurement system 1. Motor 2. Rotary Union 3. Torque tube 4. Liquid Heater 5. Dome 6. Cooling Water 7. Supporting structure 8. PIV Camera 9. Optical speed sensor 10. Wirelessly controlled mobile workstation recording data in the rotating frame 11. Mirror 12. Laser diode 13. K-type thermocouples connected under and in the ceramic plate 14. Pipe carrying ethylene glycol.

Figure 3.2: Schematic of the electrical circuit. A. Static frame (red) B. Rotating frame (blue) C. Main vessel D. Vertical plane E. Horizontal Plane 1. Fixed workstation, 2. Arduino Uno, 3. Optical speed sensor, 4. Mobile workstation, 5. Data logger 6. Four K-type thermocouples, 7. Glass dome, 8. Liquid heater 9. Laser diode 10. Current controller 11. Battery 12. Arduino Leonardo 13. Camera.

the module such as the DC-motor, the belt and the shaft that are transmitting the torque through to the rotary union. Finally, it shows the torque tube connecting the rotary union to the other modules of the setup. The choice of a wheels and belt system to transmit the torque offers a simple and efficient damping system preventing possible vibrations from the motor to contaminate the main cell.

With this setup, we were able to reach a rotation rate of 2 revolutions per second (rps). Although it was used only up to 1.5 rps to preserve the integrity of the setup on a long term. To operate the DC-motor, we only applied a constant potential to it. With figure 3.7, we expose the behavior of the motor

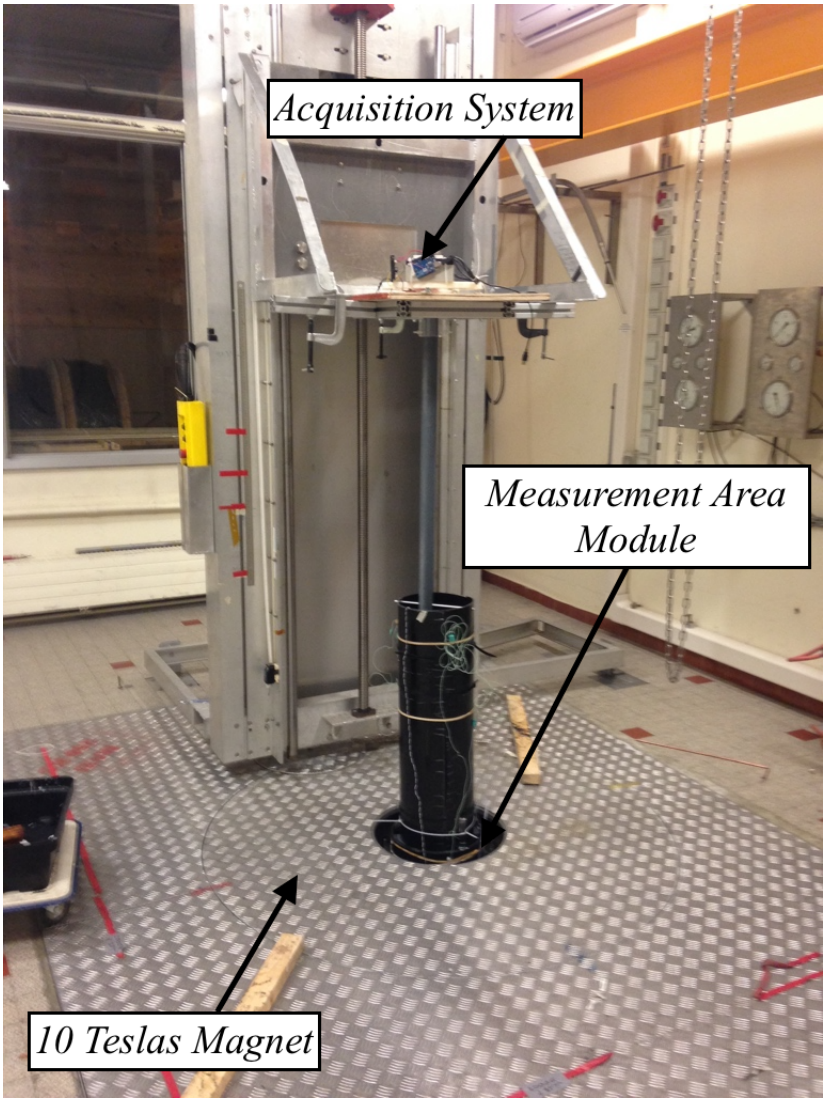

Figure 3.3: Picture of the apparatus installed in a 10 Teslas resistive magnet.

in term of rotation per minute with respect to the input voltage applied on it. We found out a simple linear relation: $Rpm(V) = 2.629 * V - 4.98$. This relation is found with the experiment at constant weight. The measurements were made using a revolution counting device over a period of five minutes for each point. Velocity variations are measured in a range between 2% at high speeds ($>$ 1 revolutions per second) and 6% at lower speeds ($<$0.5 revolutions per second), see figure 3.8. The angular velocity is continuously monitored with the built-in optical system, made of a 72-teeth wheel placed just above

Figure 3.4: Picture of the apparatus installed in a 4 Teslas supraconducting magnet.

the turntable and an optical detector fitted to the magnet bore (see electrical sketch in figure 3.2).

In the perspective of nondimensional numbers, the control parameter for the Coriolis force is the Ekman number. The driving module as it has been presented here allows a range of $E = [10^{-4}, 4{*}10^{-6}]$.

Figure 3.5: Schematic of the driving module.

Figure 3.6: Picture of the driving module.

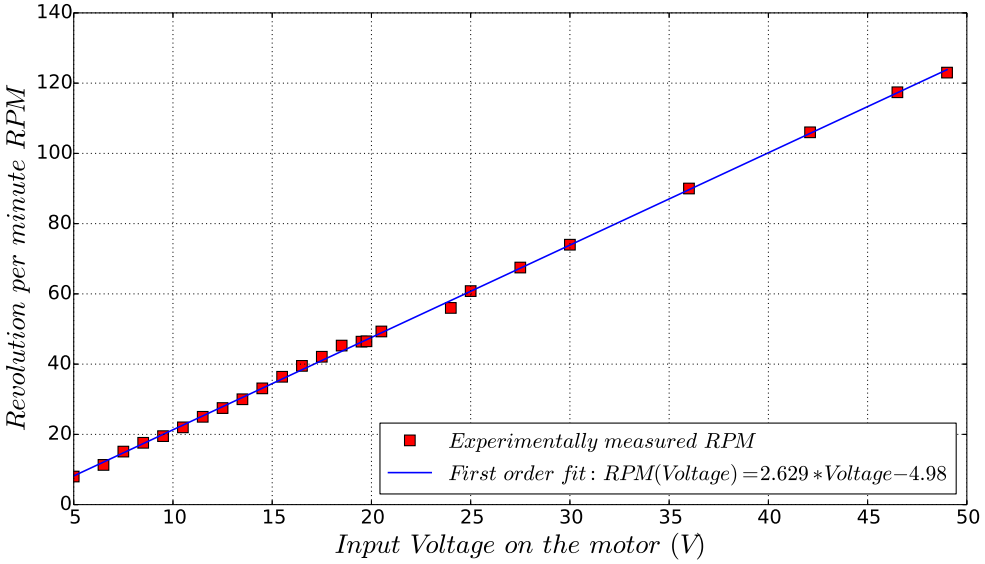

Figure 3.7: Measurements of the rotation speed of the entire system with respect to the input voltage in the driving motor.

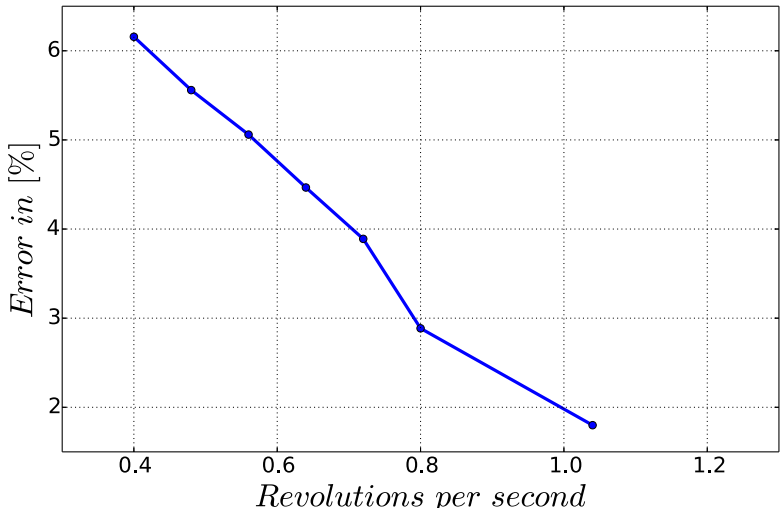

Figure 3.8: Average fluctuations of the rotation rate with respect to the average rotation rate.

Figure 3.9: Schematic of the heating system showing the path of the heating fluid. A. Static frame B. Rotating frame 1. Header tank 2. Pump 3. Electric heater 4. Rotary union and 5. Liquid heater

3.2.2.2 Generating the Buoyancy Force: the rotating heater

The buoyancy force results from an imposed temperature difference between outside and inside of the dome. We developed a heating system specifically for our apparatus to trigger the convection. Figure 3.9 describes the different elements that compose of the heater. The system can be divided in 2 modules: the static frame and the rotating frame connected with a rotary union. In the static frame, we find three parts:

- A peristaltic pump (WMC pump UIM243L02BT) to circulate the heater transfer liquid.
- An electric heater to warm up the heater transfer liquid.
- A header tank to pressurize the hydraulic system and help the pump.

As the experiment is rotating inside a magnet field, it was necessary to build a rotating liquid heating system. Indeed a classic electric heater would gen-

erate a huge torque in rotation inside a magnetic field. Therefore, we ensure a good heat transfer by pushing Ethylene Glycol with a peristaltic pump through an electric heater towards the rotating parts of the experiment. We choose ethylene glycol as the heating fluid because of it has a higher boiling point than water, 197.3°C at ambient pressure, and reasonably low viscosity ($\nu = 14 \times 10^{-6}\mathrm{m^2 s^{-1}}$). This allows us to reach for more extreme regime of convection. The peristaltic pump guarantees a constant flow rate inside the system (100mL/min). As it is presented on figure 3.9, in the rotating frame, the heating system is only made out of two parts: a rotary union and a liquid operated heater. Both of these parts were designed for our setup. The rotary union is connecting the static and the rotating frame with a static aluminum housing and a rotating polyvinylidene fluoride shaft. We paid special attention to the design of the liquid operated heater. Indeed this part is technically challenging as it needs to be non-magnetic, acid resistant and thermally conducting. To overcome these issues, we designed the heater in two parts: a polyvinylidene fluoride (PVDF) base and a high thermal conductivity ceramic (SHAPAL®) top ($k_S = 92\mathrm{W\ m^{-1}K^{-1}}$). These two materials were chosen because they do not react with Sulphuric acid. As a test for these materials specifications, we placed a piece of each in sulphuric acid (at 20°C and concentrated at 30% mass) for a month. As a results we could only observe a difference of the order of 100μg that we linked to the readability of the scale. Figure 3.11 shows the base of the PVDF part. It is composed of two spirals in which the Ethylene Glycol circulates. The two spirals direct the fluid in two opposite directions (inside-out and outside-in), to minimize the inhomogeneity of the heat source.

On top of this part, we placed a ceramic plate that provides a uniformly heated boundary in contact with the sulphuric acid. This part is a plate of

diameter 0.098m to respect the aspect ratio inner core to outer of the Earth core ($\eta_{earth} = 0.35$ and $\eta_{experiment} = 0.355$). Although the ceramic part is simply a circular plate, we have very carefully chosen its thickness, to obtain the best uniformity of the temperature at the surface as well as the isothermal properties of the surface. We approach the problem with two different methods: through dimensional analysis and numerical computations.

Biot Number Following [45] and [10], we used the Biot number to determine the thickness of our ceramic plate. Indeed, the Biot number (Bi) represents the ratio of the thermal resistivity in the plate and in the liquid above it. In accordance to [45] p.29, the boundary can be considered isothermal when $Bi < 0.1$. In our case, it is with a 10mm thick ceramic plate:

$$Bi = \frac{L_{ceramic}/k_S}{L_{H_2SO_4}/k_{H_2SO_4}} = \frac{0.01/92}{0.12/0.5} = 4.53 \times 10^{-4}. \tag{3.1}$$

Therefore, we can safely consider the boundary in between the ceramic and the fluid isothermal.

Computation To support the result obtained with the Biot number, we used a simple finite difference solver to compute the diffusion and advection of the temperature within the ceramic plate. In figure 3.10, we present our results at the top of the ceramic plate with an imposed boundary conditions that corresponds approximately to the effect of the spiral on the PVDF base. Although we acknowledge that these calculations only correspond to a very ideal case, they confirm the previous results as the heat distribution through the ceramic yields a relative non-uniformity of $\pm 0.1\%$ at the interface between the fluid and heater.

With our apparatus we are able to investigate a range of $0.5Ra_c$ to $50Ra_c$.

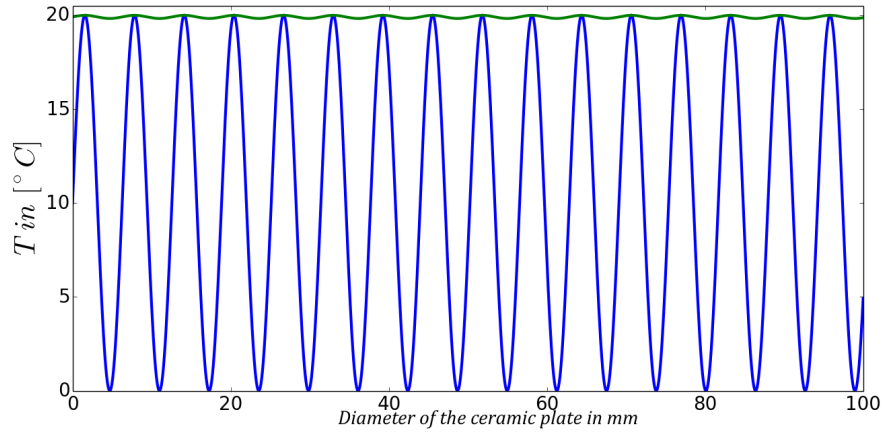

Figure 3.10: Results obtained numerically for the advection/diffusion of the temperature within the ceramic plate. The blue curve corresponds to the imposed boundary condition between the ceramic and the Ethylene Glycol. The green curve represents the temperature at the top of the ceramic after approximately 5 seconds

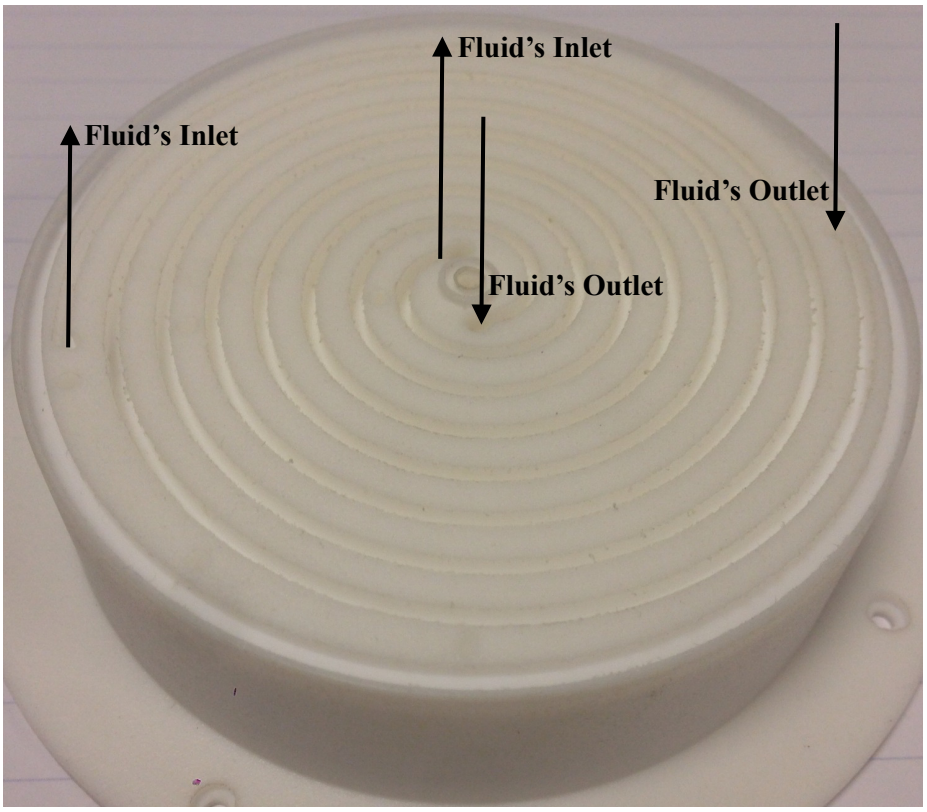

Figure 3.11: PVDF base of the liquid operated heater showing the double spiral circulating the heating fluid (ethylene glycol) below the ceramic element (not shown).

The outside temperature of the dome is kept constant by placing a sufficiently large volume of water above it. The spatial inhomogeneity in temperature at the dome surface is measured using thermocouples placed on the surface and found to lie in the range 1 °C for an imposed temperature difference between the top of the ceramic and the top of the dome of 15 °C. Within the region of the tangent cylinder, the inhomogeneity drops to 0.05 °C. During operation, the temperature at the surface of the heating element is monitored by a thermocouple embedded in the element placed 1 mm below the surface. The temperature at the surface of the dome is not directly measured so that the top view is not obstructed. Instead, the temperature is measured inside the cooling tank above the dome. Figure 3.12 shows an example of the evolution of the temperature at the heater and the temperature measured at the dome surface. The system has a large thermal inertia and reaches thermal equilibrium after approximately half an hour. After this initial transient, the fluctuations of the temperature difference ΔT between heating element and outside cylinder remain of the order of ± 0.1 K and cannot be correlated to fluctuations in the velocity field. It is therefore not necessary to actively regulate the system after thermal equilibrium is reached.

3.2.2.3 Generating the Lorentz force

The Lorentz force is produced by the interaction of a strong magnetic field and an electrolyte. To generate the magnetic field, we use two different magnets: a superconducting magnet and a resistive magnet. The access to both magnets was granted by the "Consortium de Recherche pour l'Emergence de Technologies Avancées" (CRETA) and the "Laboratoire National de Champs Magnetiques Intenses" (LNCMI) based in Grenoble. The superconducting magnet has a bore of 0.460m and is 1.2m height. It can be operated in be-

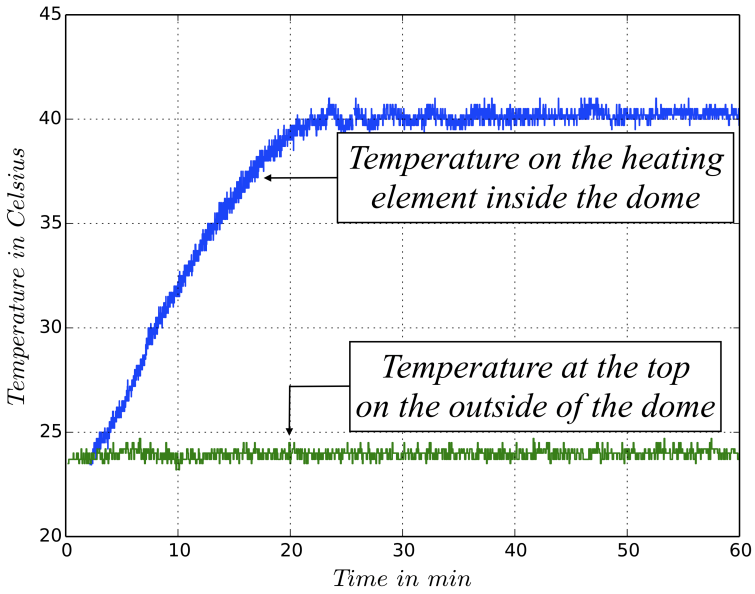

Figure 3.12: Evolution of the temperature between the top of the dome and the heated ceramic at the center of the dome. This test was carried out with a constant voltage of 50V on the static electric heater and 0.75 revolution per secondes.

tween 0 and 4 Teslas. Its magnetic field rises at an average rate of 30 minutes per Tesla. The resistive magnet has a bore of 0.376m and can be operated in between 0 and 10 Teslas. For this second magnet, the field can be ramped up in the matter of a few minutes to 10 Tesla. Of course, with this magnet we exclusively worked at high fields (7 Teslas and above).

For the electrolyte, we choose to work with sulphuric acid following [4] and [3]. This choice is justified by the strong conductivity of the sulphuric acid (80S/m at 26.7°C and 30% mass concentration) and the fact that it is a clear liquid. Therefore it enabled us to investigate the flow with a particle image velocimetry measurement system. On Figure 3.13, we present the behavior of the conductivity with respect with the mass concentration of a mixture Acid/Water. These data were extracted from [24]. They show a maximum of conductivity of approximately 80S/m around 30% mass concentration. The

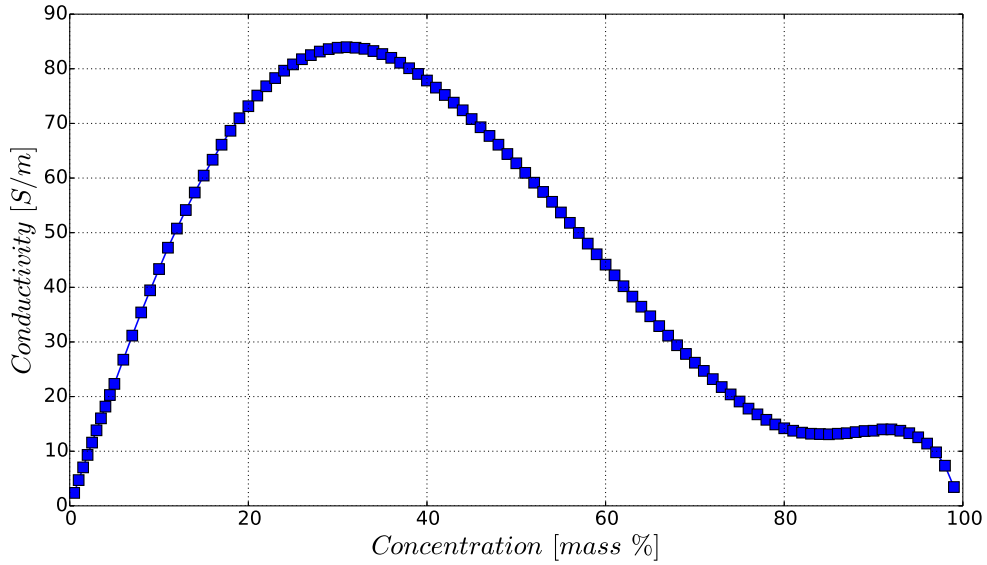

Figure 3.13: Data extracted from [24].

choice of electrolyte was determined by three constraints: it needed to have the highest possible electric conductivity, whilst remaining transparent and Newtonian. Additionally, the viscosity needed to be as low as possible to minimize the Ekman number. At room temperature conditions, electrolytes are by far the simplest choice. The conductivity of electrolytes varies non monotonically with their concentration and often exhibits a maximum resulting from the best compromise between a good concentration of free charge and sufficient ion distribution. Among such electrolytes, Sulphuric acid presents one of the highest conductivity with a reasonably "safe" handling. Additionally the setup is able to run with water for non-magnetic experiments. In table 3.1, we highlight some of the relevant physical properties of the sulphuric acid in our experiment.

Physical properties	Water	H_2SO_4
ν $[m^2/s]$	0.9×10^{-6}	2.06×10^{-6}
ρ $[kg/m^3]$	1000	1250
σ [S/m]	0.005	83
κ $[m^2/s]$	1.4×10^{-7}	1.7×10^{-7}
k $[W/m/C]$	0.58	0.6

Table 3.1: Physical properties of sulphuric acid at 30% mass concentration and water at atmospheric pressure and 25°C.

3.2.3 Apparatus Capabilities

In Table 3.2, we summarized the range of parameters that our setup can achieve and we compare it to the Earth core conditions. The non-dimensional numbers of the experiment are derived with the diameter of the dome $d = 0.276$m and a rotation range $\Omega[\pi/3$ rad/s -4π rad/s] We note that the Ekman number and the Prandtl numbers (classic and magnetic) are out of range due to the low viscosity and especially the size of the Earth core. This is not a surprise as the Earth ranges for this number are out of reach to any numerical simulation or experiments until now. Doubly so as the Prandtl numbers are indicators of the physical properties of the Sulphuric acid in the setup while the Earth core is an liquid iron mixture. Remarkably on the other hand, we observe that our system is able to give a range of Elsasser number that corresponds to the Earth core's order of magnitude. Finally, we add that the two values of the Prandtl number comes from the use of to different kind of liquid (water corresponds to $Pr = 7$ and H_2SO_4 to $Pr = 12$).

Control parameters	Water	H_2SO_4	Earth core	Mercury	Ganymede
$E = \nu/\Omega d^2$	$[1.25 \times 10^{-5} - 1.25 \times 10^{-6}]$	$[4.51 \times 10^{-5} - 4.51 \times 10^{-6}]$	10^{-15}	10^{-12}	10^{-13}
$Ra = g\alpha\Delta T d^3/\kappa\nu$	$[2.09 \times 10^{7} - 2.93 \times 10^{9}]$	$[1.4 \times 10^{7} - 2.25 \times 10^{9}]$	10^{22}	-	-
$\Lambda = B^2/\mu_0\rho\eta\Omega$	0	$[0 - 1]$	$[0.1 - 1]$	10^{-5}	10^{-3}
$Pr = \nu/\kappa$	7	12	10^{-2}	0.1	0.1
$Pm = \nu/\eta$	10^{-15}	10^{-10}	10^{-6}	10^{-6}	10^{-6}

Table 3.2: Range of achievable parameters in the experiment and comparison with planetary parameters. Note that the values of Ra are highly uncertain [54] and corresponds to the classical definition of the Rayleigh number.

3.3 Instrumentation

On our system, we measure two types of quantities: the local temperature and the velocity field. The temperatures are measured with Thermocouples and the velocity field is obtained by particle image velocimetry (PIV).

3.3.1 Temperature measurements

To measure the temperature, we use four classic K-type thermocouples connected to a Pico TC-08 USB Thermocouple Data Logger. With this system, we have a resolution of 0.025 Kelvin. The thermocouples are positioned in order to measure the temperature near the surface of the heater (1mm from the interface Ceramic/Sulphuric acid), on the top of the dome, at the inlet of the heating element and on the outlet of the heating element. With these four points, we are able to recover the temperature difference ΔT in the experiment and the amount of heat flux, Q in W/m^2, passing through our heating element. These two informations combined with the physical properties of the ceramic and the sulphuric acid give us access to the Rayleigh number and the Nusselt number in the experiment respectively. The Nusselt number is given by

$$Nu = \frac{QD}{k\Delta T} \tag{3.2}$$

where D is the fluid layer height above the heating element and k is the thermal conductivity of the working fluid. For simplicity, the reference heat flux in this definition corresponds to conduction between two infinite parallel planes. In the geometry of the experiment, however, heat losses can occur through the lateral boundaries of the cylinder and the the boundaries are not strictly parallel because of the dome curvature. Hence the Nu may not be unity in the case of pure conduction.

3.3.2 PIV visualization

To record the velocity field, a bespoke PIV system has been developed. This experimental technique has been commonly used with transparent fluids but the specific constraints of our apparatus (accessibility, rotation, influence of the magnetic field and risks associated to sulphuric acid) make its implementation particularly unusual. The principle of PIV is to seed the fluid with very small, neutrally buoyant non-inertial, highly reflective particles. These are then illuminated with a laser sheet. The laser sheet is generated with a hemispherical glass rod. The resulting field of brightness is then recorded in a series of frames. The velocity field is obtained by calculating correlations between two successive frames [48]. Given our external constraints, we use a continuous, low-power (180mW) diode laser (532 nm) that is battery-operated. The tracer particles are silver coated glass spheres of size 13μm. Surface charges may appear on the particle surface that could induce electric currents around the particle. However, the corresponding Lorentz force lies typically four orders of magnitude below the possible drag that would be induced by a particle motion relative to the surrounding fluid. Hence, it is safe to assume that despite their metallic coating, the PIV particles do behave as tracers. Once the particles are well mixed in the fluid, we shine a laser sheet of thickness 3.5 ± 0.5mm into the measurement region. The laser is modified to separate the diode (positioned inside the magnet bore, outside the outer cylindrical shell, see figure 3.1) from its electronic controller (placed on the rotating acquisition platform, outside the region of intense magnetic field). The interaction between the laser plane and the particles produces localised areas of high light intensity. Images are captured at 20 frames per second by a CCD camera (Point Grey model FL3-FW-03S1C-C) with Sony ICX618 CCD, 1/4", 5.6 μm sensor. The camera placed on the rotating acquisition table captures images from above the main

cell, either directly or through a mirror fitted outside the cylindrical shell, at the desired height.

This set-up provides two types of measurements, in a vertical plane passing through the centre of the hemisphere (see figure 3.14) and in horizontal planes parallel to the base (see figure 3.15). The vertical plane provides radial and axial velocity components, $u_r(r, z)$ and $u_z(r, z)$ at a prescribed azimuthal angle θ, while the horizontal planes provide radial and azimuthal velocities $u_r(r, \theta)$ and $u_\theta(r, \theta)$ at a prescribed height z in a cylindrical polar coordinate system (r, θ, z). While varying z reveals different areas of the tangent cylinder, the flow inside the tangent cylinder is expected to be statistically axisymmetric under a uniform magnetic field. Hence the laser can be positioned at several heights z and one azimuthal angle.

Velocities in the vertical plane provide us with the size of the convective structure in the radial and axial directions above the heater. This is the preferred measurement to characterise the onset of convection and to observe upwelling motions. Azimuthal velocities measured in the horizontal planes give information on the structure of the azimuthal wind and polar vortices.

3.4 Experimental procedure

The experimental procedure can be divided in two different parts. The first is the preparation of the setup, including positioning elements and filling the dome. The second is the operation once the apparatus is installed from switching on the magnet to generating convection.

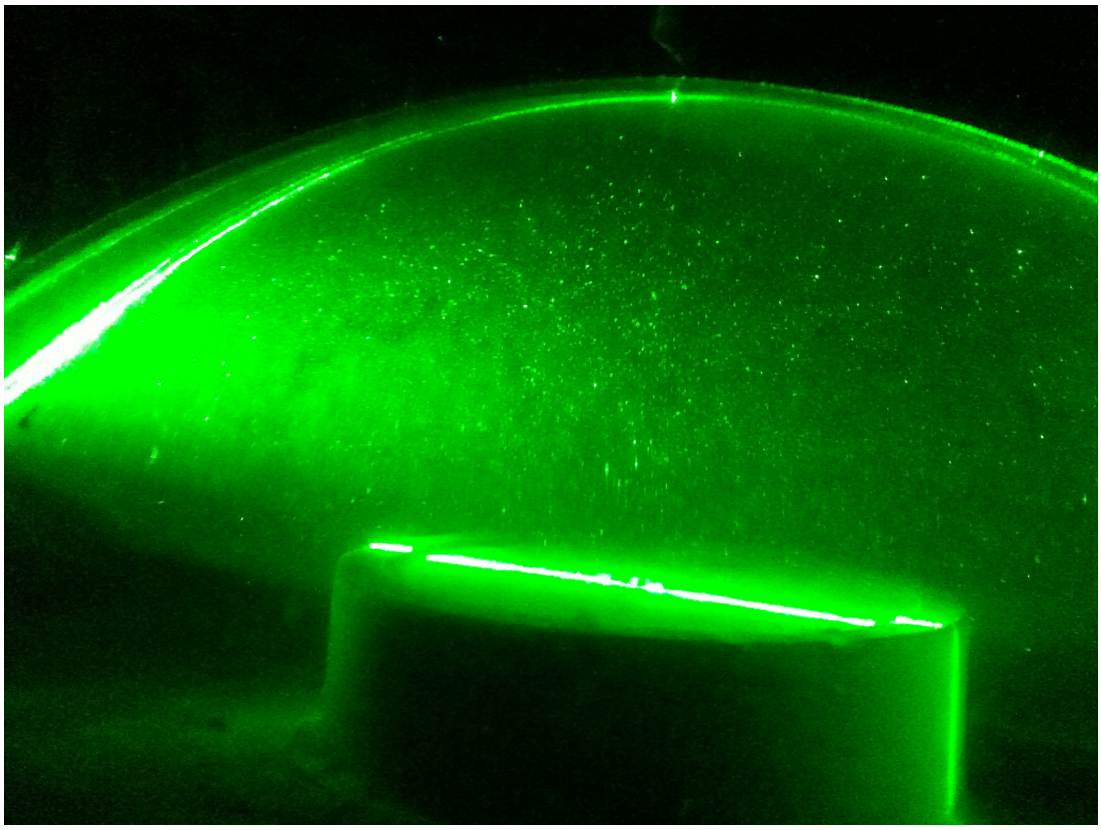

Figure 3.14: Picture showing the vertical plane from the top of the heating element to the top of the dome.

3.4.1 Preparation

The guarantee of correct, fruitful measurements strongly depends on the quality of the preparation. For safety and practical reasons the magnetic field has to be off during the preparation phase. Assembling the hardware can be divided in three phases:

1. Positioning the driving module with respect to the magnet. Alignment in between the rotating axis and the magnetic field axis is ensured by specific ring spacers connecting the experiment to the bore of the magnet. The ring size depends on the magnet the setup is assembled in.

2. Filling the measurement area module (glass dome) with sulphuric acid, positioning it inside the magnet and connecting it to the driving module.

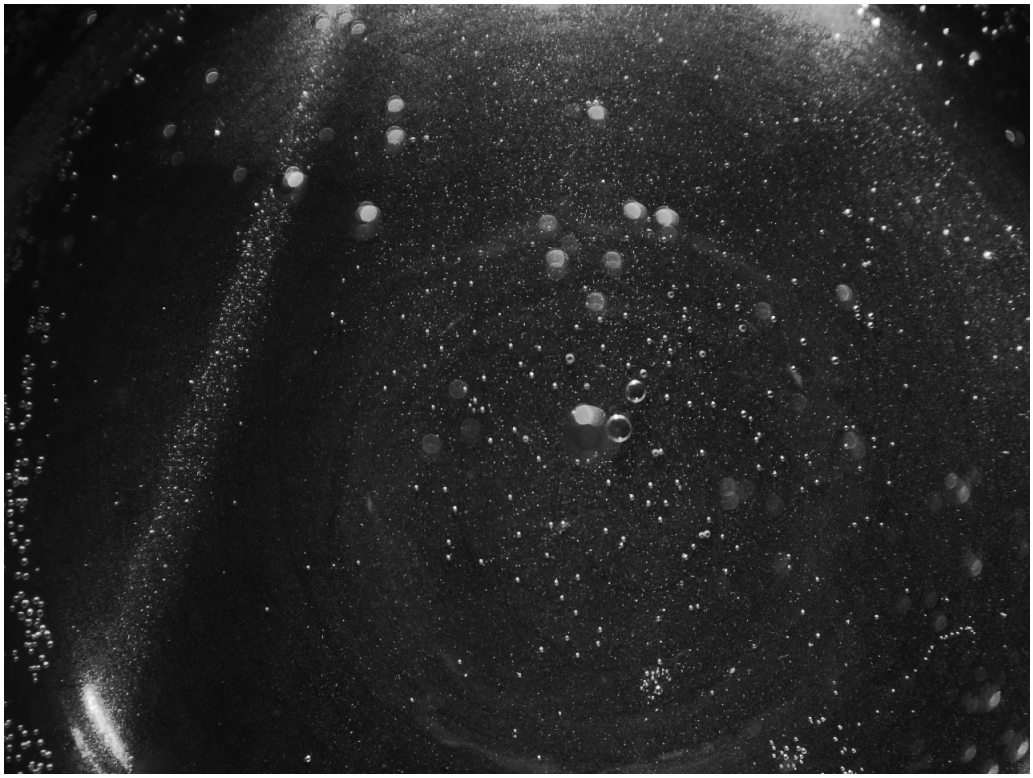

Figure 3.15: Example of a picture showing the horizontal plane 6cm above the top of the heating element.

3. Bolting the acquisition system on top of the magnet and installing the different component such as laser, camera and laptop with respect to the measurement area module and the magnetic field.

Considering the apparatus reaches a total height of up to 5m, the alignment between rotating parts is a critical point although the setup was designed with sufficient degree of liberty to guarantee the rotation even if a misalignment up to 5 mm occurs. Additionally, we believe that the filling of the glass dome with sulphuric acid is worth explaining for any other team who could be interested in building a similar setup. Filling the glass dome requires several steps:

1. Filling the outer cylinder surrounding the glass dome's location with 30 littres of sulphuric acid

2. Immersing the dome upside down in the sulphuric acid helped by acid resistant gloves with long sleeves.

3. Once the dome is fully submersed, flipping the dome in the right position without trapped air bubbles inside

4. Pushing the dome in its position and in doing so trapping exactly 15 litres of sulphuric acid inside the dome

5. After making sure that there are no bubbles inside the glass dome, pumping out the sulphuric acid that remains outside of the dome

6. Pump in water on the outside of the dome. This plays a role in term of safety if the sulphuric acid starts to leak and it acts as a coolant while running the experiment.

3.4.2 Operation

Once installed and filled the experiment can be operated. We obey the following chain of events detailed as follows:

1. Inject a slurry of H_2SO_4 and silver coated particle inside the dome by the pressure released valves. This necessary step for PIV must come with great care to avoid injecting air bubbles inside the dome.

2. Control the connections (see figure 3.2):

    - Acquisition Laptop to Control Laptop by making sure the wireless ad hoc network (both node of the network can exchange informations) is on and both laptop communicate with each other.
    - Acquisition Laptop to Laser diode's controller by turning on and off the laser diode with the control laptop.

- Acquisition Laptop to Camera and control of the optics while the Laser is on.
- Setup the camera (size of the image, acquisition rate...) with the interface installed on the acquisition laptop.
- Acquisition Laptop to the Thermocouples by running a short measurement with the control laptop.

3. Ramp up the magnetic field.
4. Disconnect the Acquisition Laptop from the power socket.
5. Setup a rotation rate by applying a constant voltage to the driving motor.
6. Rotate the system for 30 minutes to guarantee that the fluid inside the dome behaves as a solid body in rotation.
7. Start the pump on the heating system to circulate the heating fluid from the static to the rotating frame.
8. Impose a voltage on the heating element is the static frame.
9. Wait for 30 minutes in order for the flow to fully develop.
10. Control the thermal equilibrium of the system with direct readings of temperature on the Control Laptop.
11. Turn on the Laser diode from the Control Laptop.
12. Start temperature measurements.
13. Start the camera for measurements.
14. Once the measurement is finished start again from 9 with a higher voltage until the Acquisition Laptop has either no more battery or recording space.

The whole operating process corresponds approximatively to a period of 8 to 9 hours depending on the chosen intensity of the magnetic field and the length of each measurement. For most of our measurements, we recorded 8000 images at 20 frames per second. This allowed us to gather data for up to 7 different Rayleigh numbers.

3.4.3 General convergence of the results

In this section, we are briefly introducing some of the convergence tests that we ran to ensure the validity of the results presented in the following chapter. With figure 3.16, we show convergence test for averages in time using rolling averages on the averaged velocity field. Here, we chose to focus on the case at the limit of our study. Therefore we were interested only in the lower and higher Ekman number and in each case the lowest and highest Elsasser and Rayleigh numbers. Our averages were made out of 8000 consecutive images at a frame rate of 20 images per second. We conclude that our results on the averages have be considered with a precision between 5×10^{-2} and 5×10^{-1}.

3.5 Conclusion

In this chapter, we described in detail the experimental setup that was designed, built and operated over the course of this project. This experiment is the first to combine the effects of Rotation, Lorentz force and Convection and to allow particle image velocimetry measurements. As such we believe that our setup constitutes a multiphysics platform to study geophysical and fundamental fluid mechanic topics.

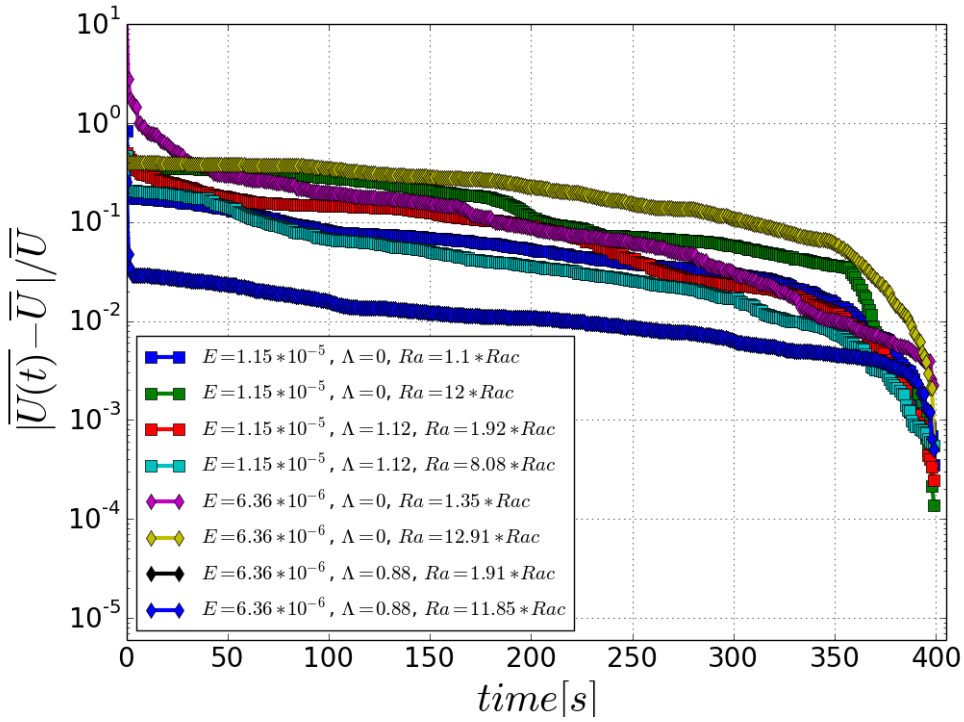

Figure 3.16: Test of convergence for the critical cases (at the limit of our experimental setup in terms of magnetic field, rotation and temperature difference) presented in following sections.

Chapter 4

Convection in a Tangent Cylinder

4.1 Introduction

In the present chapter, we introduce results obtained with our experiment from a hydrodynamic point of view rather than geophysical. The purpose is to characterise the effect of rotation and magnetic field on the convective patterns. To organize this chapter, we follow convection from its initiation to the weakly supercritical regimes and above (approximately one to ten times critical). Indeed we want to answer questions such as:

1. When does the onset of convection occur?
2. What is the structure of the convective cells at the onset of convection?
3. What is the effect of the magnetic field on the flow at onset and beyond?
4. For what Elsasser number does the transition between viscous and magnetic occur at onset of convection?

Although some of this questions already motivated an extensive literature, we believe that they deserved a second look with our setup as our geometry doesn't correspond fully to a plane layer or to a cylindrical geometry. Indeed

the aspect ratio of the Tangent Cylinder cannot be ignored and considered strictly equivalent to the plane layer theory. Also the boundary conditions of the tangent cylinder can not be interpreted as rigid as the cylindrical geometry . To our knowledge, the closest experiments corresponding to our configuration are [43], [10], [8] and [64]. The first two correspond to plane layer geometry with liquid metal. Therefore the measurements in both cases correspond only to temperature, heat flux and qualitative visualisations. On the other hand, [8] had a similar geometry as our but performed measurement without magnetic field and with a highly qualitative measurement system. Finally [64] corresponds to a study in a cylindrical shape of the same aspect ratio as the Tangent Cylinder but with rigid walls and without magnetic field. Our experiment is therefore the first to answer the questions asked, in a representative geometry, with the right force balance in the Tangent Cylinder and quantitative measurements of the flow motion. In the following we will first mention the development of the convection without magnetic field at onset and above, and highlight the differences with the plane layer theory as well as the consistencies with the cylindrical geometry. Then we will report the effect of the magnetic field on the onset of convection and beyond it. We will highlight the transition to magnetic regime at onset and the robustness of the magnetic mode above onset. After, we will also focus on the global quantities in our results such as the evolution of the energy with respect to the Rayleigh number and the velocity fluctuations. The study of the energy aims to characterise the different modes taking place in the flow. The fluctuation will inform us on the steady or turbulent state of our results. Finally we will conclude on the large discrepancy induced by the presence of the magnetic field on the flow pattern at any level of criticality.

4.2 Non-magnetic Convection

In this section, we report the results obtained without magnetic field. We will describe the flow at onset and continue further with the supercritical regimes.

4.2.1 Onset of Convection

General results The structure at the onset of convection has been long examined and corresponds to columnar structures. With figures 4.1, 4.2, 4.6 and 4.7, we illustrate the flow dynamic with a time average of the velocity field in the vertical plane and the horizontal plane at two different values of the Ekman number. With figures 4.1 and 4.2, we remark that structures appear corresponding to helical columns with successive upstream and downstream motions. These figures are a clear representation of the expected effect of the rotation without magnetic field: the structures become thinner as the system rotates faster.

Before introducing the results for the onset in the horizontal plane, it is necessary to describe some of the results presented by [33], [65] and [64]. In these studies, the authors investigated the convection at onset and beyond in a rotating cylinder. They observed that the aspect ratio of the cylinder plays a major role in determining the most critical mode at the onset. They showed that they can be two different types of modes: "fast" and "slow". On figures 4.3 and 4.4, we highlight the shape of the fast and the slow mode respectively with the results obtained by [33]. On figure 4.3, we can clearly see that the fast mode originates at the boundary of the cylinder. The authors in [33] described the fast mode as a fast precession mode. On figure 4.4, we show that the slow mode arises at the center of the cylinder. Again in [33], the name slow mode

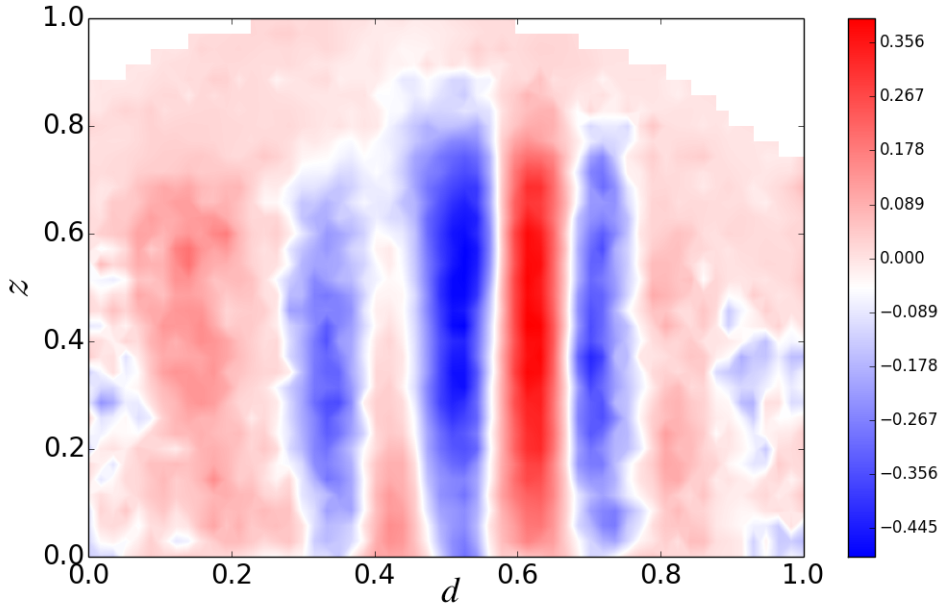

Figure 4.1: Average over time of the vertical component of velocity in cm/s from PIV measurement above the liquid heater for $E = 2.51 \times 10^{-5}$ at our measured onset $Ra = 3.48 \times 10^7$. On the figure, d is normalized by the diameter of the heater and z is normalized by the height of liquid between the heater's surface and the dome. The cut at the top of the pictures and the pixel effect on the side are due to the discretization of the PIV software.

comes from the idea that this is a slow precession mode. Finally, another interesting results from [33] is that the slow and the fast modes for a mode 1 can alternate as a function of the rotation rate. This alternate behaviour is illustrated in figure 4.5 with [33]'s results.

In the horizontal plane with figures 4.6 and 4.7, we only obtained results very close to the onset of convection but not below it. On these results, the horizontal plane is not square as it is limited by the junction of the laser plane and the dome that is circular. Indeed the measurement in the vertical plane and the horizontal plane are made during separate runs as we used only one LASER and one camera. Additionally, the measurements were located at a height above the dome's equator corresponding to the 68° in latitude (which

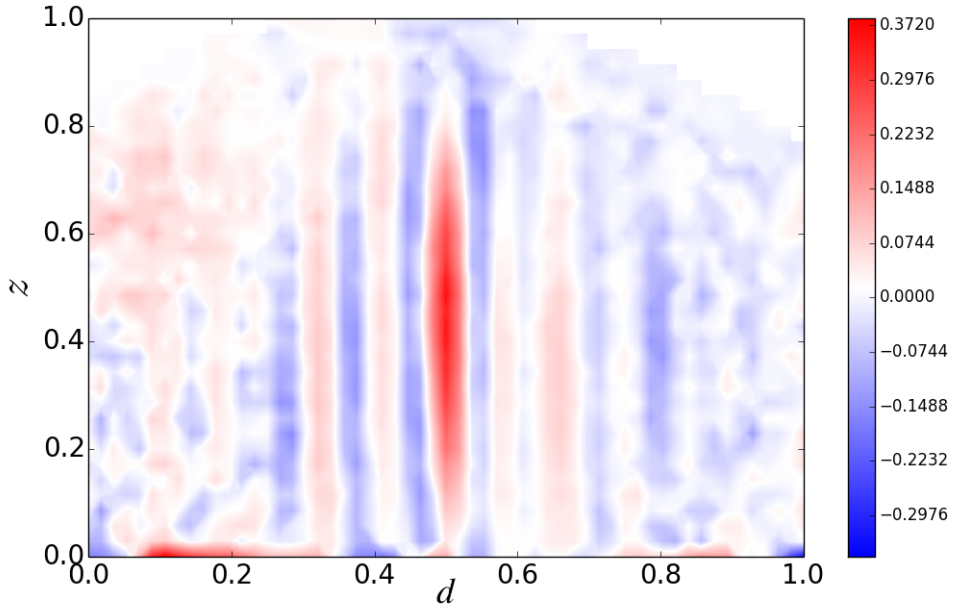

Figure 4.2: Average over time of the vertical component of velocity in cm/s from PIV measurement above the liquid heater for $E = 3.36 \times 10^{-6}$ at our measured onset $Ra = 3.82 \times 10^8$. On the figure, d is normalized by the diameter of the heater and z is normalized by the height of liquid between the heater's surface and the dome. The cut at the top of the pictures and the pixel effect on the side are due to the discretization of the PIV software.

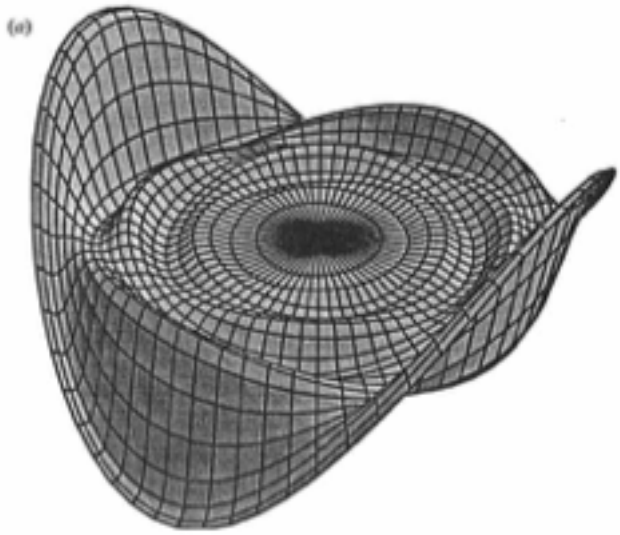

Figure 4.3: Fast mode presented for temperature field in [33] corresponding to a mode 2

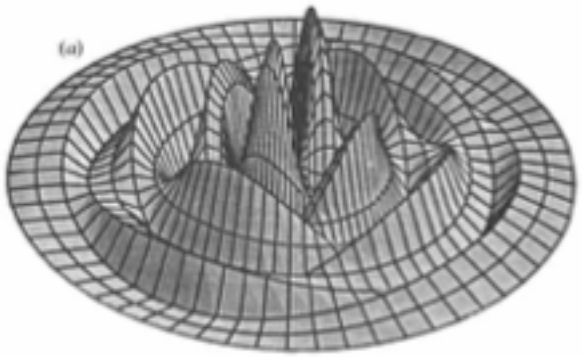

Figure 4.4: Slow mode presented for temperature field in [33] corresponding to a mode 2

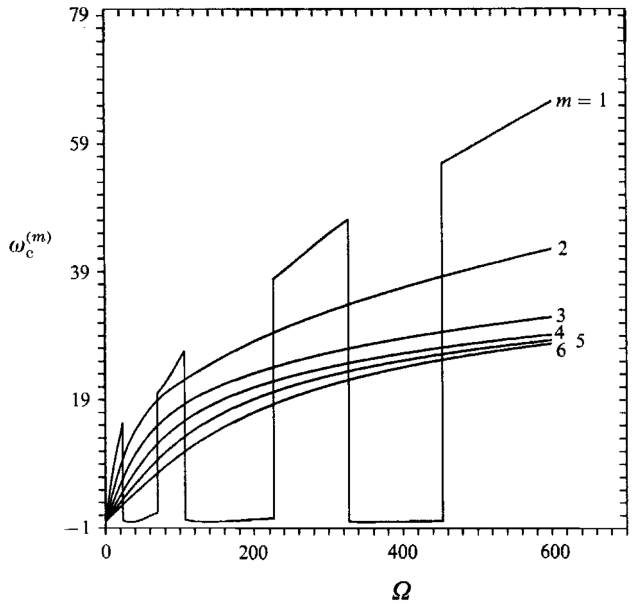

FIGURE 9. The competition between the fast and slow modes for different values of m as a function of Ω for fixed $\Gamma = 1$, $\sigma = 6.7$, and boundary conditions A. Note that for $m \geqslant 2$ the fast modes always have lower critical Rayleigh number than the corresponding slow modes; for $m = 1$ it is either the fast or the slow mode that has a lower critical Rayleigh number, depending on Ω.

Figure 4.5: Results from [33] showing the evolution of the modes frequencies with the rotation rate and alternative behaviour of the mode 1.

corresponds to 90 mm above the heater). As a result, we were unable to observe precise columnar structures since at the onset, convective plumes are more intense in the vicinity of the heated boundary and only weak further into the bulk. Nevertheless, with figures 4.6 and 4.7, we illustrate the behaviour of the flow in this region for weakly supercritical cases. In these figures, the coordinates are normalized by the diameter of the liquid heater. Although the observed structures are very weak, it appears as previously that their size becomes smaller as the Ekman number diminishes. It is also interesting to compare these results with studies in rotating cylinder. Indeed figure 4.6 corresponds to the fast mode 1 described by [33]. This mode is known to be stable. On the other hand with figure 4.7, we show that the onset corresponds much more to a slow mode 1 described by the authors of [33]. This makes sense as the fast and the slow modes alternate as a function of the rotation rate. Nevertheless to be make sure that our modes are indeed fast and slow, we investigated the evolution of the frequencies in our system and determined the frequencies at onset with a fit on our data. On figure 4.8, we show the frequencies without magnetic field in our system for these two cases. The frequencies are normalized by κ/h^2 (h is the height of fluid and κ the thermal diffusivity) following [33]. They are derived from the axisymmetric part of the average azimuthal velocities. With our fits we obtain a frequency at onset of 852 for the fast modes and a much lower value for the slow mode. It is not possible to give an exact value for the slow mode as the slope of the fit is very large. Our results seems in good agreement with [33] as the authors predicted a frequency of 930 for the fast mode with our rotation rate (extrapolated from 4.5). It is also essential to acknowledge that the extrapolation is purely based on the points observed on [33]'s figures. Therefore it is not as rigorous as a theoretical results. Yet there is a precession at the onset of convection in our

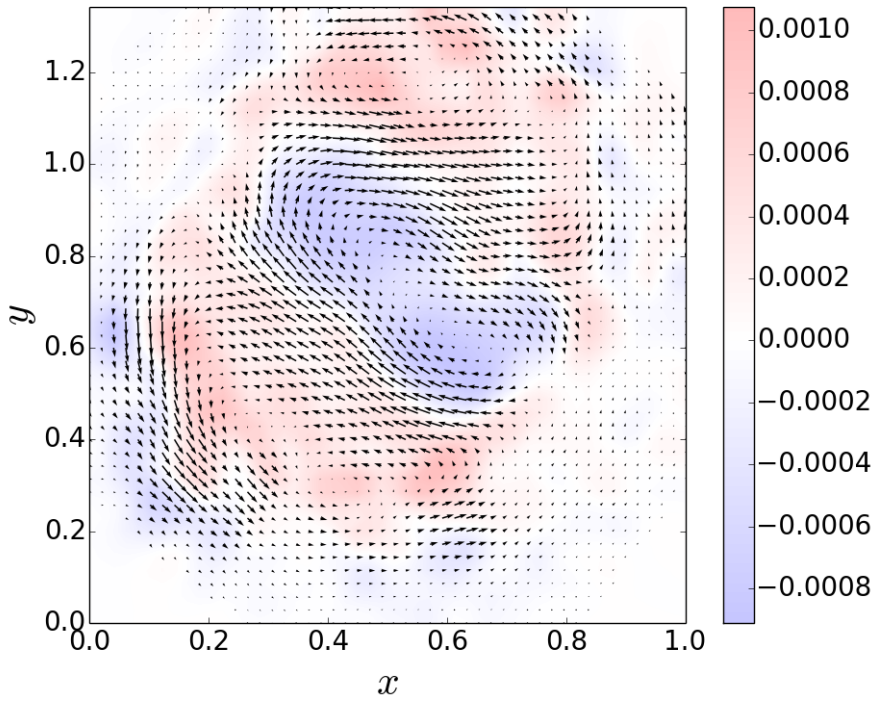

Figure 4.6: Average of the velocity field (arrows) and vorticity (color) in time at $\Lambda = 0$ near the onset of convection with $Ra = 1.13 \times Ra_c$ and $E = 1.15 \times 10^{-5}$. On the figure, x and y are normalized by the diameter of the heater d. The center of the heater corresponds to the center of the pictures. Additionally, y is often larger than 1 because the area of interest in the PIV software was larger than the heater in that direction.

Tangent Cylinder which suggests that the plane layer theory as in [19] is not fully satisfactory for the Tangent Cylinder.

Additionally, the fast mode corresponds to motions on the side of the cylinder as we see in figure 4.6 and the slow mode corresponds to motion at the center of the cylinder as figure 4.7 shows. Finally, we remark that in figure 4.7 there are trace of small helical structure at the center of the Tangent Cylinder. This feature is characteristic of the plane layer geometry. Therefore we have to conclude that our results correspond to a mix between cylindrical and plane geometry.

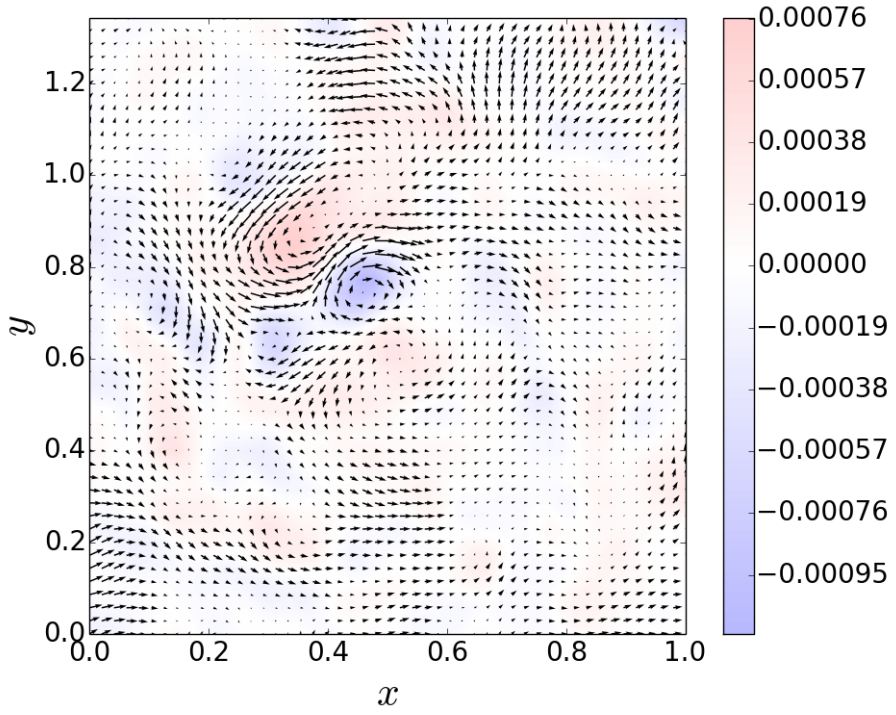

Figure 4.7: Average of the velocity field (arrows) and vorticity (color) in time at $\Lambda = 0$ near the onset of convection with $Ra = 1.35 \times Ra_c$ and $E = 6.36 \times 10^{-6}$. On the figure, x and y are normalized by the diameter of the heater d. The center of the heater corresponds to the center of the pictures. Additionally, y is often larger than 1 because the area of interest in the PIV software was larger than the heater in that direction.

Scalings for the onset In order to quantify accurately the change in size of the convective structures, we calculated the spatial correlations of vertical component of velocities along the radial direction on the velocity field average on time. As an example, figure 4.9 highlights the correlation function obtained for the cases corresponding to figures 4.1 and 4.2 which have respective Ekman numbers of $E = 2.51 \times 10^{-5}$ and $E = 3.36 \times 10^{-6}$. To determine the size of the structures, we seek the minimum value of the spatial increment for which the correlation function is zero. Figure 4.10 is zoomed in on the area of the first zero for all the results obtained without magnetic field.

Using the results shown in figure 4.10, we were able to characterize the

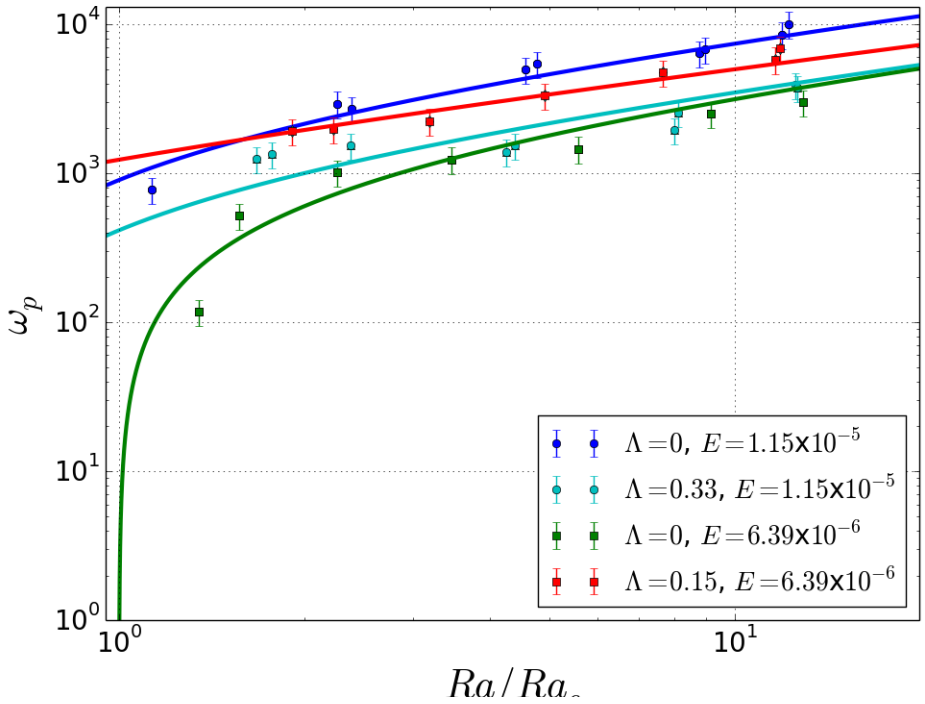

Figure 4.8: Evolution of the frequencies of precession obtained in our results following [33].

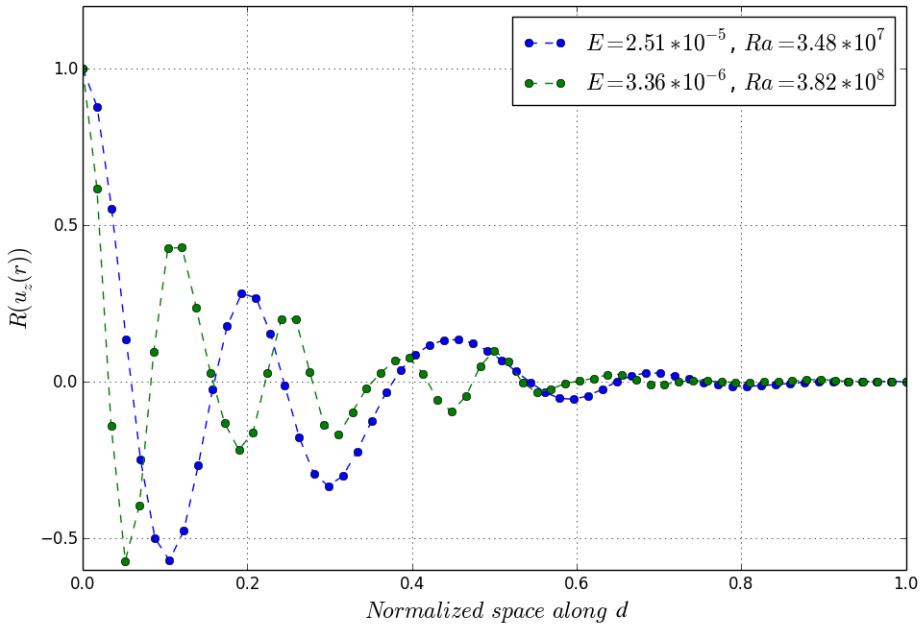

Figure 4.9: Spatial correlation function corresponding to 4.1 and 4.2 without magnetic field base on time averaged velocity.

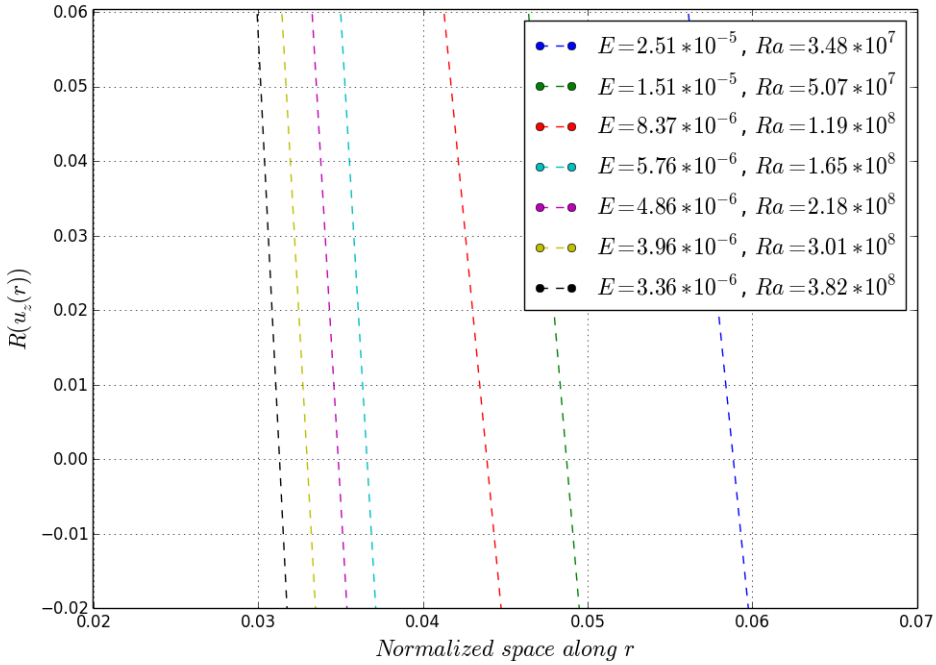

Figure 4.10: Zoom in the vicinity of the first zeros of the different spatial correlation functions we derived from our measurements

onset of convection in our rig without magnetic field. In our results, we did not observe any overstability effect which is not very surprising. Indeed this effect is supposed to happen for low Prandtl number whereas in the experiment the Prandtl number is relatively high. On figure 4.11 and 4.12, we compare the results obtained experimentally at onset to the results expected in the plane layer theory. As a first point, we note that on figure 4.11 the results obtained with water are consistent with the results obtained with Sulphuric Acid. This confirms the reliability of the setup. We also observe that we recover the scaling for the Rayleigh number such as $Ra = 22.3 \times E^{-1/3}$. This results prove that the scaling for the onset is very robust as it seems to support the large change in geometry between our cylinder and two infinite planes. We also obtain a consistent scaling for the number of structure expected at the onset $a_c = 0.5 \times E^{-1/3}$. Again it suggests that the scaling is generally very

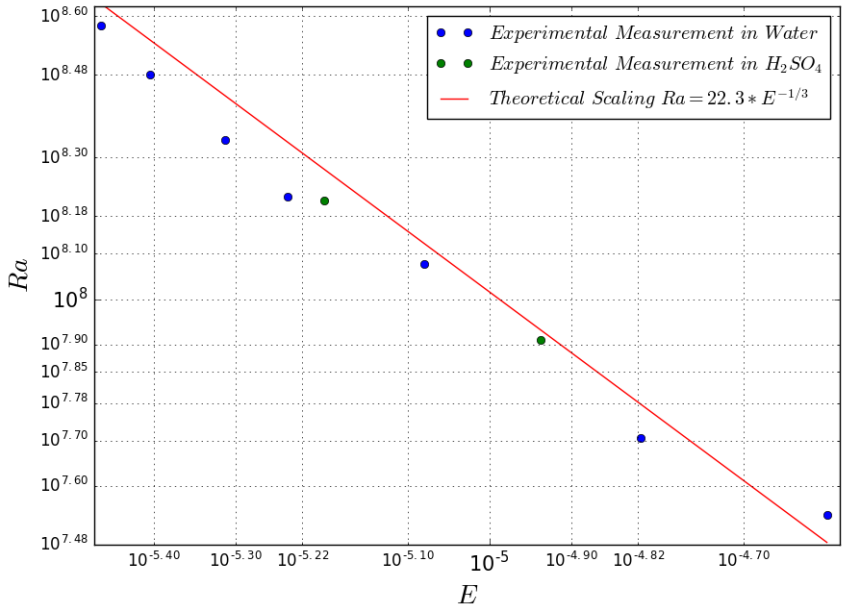

Figure 4.11: Comparison between measured Rayleigh number at onset and theoretically expected Rayleigh number. The theoretical values were obtained with the linear stability study introduced in Chapter 2. Our onsets were determined as the first Rayleigh number at which we could measure the flow. We note that our results are below the predictions which is not so surprising as our geometry is slightly different than two infinite plane layers.

robust. Nevertheless we note that the wavenumber of convective structures is significantly smaller than the theoretical wavenumber. The literature suggests that this result is a consequence of the aspect ratio of the Tangent Cylinder [33]. Unfortunately it is not possible to compare our results to this study as the author only worked in a range of Ekman number larger than 10^{-3}. Nevertheless this idea of the confinement induced by the Taylor-Proudman constraint has been overlooked in previous studies even though results show that the plane layer theory is not sufficient to depict the full picture of the onset of convection.

Our results point that the convection without magnetic field in the geometry of the Tangent Cylinder seems to behave as a mix between a confined

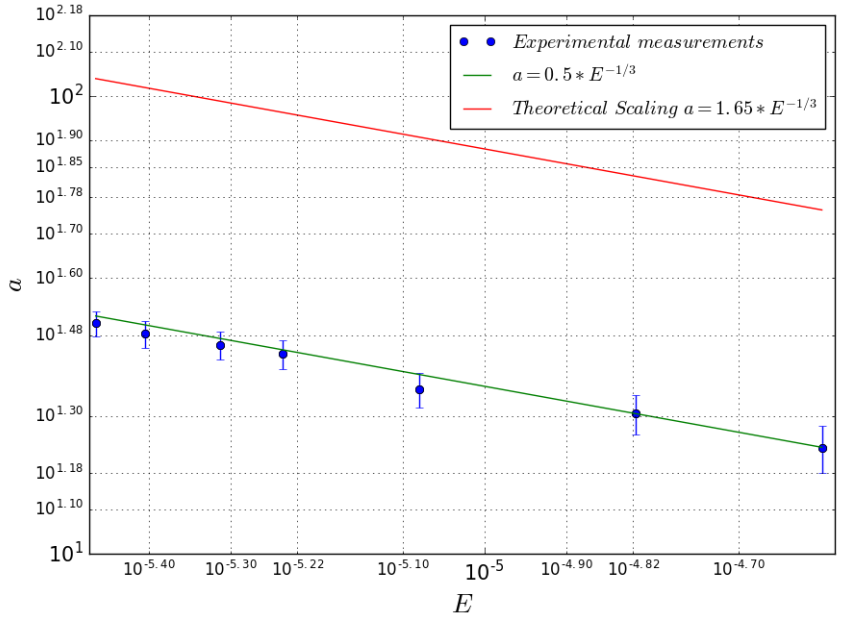

Figure 4.12: Comparison between experimental measurements of the wavelength determined with correlation functions and theoretical scalings with respect to the Ekman number. We note again that our results are below the predictions which is not so surprising as our geometry is slightly different than two infinite plane layers.

cylinder and a plane layer.

4.2.2 Supercritical regimes

In this section, we focus on regimes of convection that are beyond onset. We will first describe the evolution of the wave number with respect to the factor of criticality of the convection. Then we will introduce the secondary instabilities which can be observed for these regimes.

4.2.2.1 Evolution of the wave number beyond onset

General results In the next cases, we look at the behaviour above onset for non-magnetic cases in the vertical plane at two different values of the Ekman number. On figure 4.13 and 4.14, we present averages of the flow

velocity in time for different values of the Rayleigh number with $E = 1.15 \times 10^{-5}$ and $E = 6.36 \times 10^{-6}$ respectively. In these figures, we also highlight the correlation functions used to evaluate the number of structures present in the flow. In this parameter regime, the first results are that the convective structures become fatter as the Rayleigh number increases and that the number of structures decreases with the Ekman number as it was obtained for the onset of convection.

Scaling for the wave number above onset In order to give a general picture for the evolution of the wave number with the criticality of the flow, we introduce figures 4.15 and 4.16. In figure 4.15, we summarize the results presented in the previous paragraph. By comparing experimental and plane layer theory results, It highlights very clearly the effect of the still very strong confinement above onset and the effect of the Ekman number on the wave number. Moreover, an interesting point here is the effect of criticality on the wave number. Indeed we note that the number of structure tends to decrease as the supercriticality of the flow increases. On figure 4.16, we show the scaling obtained experimentally for the decrease of the wave number with the criticality. It is such as $a \times E^{4/3} = 1.8 \times 10^{-6} Ra^{-1/5}$.

4.2.2.2 Secondary instabilities

With figure 4.17, we illustrate the development of convection in the regime of $1.1 \times Ra_c$ and $12 \times Ra_c$ with $E = 1.15 \times 10^{-5}$. The results highlight that the flow goes from convection very close to onset to a stage with a strongly anticyclonic column system (figure 4.17j). At values close to the onset of convection we observe behaviour close to the onset reported by [33] with non-slip boundary condition at the top and bottom of their cylinder and adiabatic

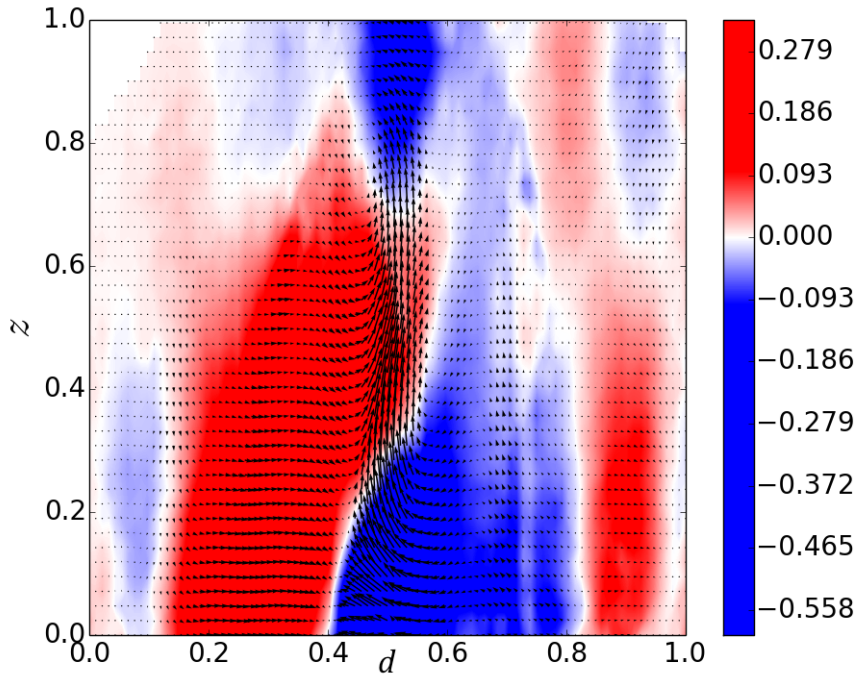

(a) $Ra = 1.52 \times Ra_c$

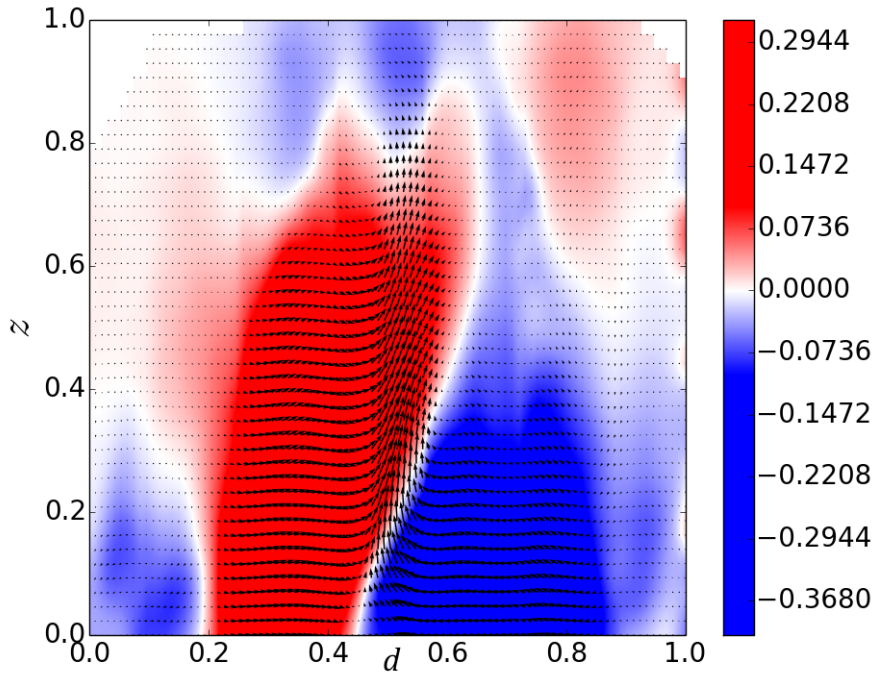

(b) $Ra = 2.45 \times Ra_c$

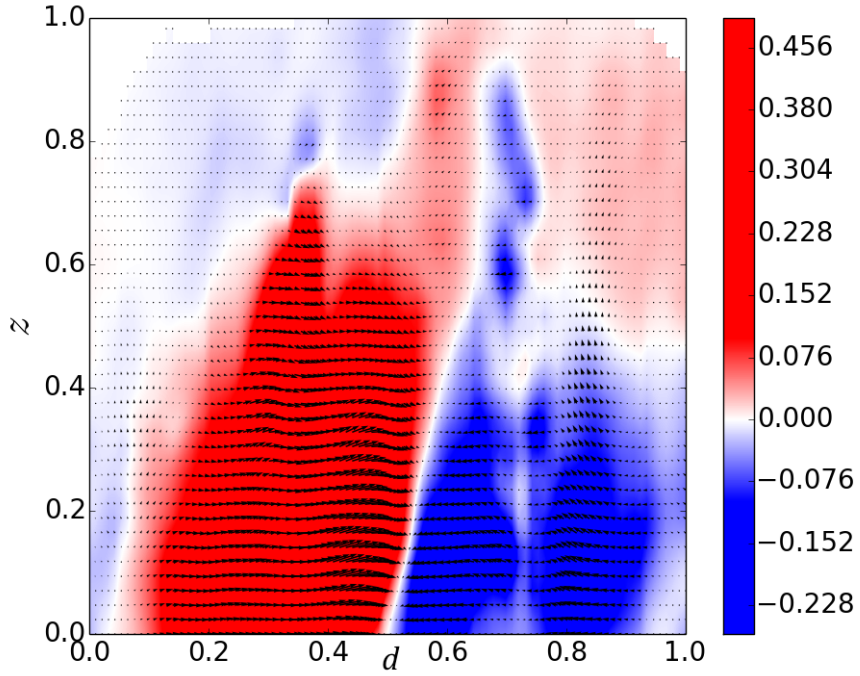

(c) $Ra = 6.14 \times Ra_c$

Figure 4.13: Average velocity fields (arrows) with u_r field in cm/s (colorbar) in the vertical plane for different Rayleigh numbers with $E = 1.15 \times 10^{-5}$ and $\Lambda = 0$. On the figures, d is normalized by the diameter of the heater and z is normalized by the height of liquid between the heater's surface and the dome. The cut at the top of the pictures and the pixel effect on the side are due to the discretization of the PIV software.

boundary conditions on the side walls. This is again in agreement with the fact that the Tangent Cylinder reacts as a confined cylinder rather than an infinite plane layer. For higher degrees of supercriticality, we observed several columns gathered around the center of the Tangent Cylinder. They correspond to what [8] qualifies as quasigeostrophic modes and [33] qualifies as aperiodic modes. By increasing even further the criticality of the system, we were able to see interaction between modes at the center of the Tangent Cylinder and at the side boundary. We call these side modes parietal modes; they corresponds to modes five and six described in [33]. In figures 4.17g and 4.17h, our system

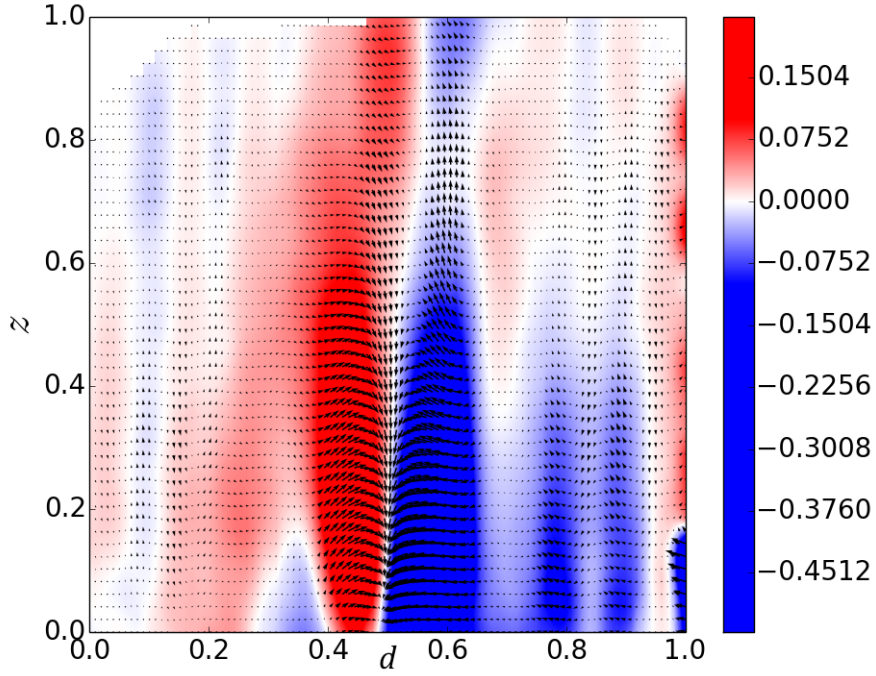

(a) $Ra = 1.80 \times Ra_c$

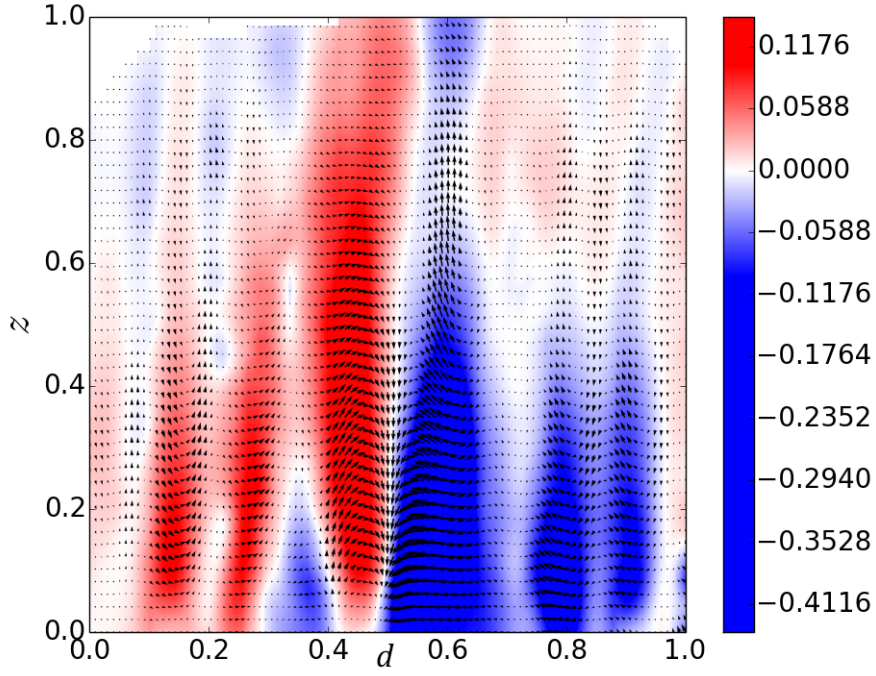

(b) $Ra = 2.95 \times Ra_c$

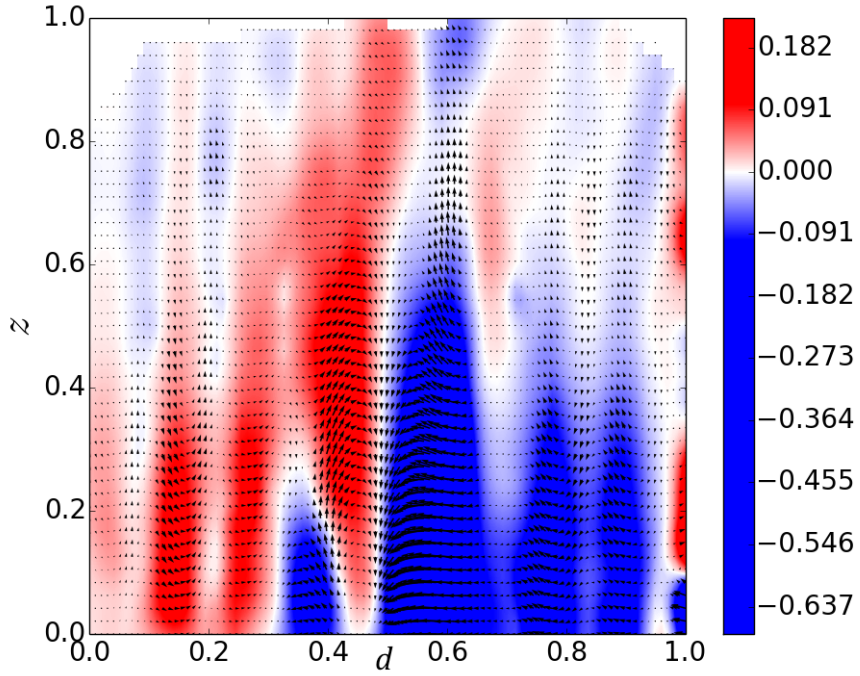

(c) $Ra = 5.96 \times Ra_c$

Figure 4.14: Average velocity fields (arrows) with u_r field (colorbar) in cm/s in the vertical plane for different Rayleigh numbers with $E = 6.36 \times 10^{-6}$ and $\Lambda = 0$. On the figures, d is normalized by the diameter of the heater and z is normalized by the height of liquid between the heater's surface and the dome. The cut at the top of the pictures and the pixel effect on the side are due to the discretization of the PIV software.

diverges from the results of [33]. Indeed we observe that flow goes beyond the Tangent Cylinder indicating that the Taylor-Proudman constraint is broken. Finally on figures 4.17i and 4.17j, we observe the last stage of the convection when it corresponds to a large central vortex. We note that for every degree of criticality there is a counterrotating background flow. This flow is known as the thermal wind and will be discussed in the next chapter but it is important for now to keep in mind that it changes rotation sign over the height of the cylinder. In other words, it is co-rotating near the bottom and counterrotating at the top.

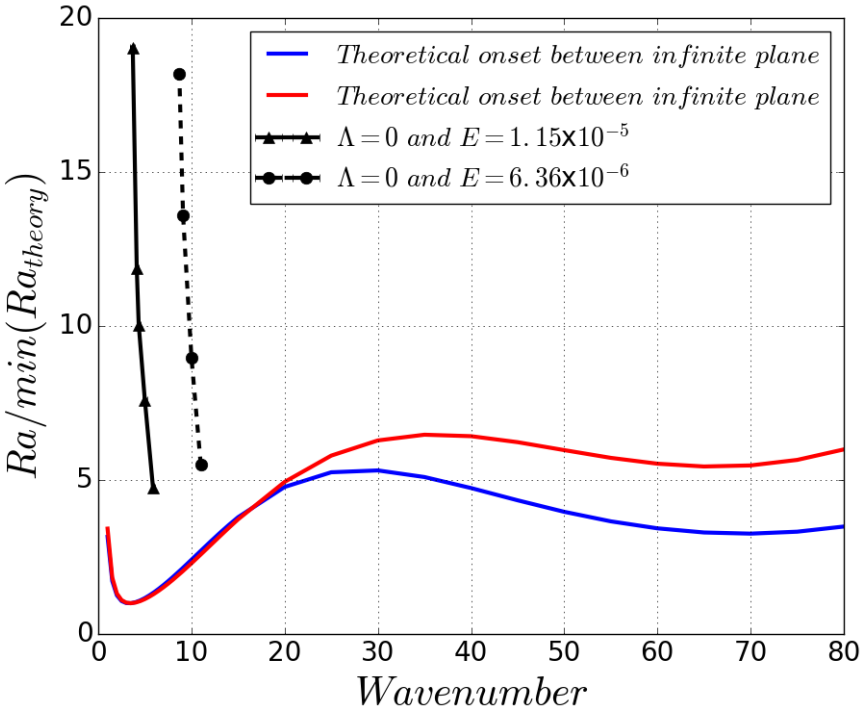

Figure 4.15: Comparison of the predicted wavelength to the wavelength obtained experimentally without magnetic field. The blue line corresponds to the theoretical onset obtained with linear theory for $\Lambda = 0.58$ and $E = 1.15 \times 10^{-5}$. The red line corresponds to the theoretical onset obtained with linear theory for $\Lambda = 1.12$ and $E = 1.15 \times 10^{-5}$.

Now, we investigate the flow at a smaller Ekman number, $E = 6.36 \times 10^{-6}$. In this case, we managed to record Rayleigh numbers in the range: $Ra \in [1.35 \times Ra_c, 12.91 \times Ra_c]$. In figure 4.18, we observe some differences than what we observe for larger Ekman number. At first, we can see that the structures in the flow are much smaller than before. Although the confinement effect is still very strong, the direct consequence is that the onset is less in agreement with [33]. Interestingly when the criticality increases, we observe modes that correspond to the modulated modes describe by [33]. The appearance of these spiraling modes is the consequence of the Taylor-Proudman constraint becoming more rigid at lower Ekman number. Then again we report a mix between parietal mode and central mode on figures 4.18g and 4.18h leading to the rupture of

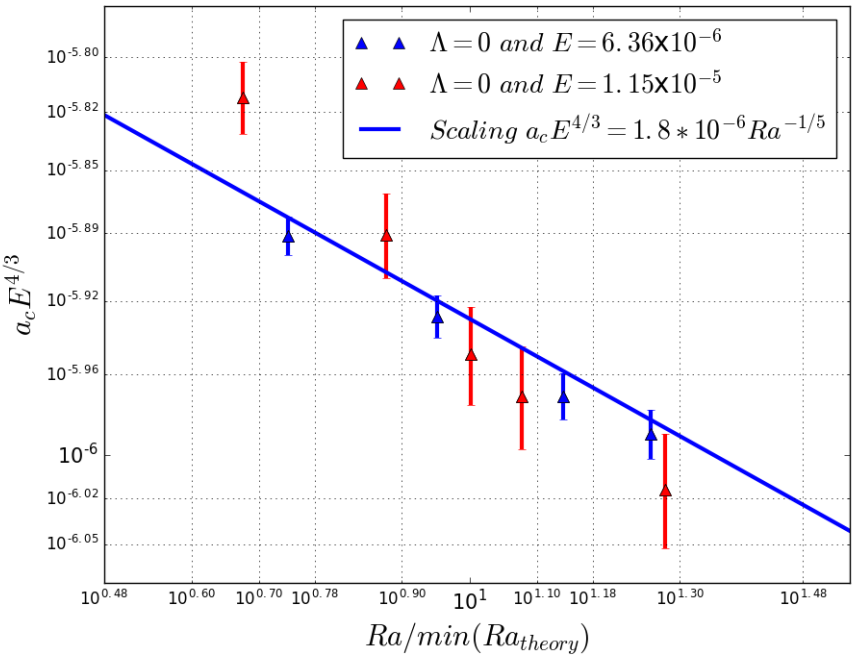

Figure 4.16: Wavelength obtained experimentally above the onset of convection and without magnetic field

the Taylor-Proudman constraint on figures 4.18i and 4.18j.

4.3 Magnetic Convection

In this section, we are exclusively interested in the effect of the magnetic field on the convection. Following the previous section we will first discuss the onset of convection. Then we will focus on supercritical regimes.

4.3.1 Onset of Convection

Here, we present the results obtained very near the onset of convection for Elsasser number, $\Lambda > 0$. We introduce cases close to onset but unfortunately never under the onset as the magnetic mode can be especially low as shown in the theoretical chapter. Indeed the corresponding temperature differences

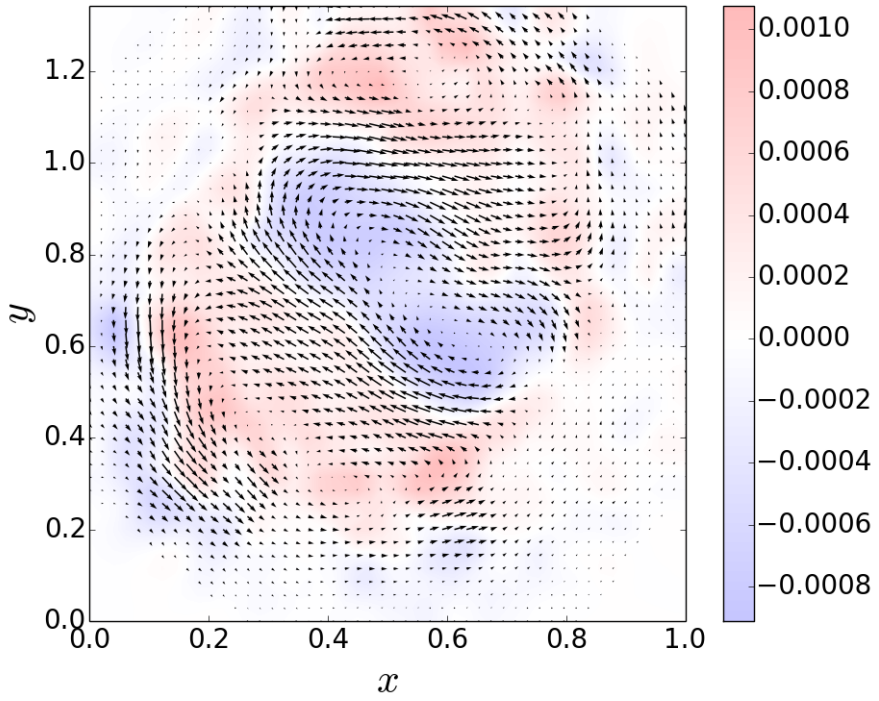

(a) $Ra = 1.13 \times Ra_c$

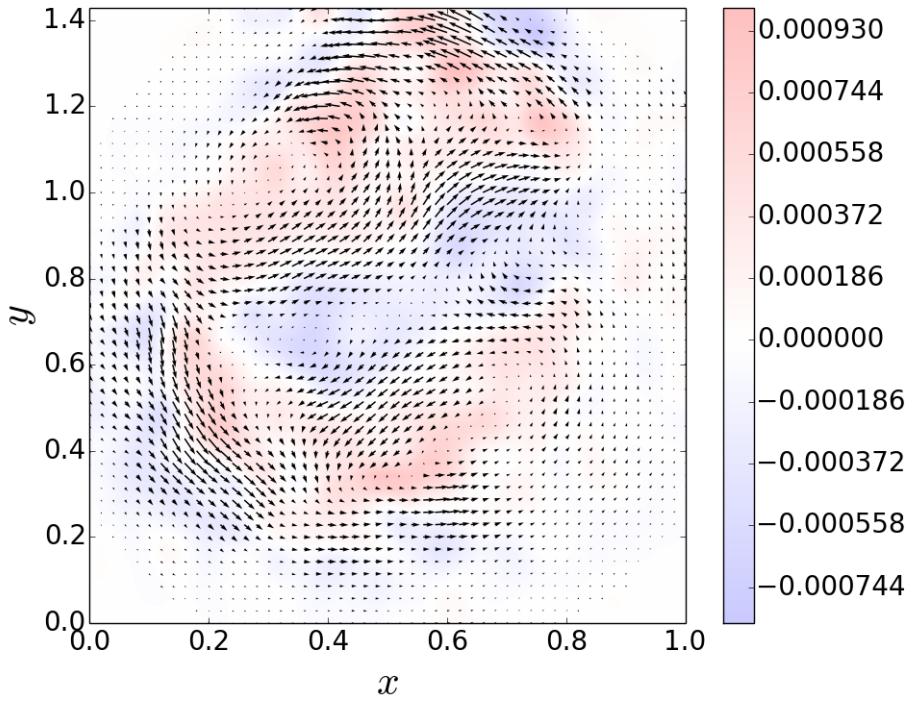

(b) $Ra = 1.25 \times Ra_c$

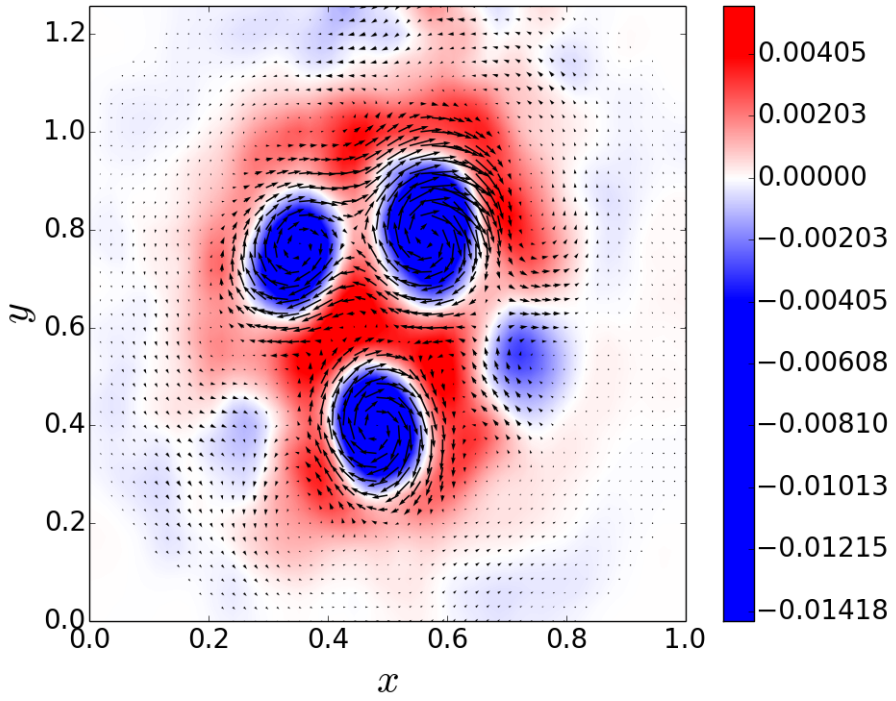

(c) $Ra = 2.26 \times Ra_c$

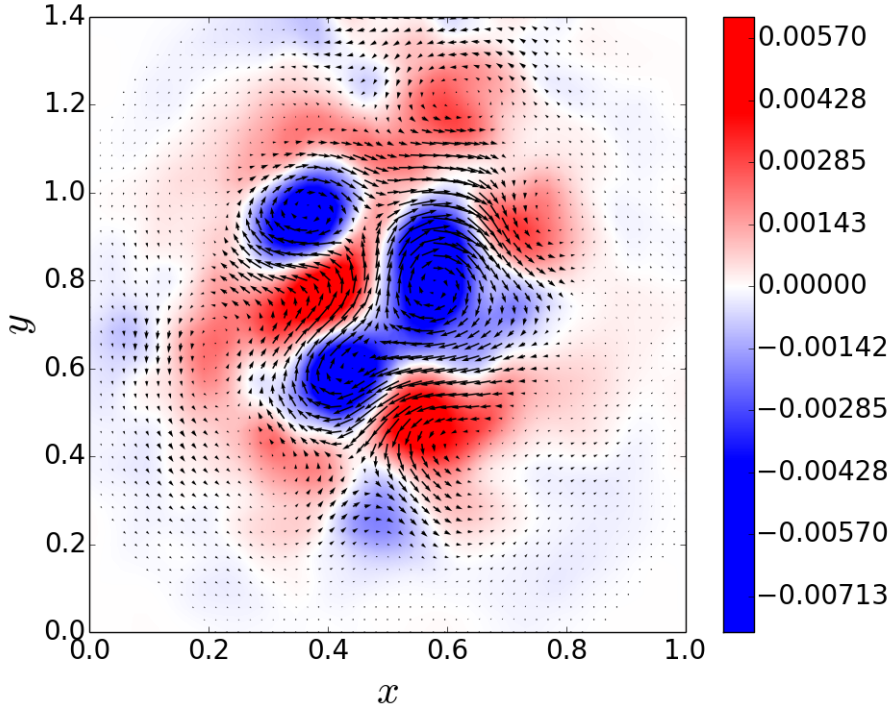

(d) $Ra = 2.39 \times Ra_c$

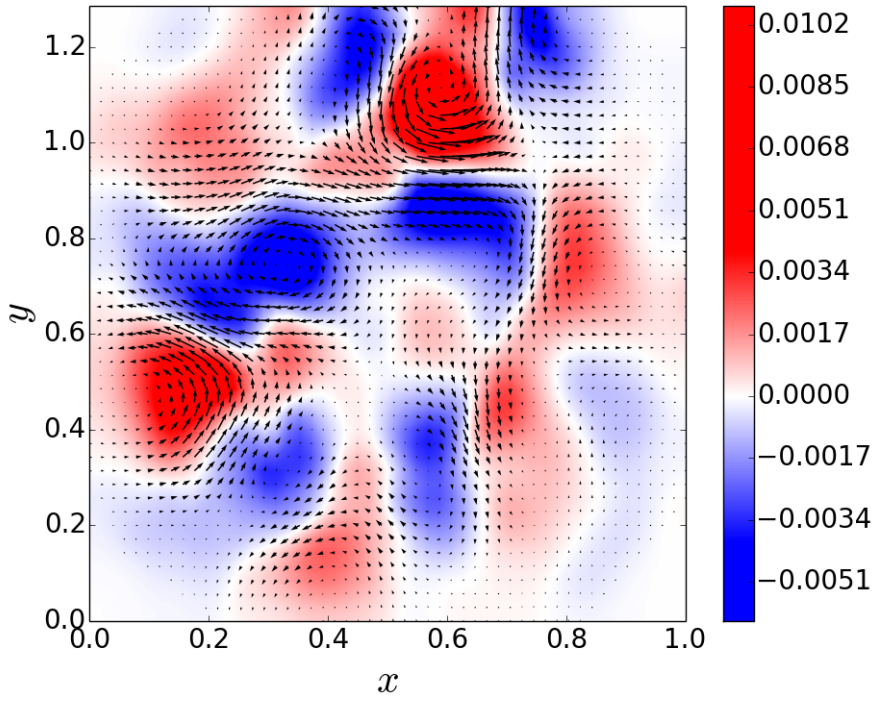

(e) $Ra = 4.58 \times Ra_c$

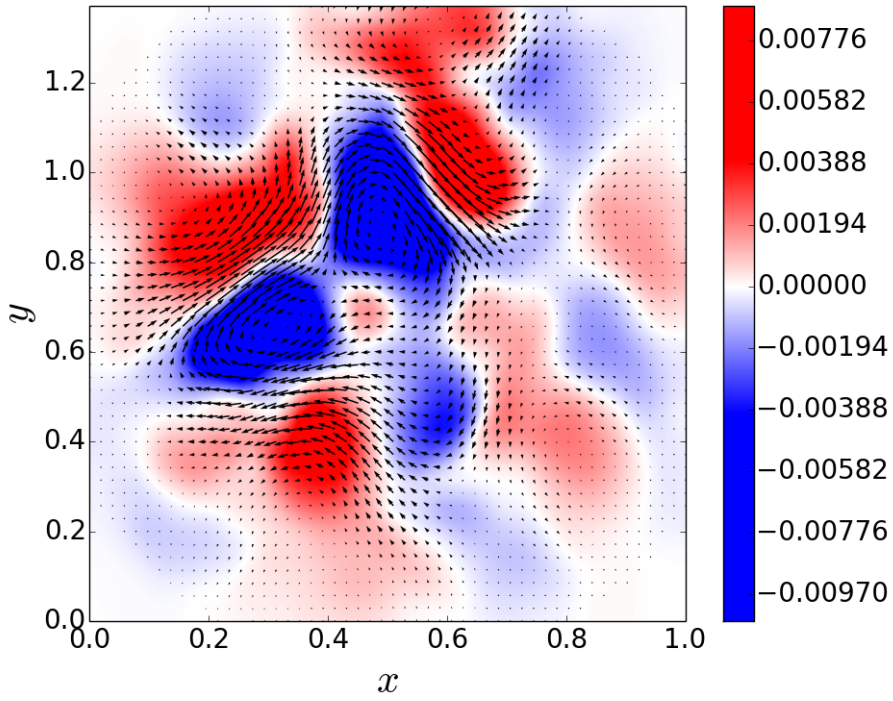

(f) $Ra = 4.77 \times Ra_c$

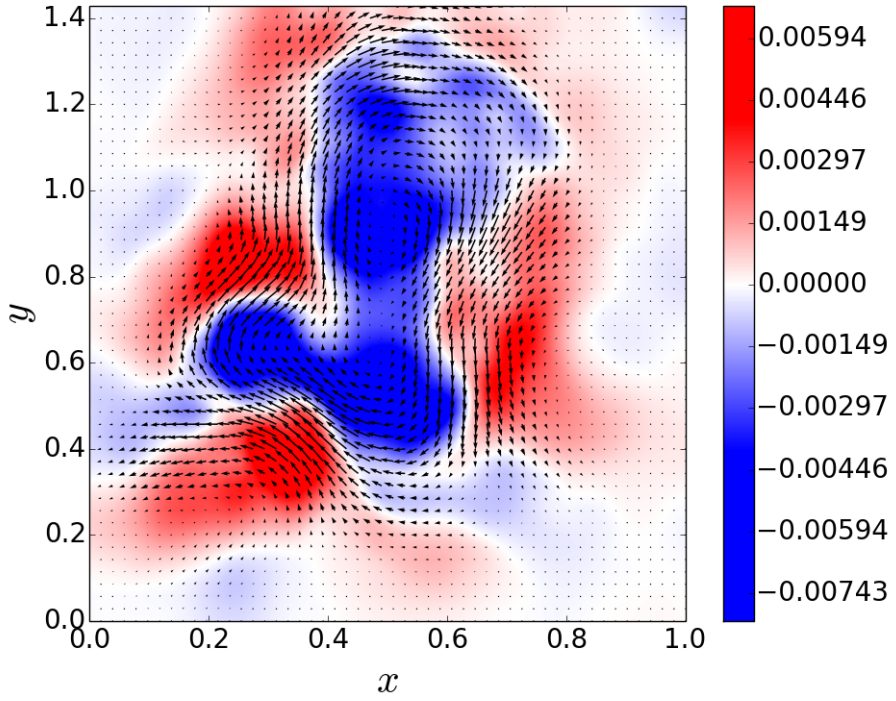

(g) $Ra = 7.29 \times Ra_c$

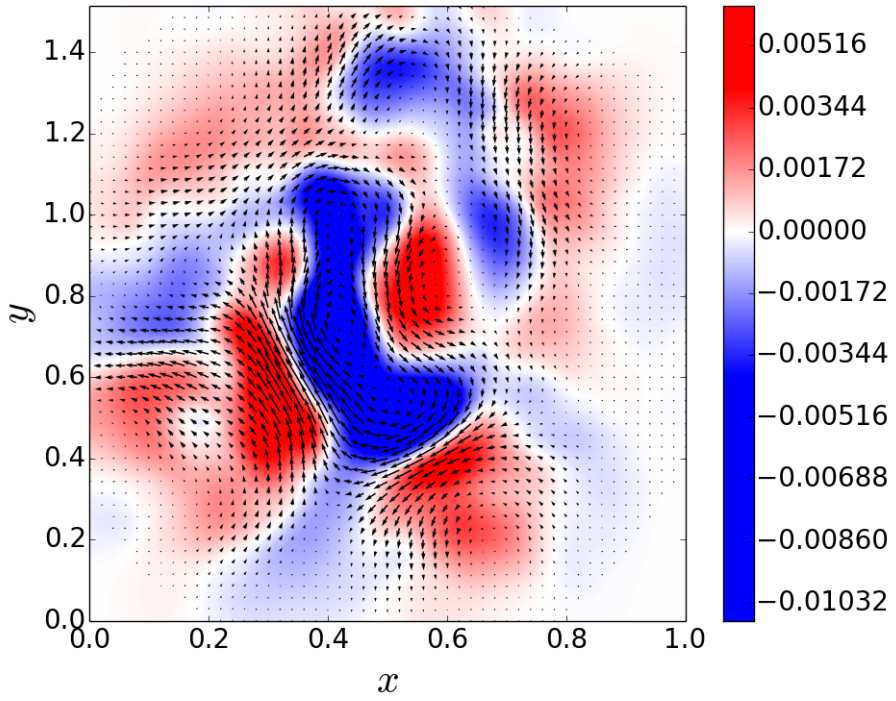

(h) $Ra = 9.25 \times Ra_c$

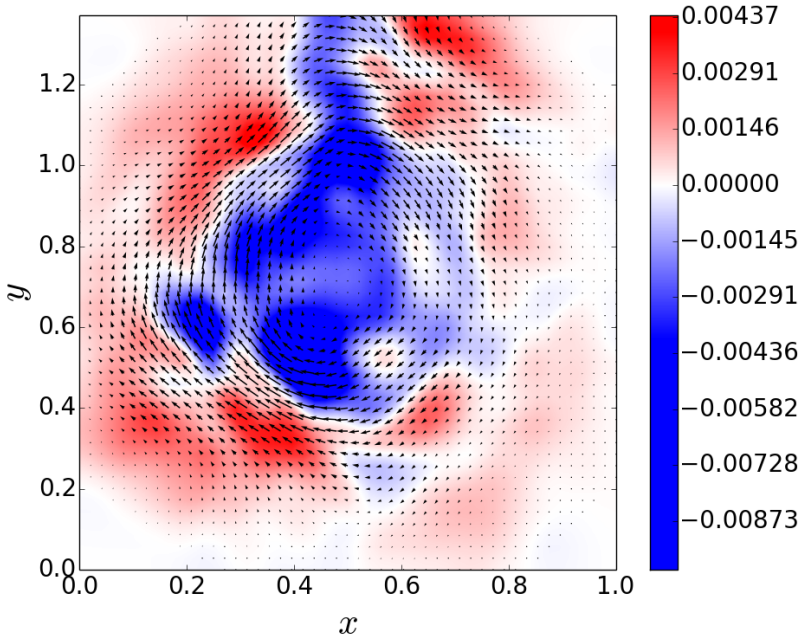

(i) $Ra = 11.94 \times Ra_c$

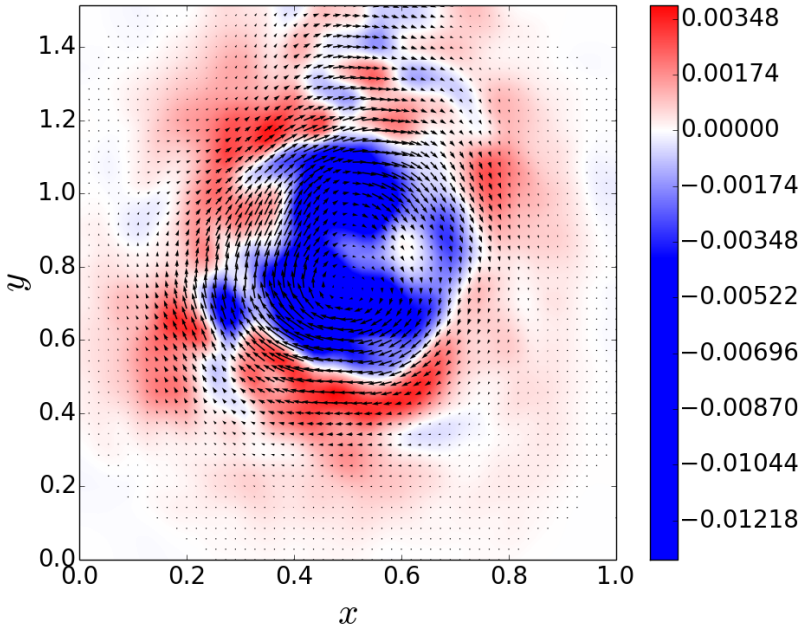

(j) $Ra = 12.27 \times Ra_c$

Figure 4.17: Average velocity fields (arrows) with vorticity field (colorbar) in the horizontal plane for different Rayleigh numbers with $E = 1.15 \times 10^{-5}$ and $\Lambda = 0$ for 68° latitude. On the figures, x and y are normalized by the diameter of the heater d. The center of the heater corresponds to the center of the pictures. Additionally, y is often larger than 1 because the area of interest in the PIV software was larger than the heater in that direction.

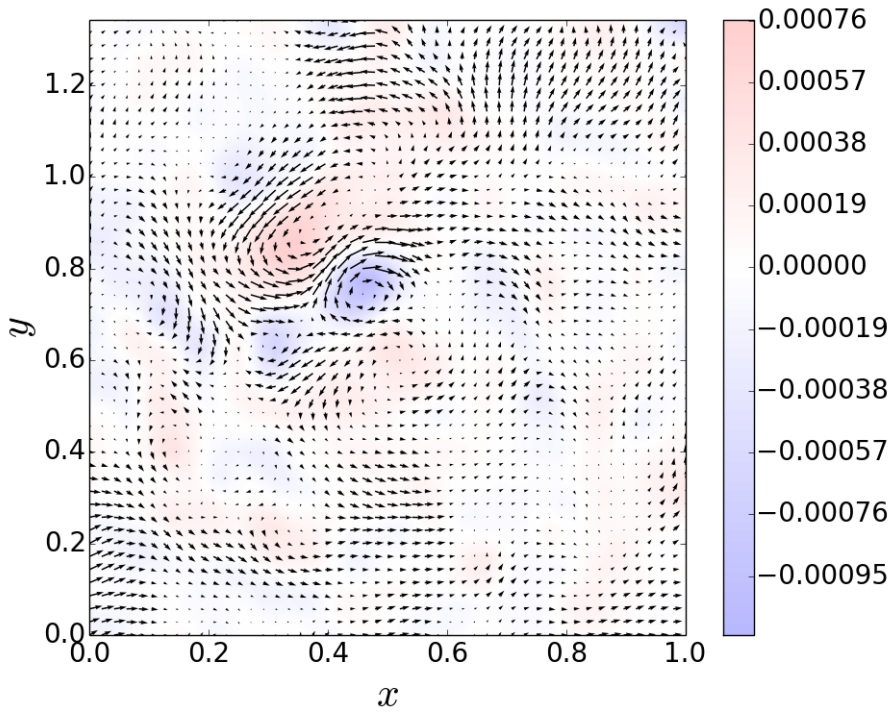

(a) $Ra = 1.35 \times Ra_c$

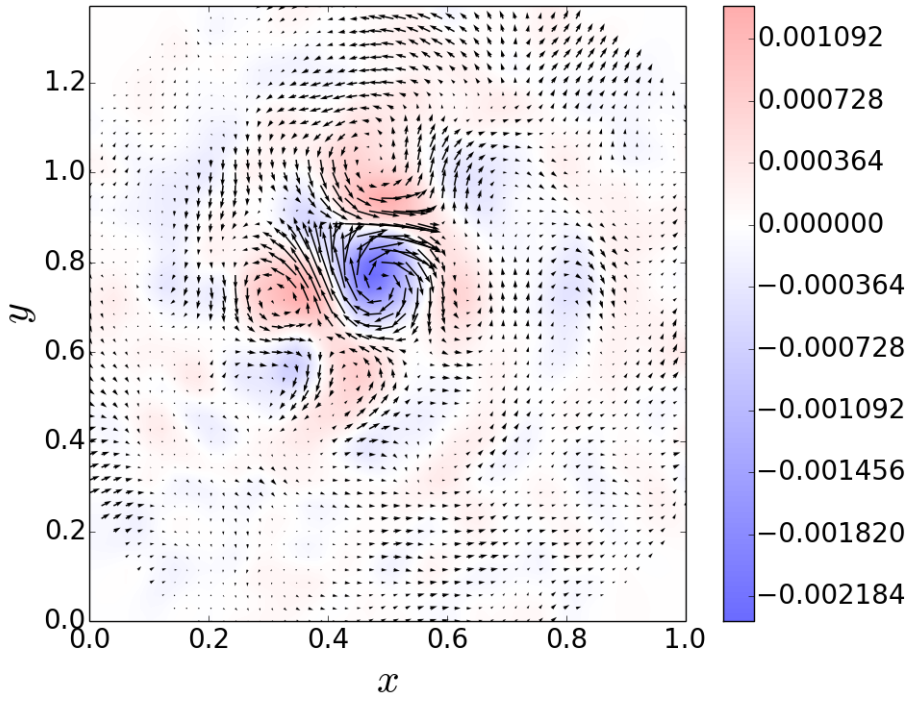

(b) $Ra = 1.57 \times Ra_c$

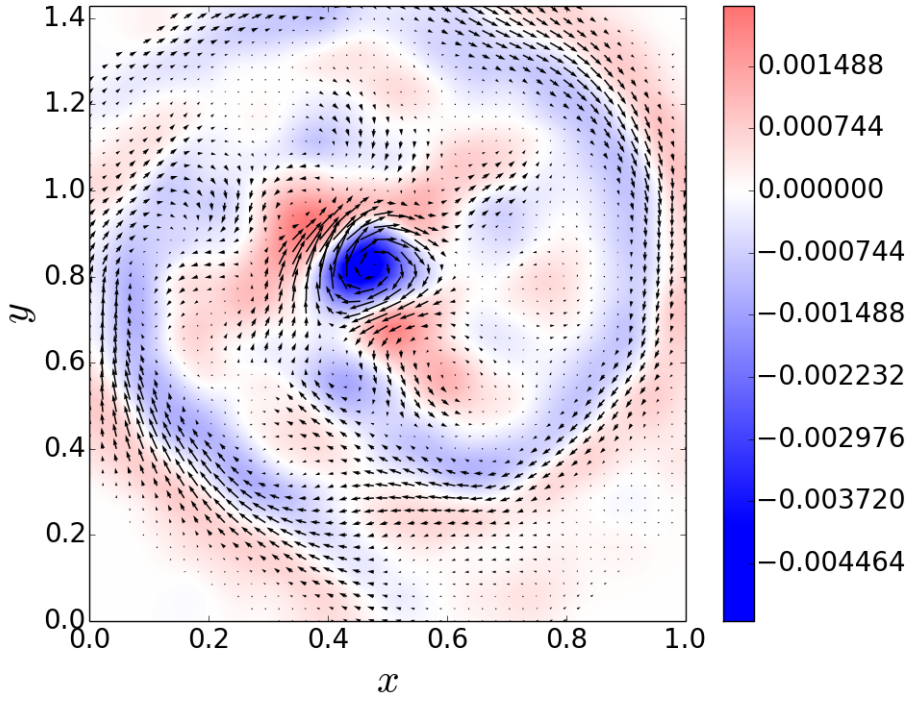

(c) $Ra = 2.26 \times Ra_c$

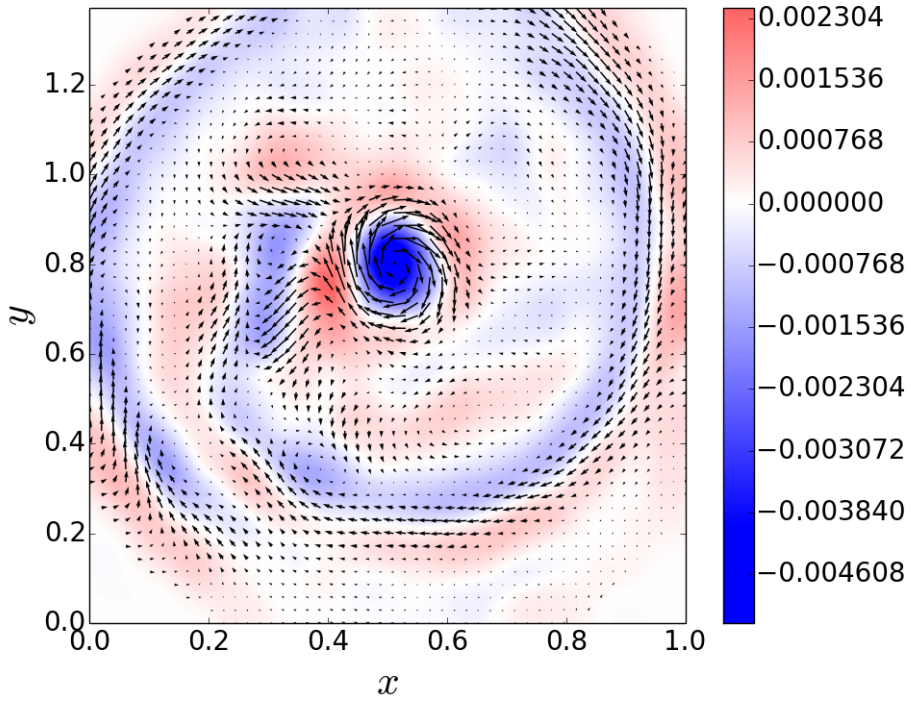

(d) $Ra = 2.39 \times Ra_c$

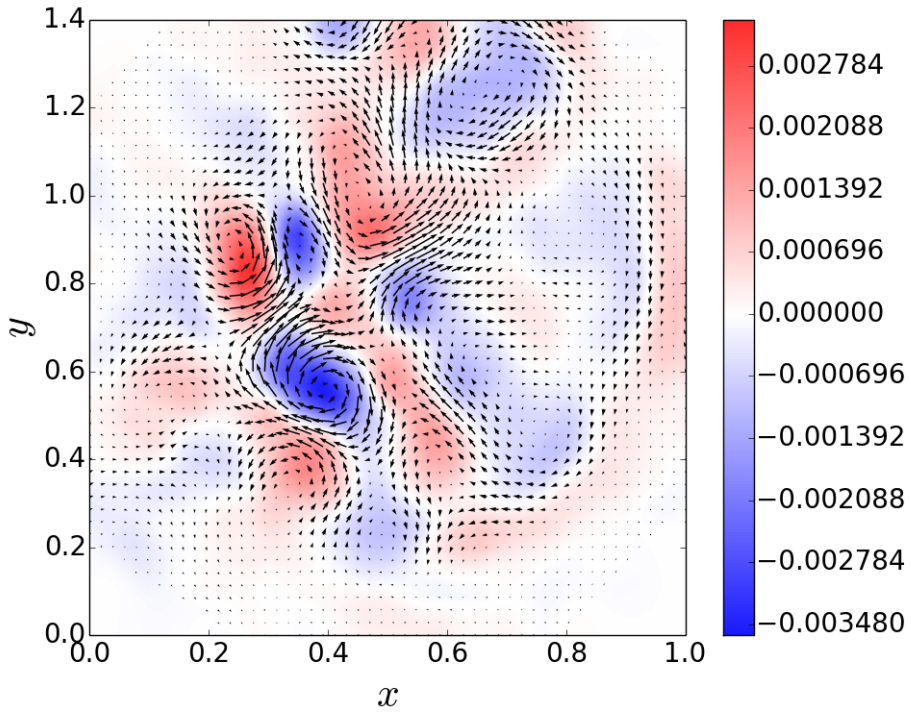

(e) $Ra = 3.32 \times Ra_c$

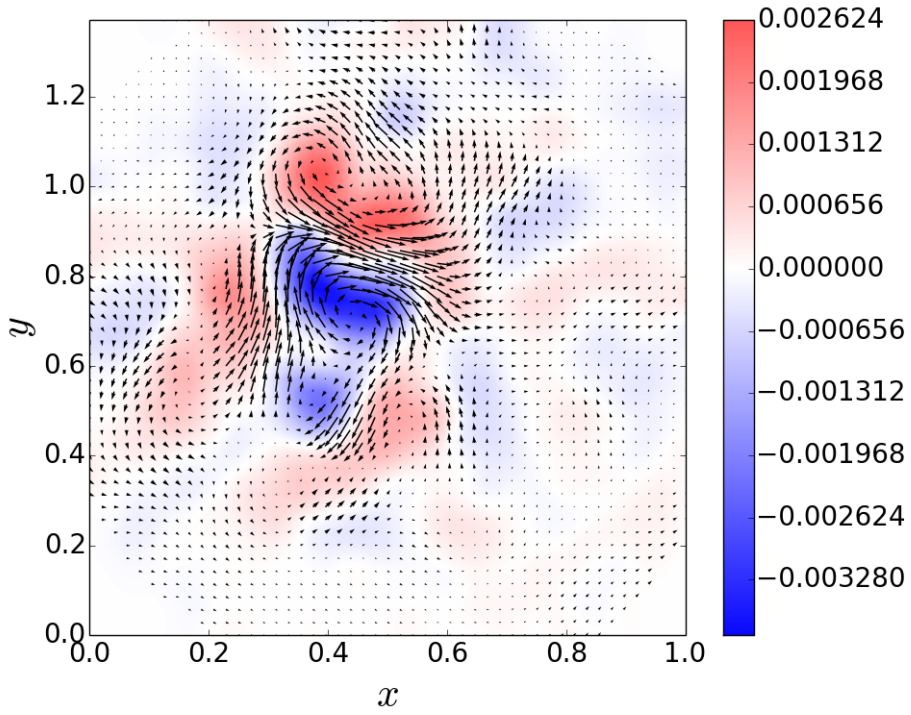

(f) $Ra = 3.47 \times Ra_c$

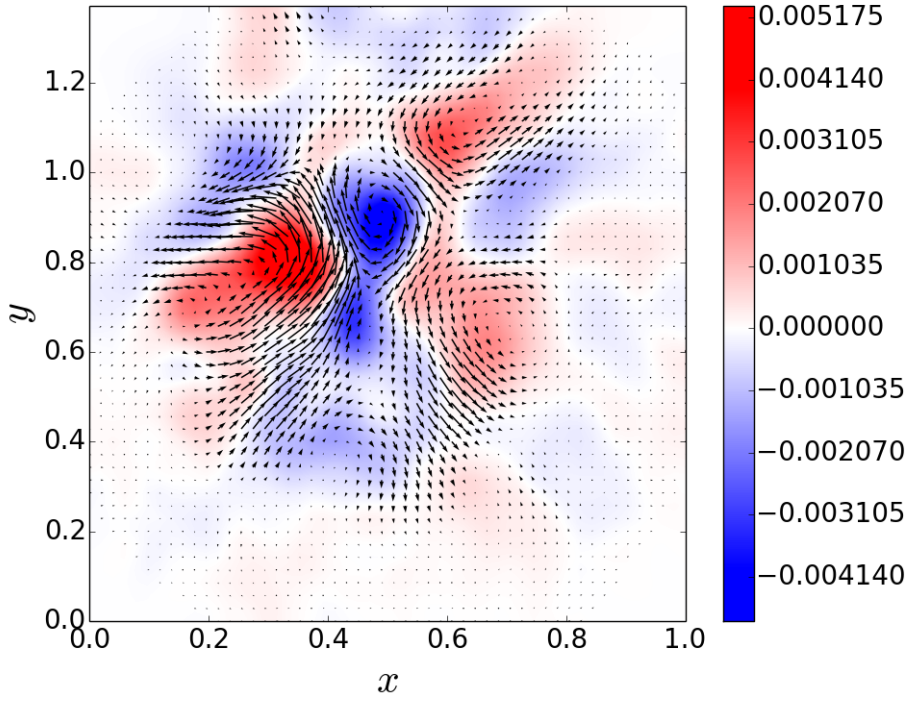

(g) $Ra = 5.40 \times Ra_c$

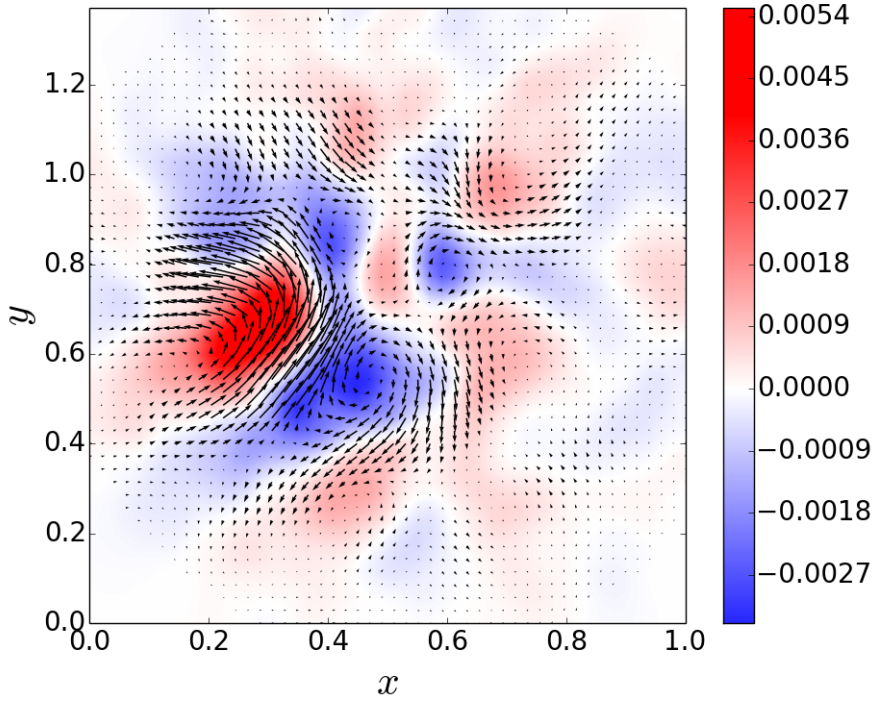

(h) $Ra = 5.58 \times Ra_c$

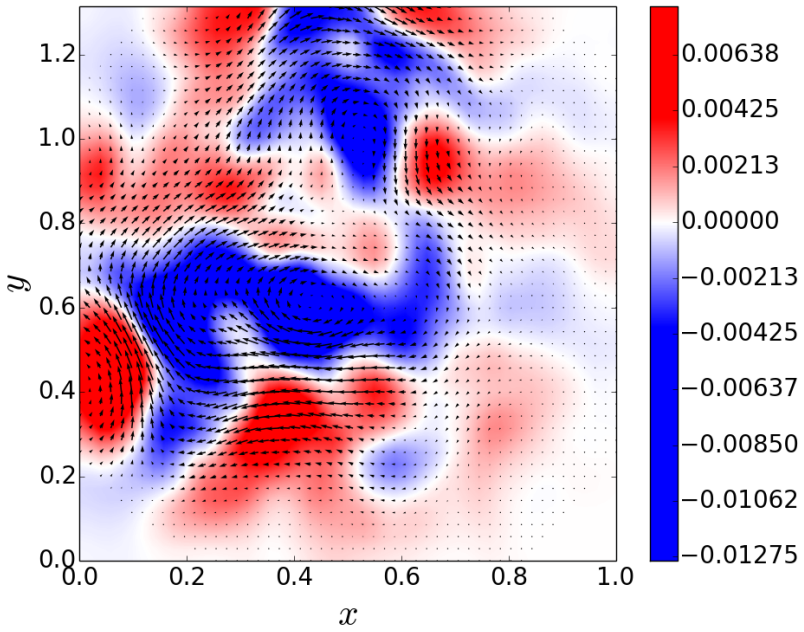

(i) $Ra = 9.17 \times Ra_c$

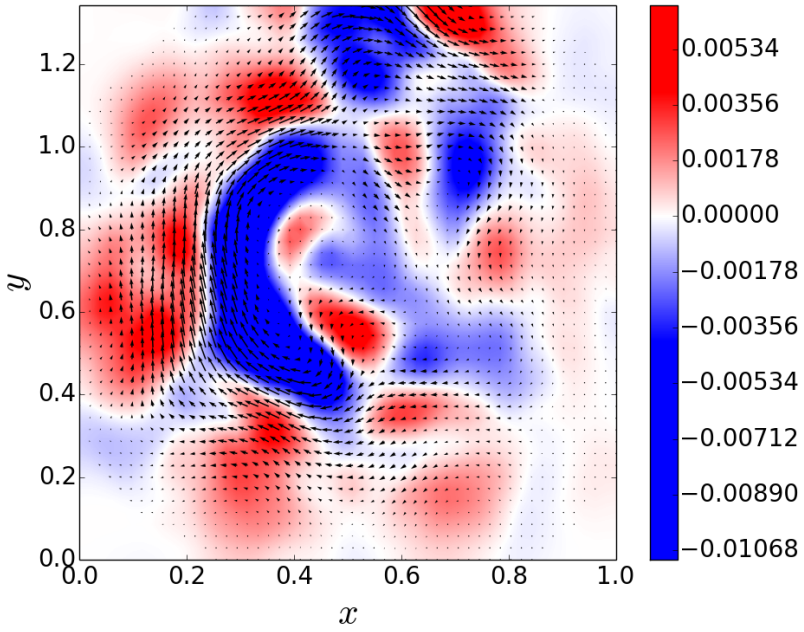

(j) $Ra = 12.91 \times Ra_c$

Figure 4.18: Average velocity fields (arrows) with vorticity field (colorbar) in the horizontal plane for different Rayleigh numbers with $E = 6.36 \times 10^{-6}$ and $\Lambda = 0$ for 68° latitude. On the figures, x and y are normalized by the diameter of the heater d. The center of the heater corresponds to the center of the pictures. Additionally, y is often larger than 1 because the area of interest in the PIV software was larger than the heater in that direction.

between the heater and the dome surface are below 1°K, which our setup cannot reliably produce. Therefore, we were unable to derive scaling for the wavelength or the critical Rayleigh number with respect to the Ekman number. Additionally, we note that overstability was not observed in our results. Although this was observed in liquid metal experiment by Aurnou [10], we can be explained to our findings by the large viscous Prandtl number of the sulphuric acid.

4.3.1.1 Consistency with the plane layer theory

With figure 4.19, we show results obtained in the vertical plane. They highlight the effect of the magnetic field for values of the Rayleigh number close to the onset of convection, between 1.3 and 2 times critical. Our results were obtained for four values of the Elsasser number, $\Lambda = [0.14, 0.33, 0.58, 1.12]$. These cases illustrate the fact that, for this regime of Elsasser numbers, the magnetic field induces significant thickening of the convective structures.

In figure 4.20, we compare the wave number obtained experimentally with the wave number predicted by the plane layer theory. We find that there is a good agreement between the two. Indeed the theory predicts a wave number of 3.4 approximately in these conditions and we recover a wave number of approximately 3 in the experiment. Such results suggest that the magnetic cases are not as sensitive to the effect of the confinement as the non-magnetic cases, although figure 4.8 showed that the magnetic cases should have a precession at onset. This is an effect of the confinement not predicted in the plane layer geometry. Finally figure 4.20 highlights the difference between magnetic and non-magnetic cases. In fact, we observe a jump between wave numbers 11 for Elsasser number equal zero to wave numbers zero to 3 at larger Elsasser numbers.

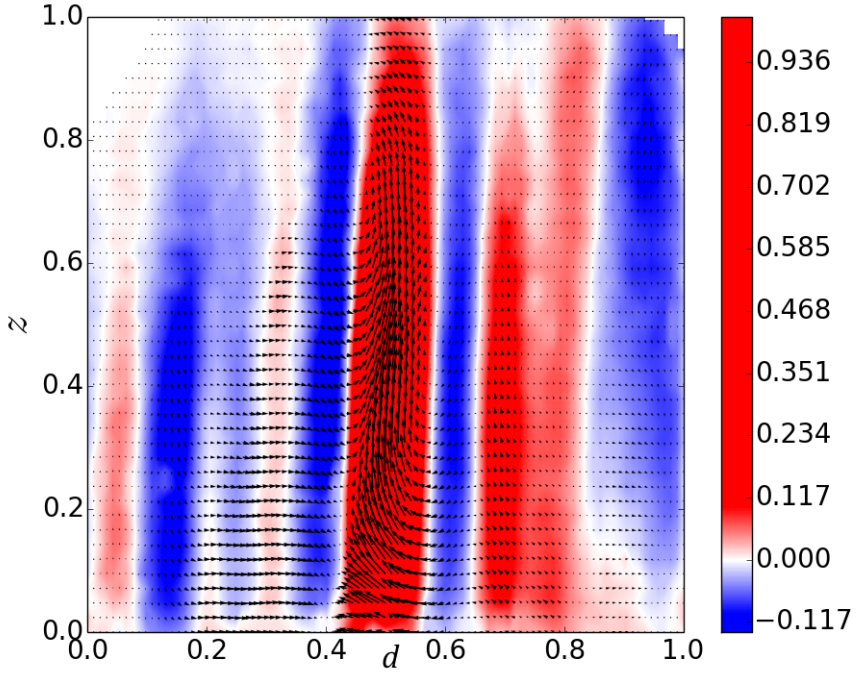

(a) $Ra = 1.37 \times Ra_c$ and $\Lambda = 0.14$

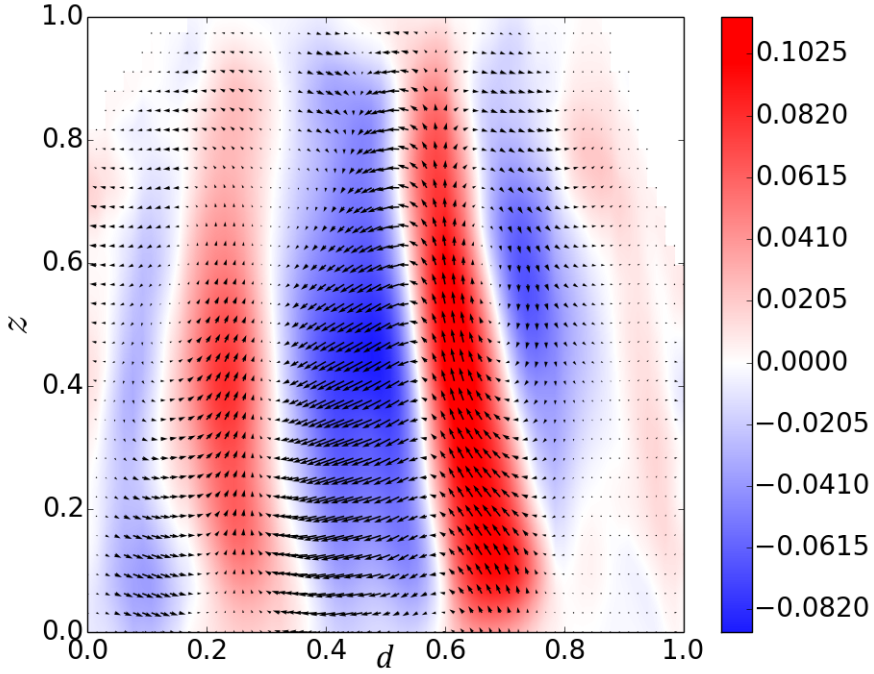

(b) $Ra = 1.63 \times Ra_c$ and $\Lambda = 0.33$

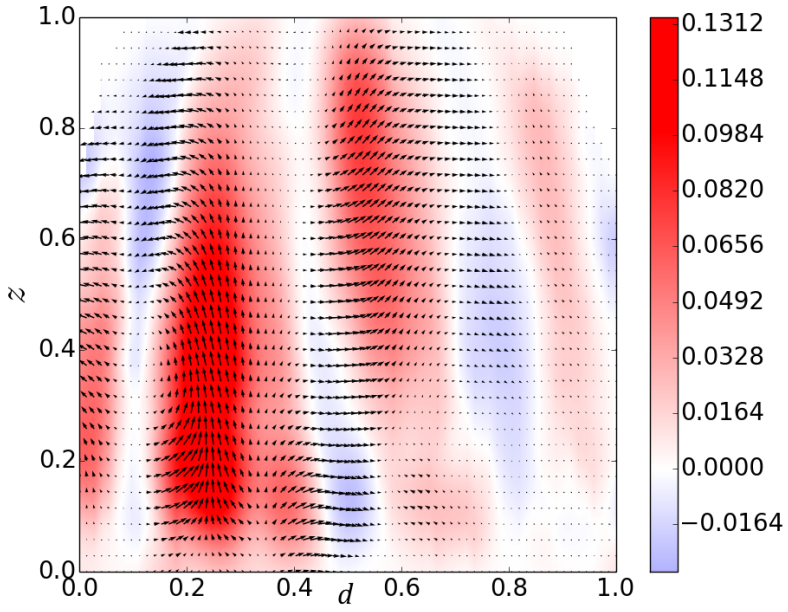

(c) $Ra = 1.88 \times Ra_c$ and $\Lambda = 0.58$

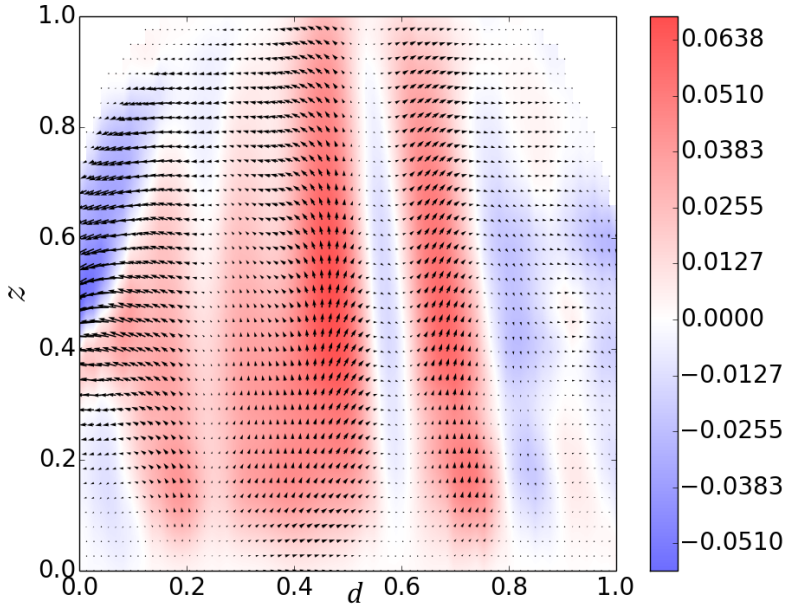

(d) $Ra = 1.92 \times Ra_c$ and $\Lambda = 1.12$

Figure 4.19: Average of the velocity field (arrows) and z-component of the velocity (color) in time with Ekman numbers, $E = 1.15 \times 10^{-5}$, and for four different values of Elsasser number near the onset of convection. On the figures, d is normalized by the diameter of the heater and z is normalized by the height of liquid between the heater's surface and the dome. The cut at the top of the pictures and the pixel effect on the side are due to the discretization of the PIV software.

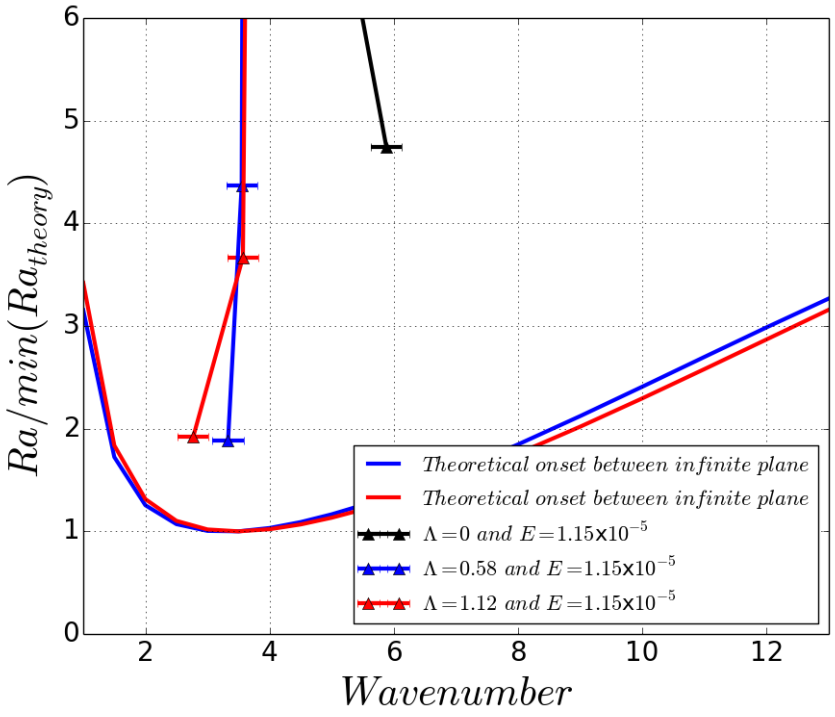

Figure 4.20: Comparison of the predicted wavelength to the wavelength obtained with magnetic field. The blue line corresponds to the theoretical onset obtained with linear theory for $\Lambda = 0.58$ and $E = 1.15 \times 10^{-5}$. The red line corresponds to the theoretical onset obtained with linear theory for $\Lambda = 1.12$ and $E = 1.15 \times 10^{-5}$

4.3.1.2 Transition from viscous to magnetic convection

In order to emphasize in our results, the clear jump in structure size that we were able to observe, we present the evolution of the wave number with respect to the Elsasser number in figure 4.21. Experimental results are compared to the plane layer theory results. The structure size in the magnetic case varies very little in supercritical regime, hence the values obtained closely after onset can be considered close to the values at onset. Similarly to the case without magnetic field, the wave numbers were extracted from the minimal value of r for which the correlation function of the velocity is equal to zero. For figure 4.21, we obtained results from correlation on components of the velocity in

the r and the z-direction. On this figure, we observe that in the theoretical case there is a brutal jump in size structure that occurs between $\Lambda = 0.16$ and $\Lambda = 0.18$. In plane layer theory, the wavenumber of structures is reduced from 72 to 3.4. Our experimental results show a significant effect of the magnetic field for Elsasser number larger than 0.2. Indeed the number of convective structures is divided by almost four in the case of correlation with velocity in the z-direction and by a factor two using correlation of velocity in the r-direction. This confirms the general results obtained in plane layer geometry by [43] as the authors were able to qualitatively observe that the size of the column at onset with a magnetic field are significantly larger. Additionally, the jump highlighted in our experimental results is a lot smaller than the theoretical jump. We attribute this effect to the confinement of the cylinder in our geometry for non-magnetic and very weakly magnetic cases. Indeed, on one hand, for non-magnetic cases, the viscous wave number is clearly lower than the predicted one (around 11 instead of 72). On the other hand, for magnetic cases, we observe a wave number very similar to the one obtained for theoretical prediction (in both cases around 3). This leads to the following conclusion: the structure of the convection in magnetic case is not strongly affected by the boundary conditions of the cylinder. Finally, we interestingly note the value of the Elsasser number, at which the jump occurs, seems to be fairly similar whether the convection is confined or not.

4.3.1.3 Polar vortex in the horizontal plane

In this section, we present a magnetic case obtained for at the same Ekman numbers as previously ($E = 1.15 \times 10^{-5}$) and an Elsasser number of 0.33. The result we show corresponds to measurements closest to the onset with the magnetic field. Figure 4.22 illustrates the behaviour of the flow for moderate

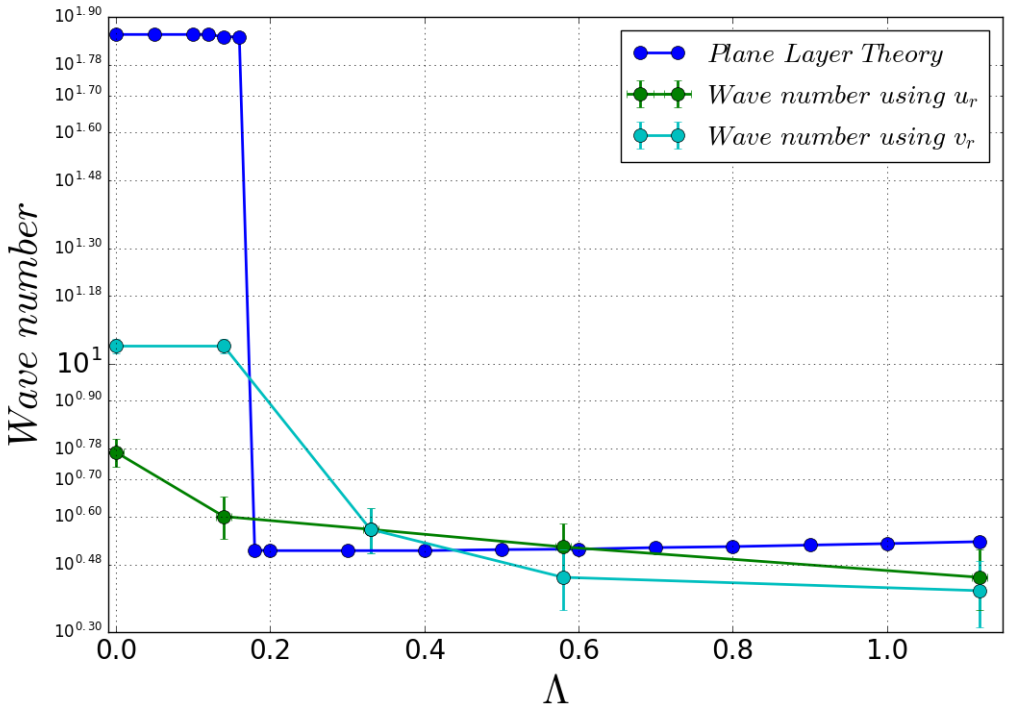

Figure 4.21: Effect of the Elsasser number on the number of structure around onset with Ekman number $E = 1.15 \times 10^{-5}$. The green points correspond to wave numbers extracted from correlation on the z-component of the velocity. The blue points correspond to wave numbers extracted from correlation on the r-component of the velocity.

Elsasser number $\Lambda = 0.33$. When $\Lambda = 0.33$, the results presented occurred for a Rayleigh number 1.67 times the Rayleigh number at the theoretical onset. This case shows that the flow is organized around one large off-axis structure corresponding to field measurement and numerical simulations [36][56]. In [36], the authors were able to show the existence of a strong vortex in the polar region; their results were obtained thanks to satellite measurement of the Earth magnetic field. In [56] thanks to numerical simulations, the authors attributed the effect observed in [36] to the magnetic field. This structure is known as the polar vortex. Nevertheless it has never been observed experimentally. Our results highlight the first experimental visualization of this mechanism. Indeed they represents an isolated off-axis vortex which is consistent with the

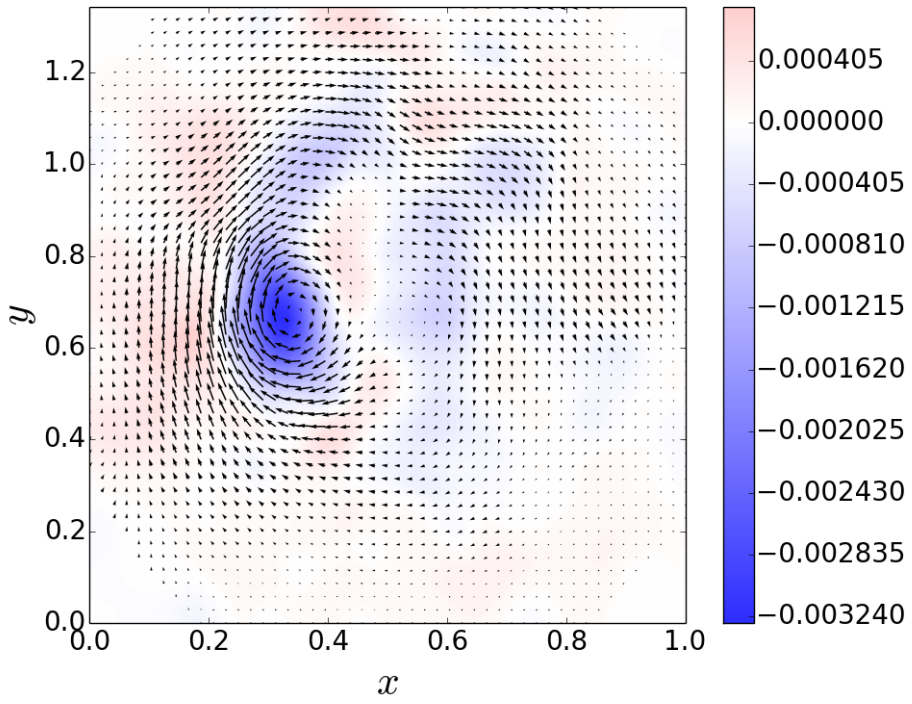

Figure 4.22: Average of the velocity field (arrows) and vorticity (color) in time at $Ra = 1.67 \times Ra_c$, $E = 1.15 \times 10^{-5}$ and $\Lambda = 0.33$. On the figure, x and y are normalized by the diameter of the heater d. The center of the heater corresponds to the center of the pictures. Additionally, y is often larger than 1 because the area of interest in the PIV software was larger than the heater in that direction.

literature and can be considered as the polar vortex.

4.3.2 Supercritical regimes

In this section, we are interested in the behaviour of the flow above the onset of convection. We will first describe the evolution of the number of structure in the flow with respect to the factor of criticality of the flow. Then we will compare the development of the flow with the several secondary instabilities observed without magnetic field.

4.3.2.1 Evolution of the wave number beyond onset

The results presented here correspond to two magnetic cases with an Elsasser number in range of the Earth's Elsasser number ($\Lambda_{Earth} \in [0, 1]$). As shown before, these cases corresponds to a magnetically controlled case for the onset. Figure 4.23 illustrates several averages in time of the flow in the vertical plane with $\Lambda = 0.58$ and $E = 1.15 \times 10^{-5}$ for Rayleigh number going from four times critical to 14 times critical. It shows as well the correlation function used in each case to determine the number of structures in the flow. Figure 4.24 shows time averages of the flow with the corresponding correlation functions for Elsasser number $\Lambda = 0.88$ and Ekman number $E = 6.36 \times 10^{-6}$. The first obvious result is the enlargement of the convective structures for lower Rayleigh numbers. Indeed, instead of thin and numerous convective structure, we observe only very few large structures. Again this results highlights the great discrepancy between viscous and magnetic convection. The interesting point here is that the size of the structures in the studied regime seems to be relatively independent of the intensity of the convection.

As a better overview of the evolution of the wave number with the factor of criticality, we want to introduce a general picture of the wavelength's behaviour in comparison to the theoretical values at the onset of convection. With figure 4.25, we show cases for Ekman number $E = 1.15 \times 10^{-5}$ with $\Lambda = [0, 0.58, 1.12]$ and $E = 6.36 \times 10^{-6}$ with $\Lambda = [0, 0.43, 0.88]$. For the magnetic cases $\Lambda \neq 0$, we observe that the wavelength is consistent with the theoretical wavelength at onset. We also observe that the wave number doesn't really change as the Rayleigh number increases away from the onset. This would suggest that the flow's structure is relatively robust to the change in Rayleigh number. Concerning the viscous cases, we can underline again that the number of structures is higher, although because of the confinement of the cylinder it is no way near

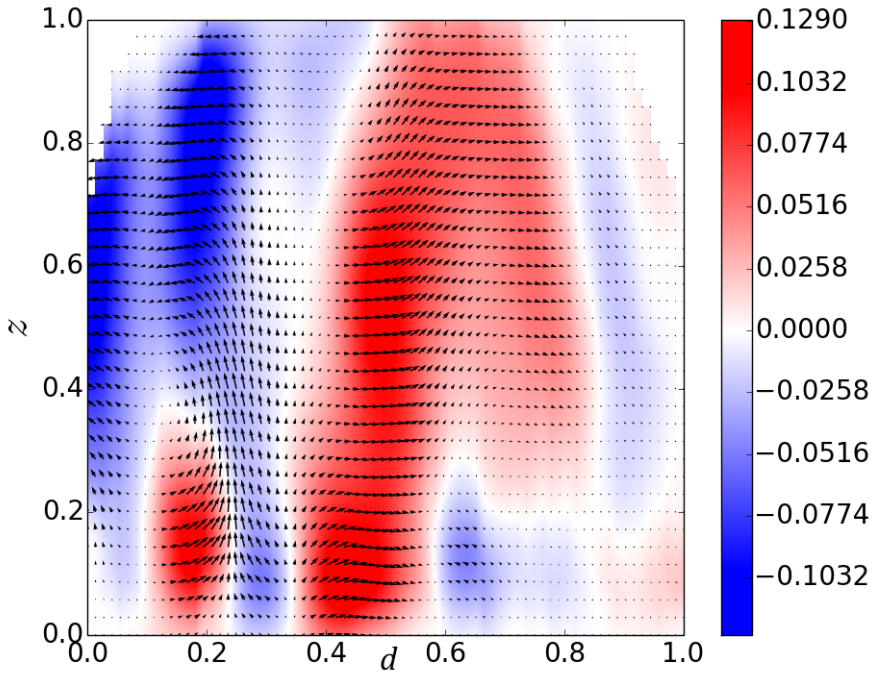

(a) $Ra = 4.37 \times Ra_c$

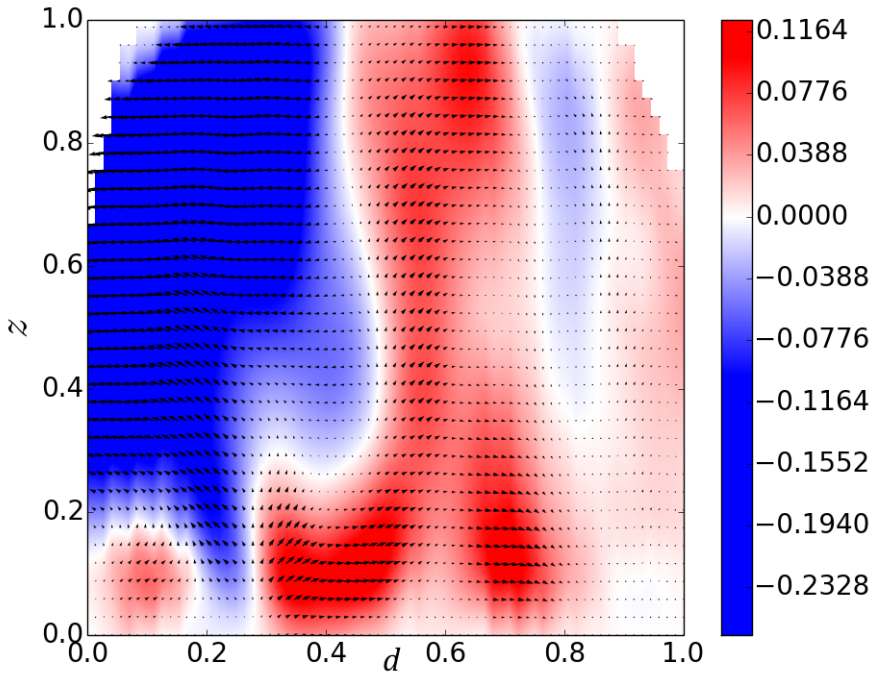

(b) $Ra = 8.08 \times Ra_c$

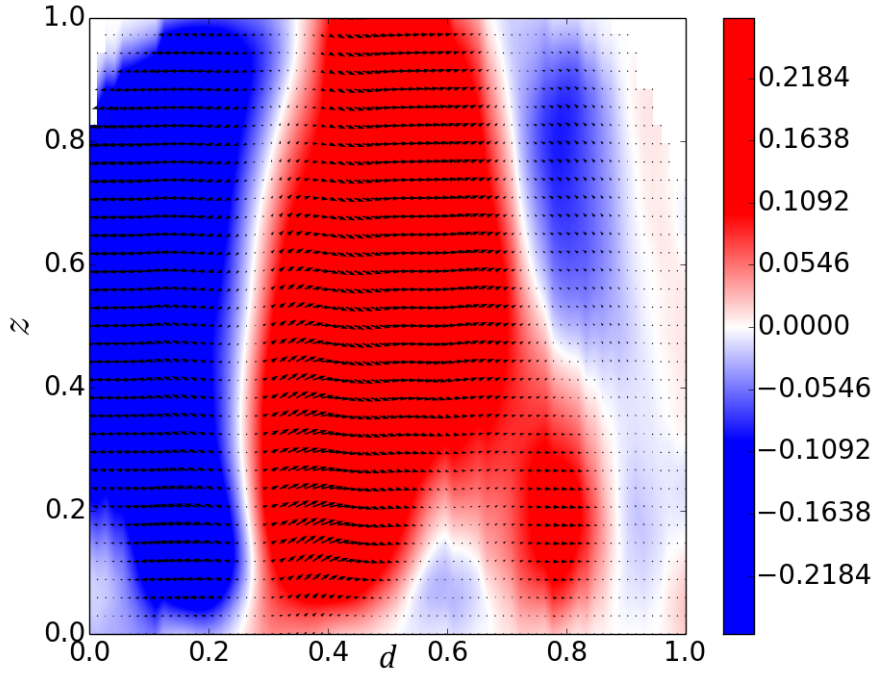

(c) $Ra = 14.28 \times Ra_c$

Figure 4.23: Average velocity fields (arrows) with u_r field in cm/s (colorbar) in the vertical plane for different Rayleigh numbers with $E = 1.15 \times 10^{-5}$ and $\Lambda = 0.58$. On the figures, d is normalized by the diameter of the heater and z is normalized by the height of liquid between the heater's surface and the dome. The cut at the top of the pictures and the pixel effect on the side are due to the discretization of the PIV software.

as high as the plane layer theory predicts.

4.3.2.2 Comparison to the secondary instabilities observed without magnetic field

In this section we are interested in the behaviour of the convection in a plane parallel to the equatorial plane and at a latitude of 68°. We focussed our attention on two different Ekman numbers ($E = 1.15 \times 10^{-5}$ and $E = 6.36 \times 10^{-6}$) with two Elsasser numbers, respectively $\Lambda =$ [0.33 and 015], and for several Rayleigh numbers. With respect to the previous results in the horizontal plane,

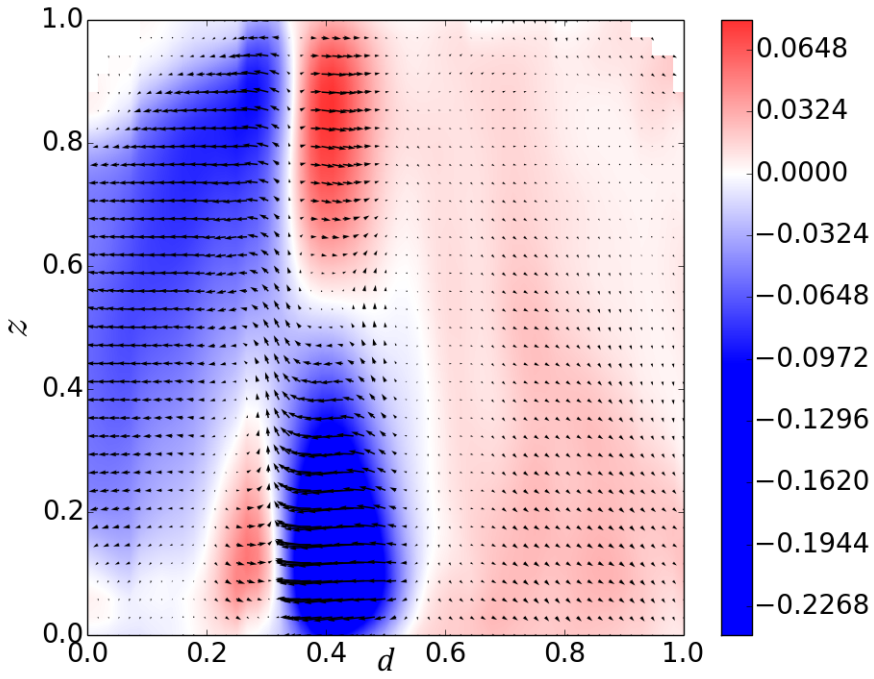

(a) $Ra = 1.6 \times Ra_c$

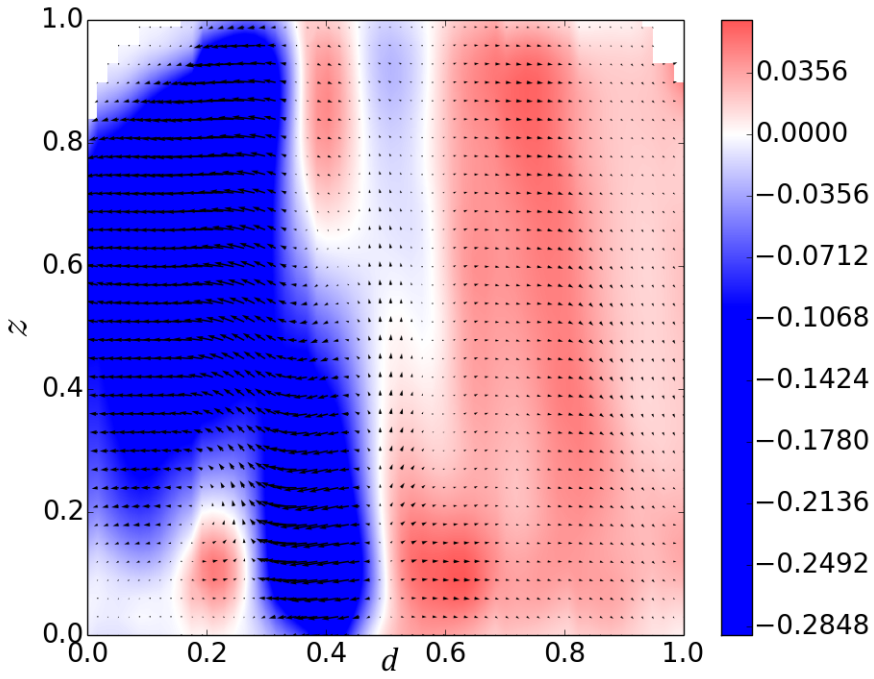

(b) $Ra = 2.73 \times Ra_c$

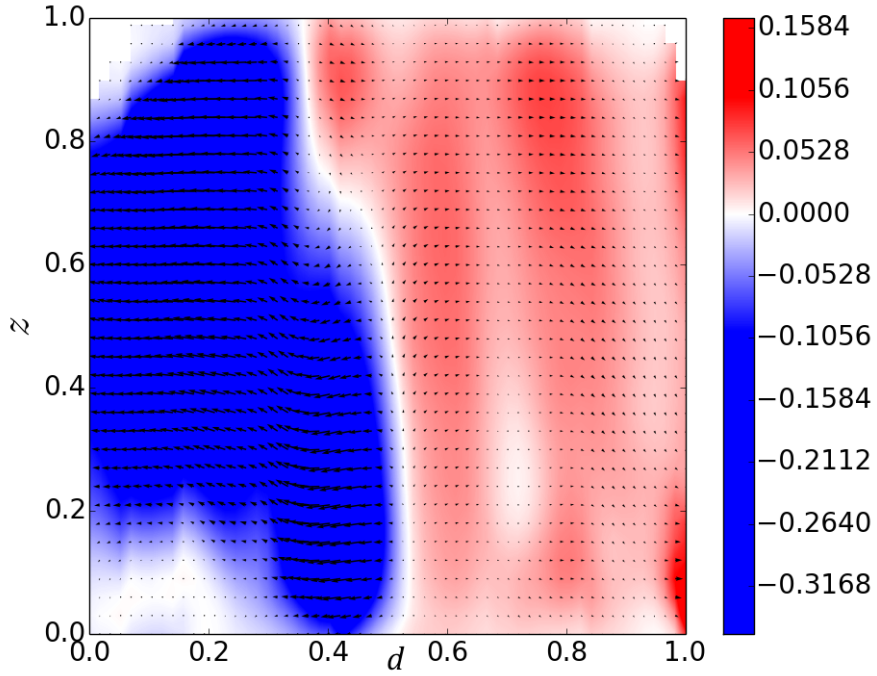

(c) $Ra = 7.39 \times Ra_c$

Figure 4.24: Average velocity fields (arrows) with u_r field in cm/s (colorbar) in the vertical plane for different Rayleigh numbers with $E = 6.36 \times 10^{-6}$ and $\Lambda = 0.88$. On the figures, d is normalized by the diameter of the heater and z is normalized by the height of liquid between the heater's surface and the dome. The cut at the top of the pictures and the pixel effect on the side are due to the discretization of the PIV software.

in all figures, the height and width are normalized by the diameter of heater placed underneath the measurement area.

Cases with $\Lambda = 0.33$ With Ekman number constant at 1.15×10^{-5}, we now investigate the effect of the magnetic field imposing an external field of 3.5T corresponding to an Elsasser number of $\Lambda = 0.33$. These points are of strong interests because as shown previously, they correspond to fully magnetic case ($\Lambda > 0.2$). In figure 4.26 we focussed on the approximate same range of criticality, $Ra \in [1.6 \times Ra_c, 13 \times Ra_c]$, as before. The results highlight a very different behaviour than the non-magnetic one. Instead of showing

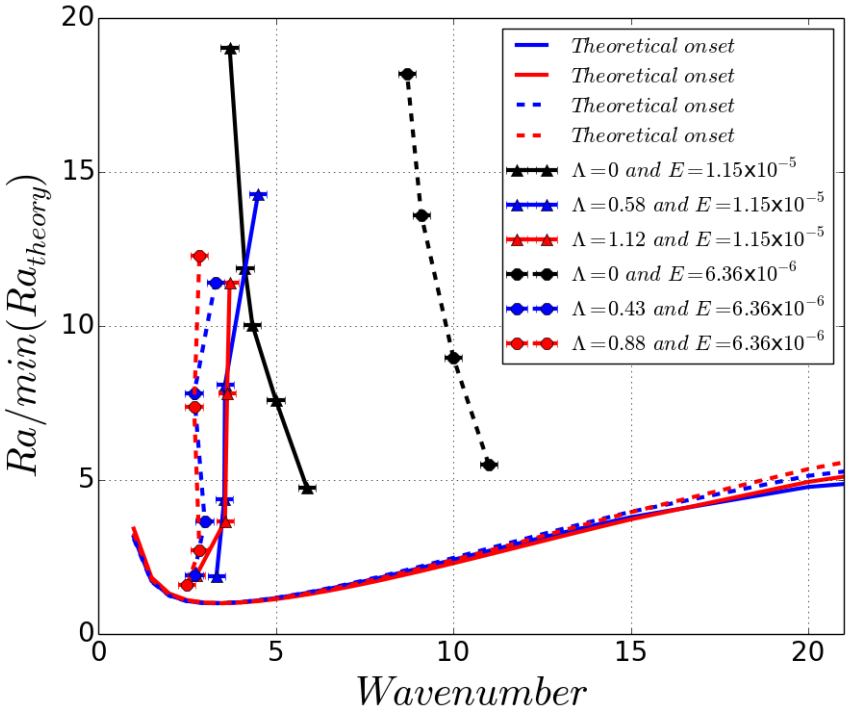

Figure 4.25: Plot of the measured wavenumber with respect to the ratio of the Rayleigh number to the critical Rayleigh number and comparison to the theoretical values at onset. The blue line corresponds to the theoretical onset obtained with linear theory for $\Lambda = 0.58$ and $E = 1.15 \times 10^{-5}$. The red line corresponds to the theoretical onset obtained with linear theory for $\Lambda = 1.12$ and $E = 1.15 \times 10^{-5}$. The dotted blue line corresponds to the theoretical onset obtained with linear theory for $\Lambda = 0.43$ and $E = 6.36 \times 10^{-6}$. The dotted red line corresponds to the theoretical onset obtained with linear theory for $\Lambda = 0.88$ and $E = 6.36 \times 10^{-6}$.

the flow growing from a multiple columns system, we can see it evolving as a single off-center anticyclonic column from weak degrees of criticality to strongly supercritical regimes. This unique vortex is known in the literature as the polar vortex. In contrast with the non-magnetic cases we are not observing the evolution of secondary instabilities. This supports the assumption that the Tangent Cylinder is very strongly influenced by the magnetic field.

Cases with $\Lambda = 0.15$ With Ekman number constant at 6.36×10^{-6}, we conducted measurements for an Elsasser number of $\Lambda = 0.15$. In figure 4.27, we

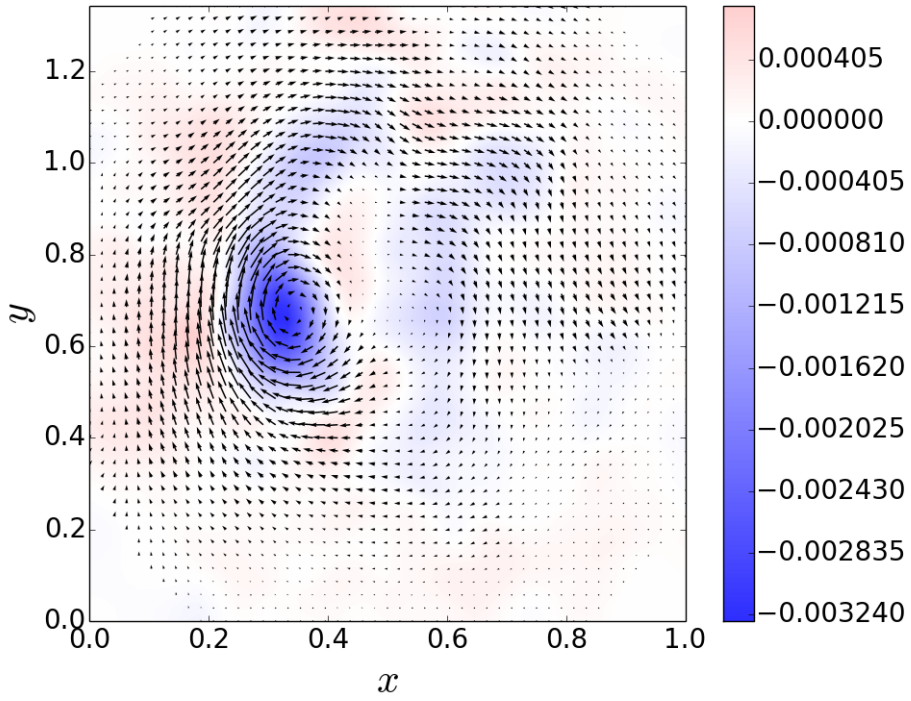

(a) $Ra = 1.67 \times Ra_c$

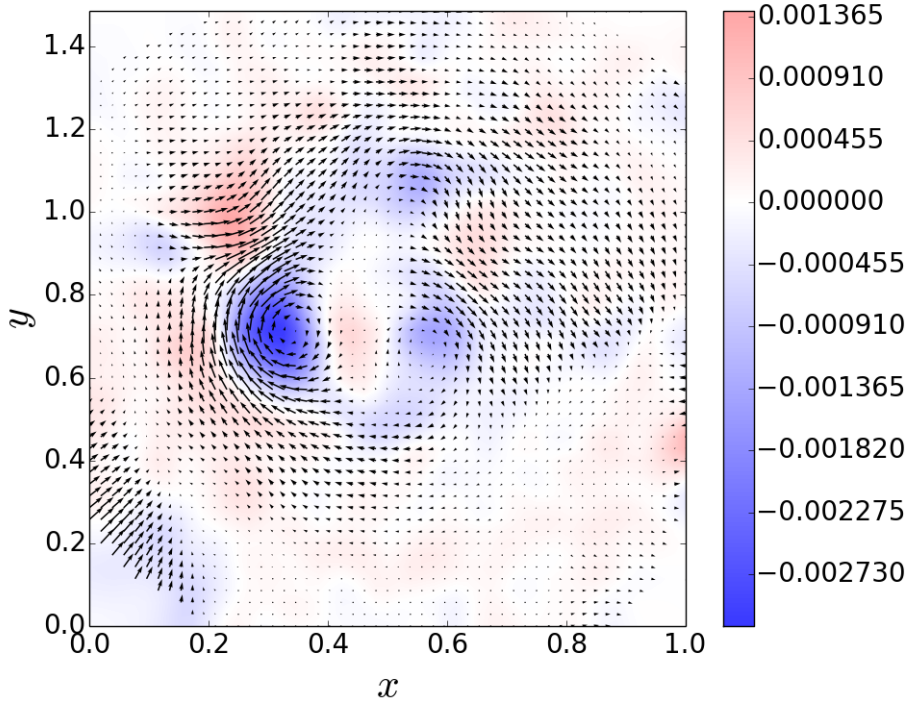

(b) $Ra = 1.77 \times Ra_c$

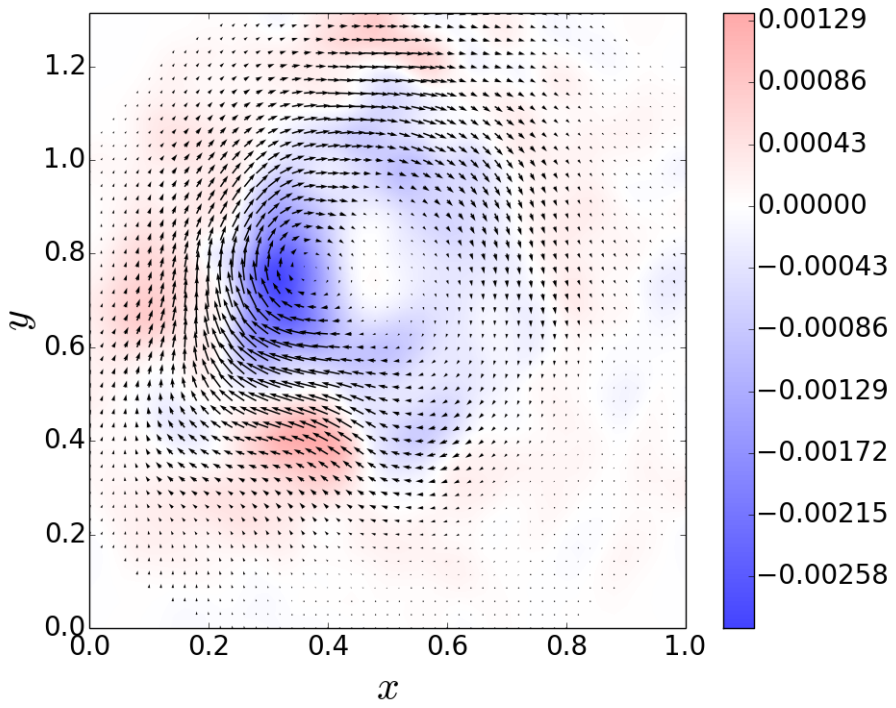

(c) $Ra = 2.16 \times Ra_c$

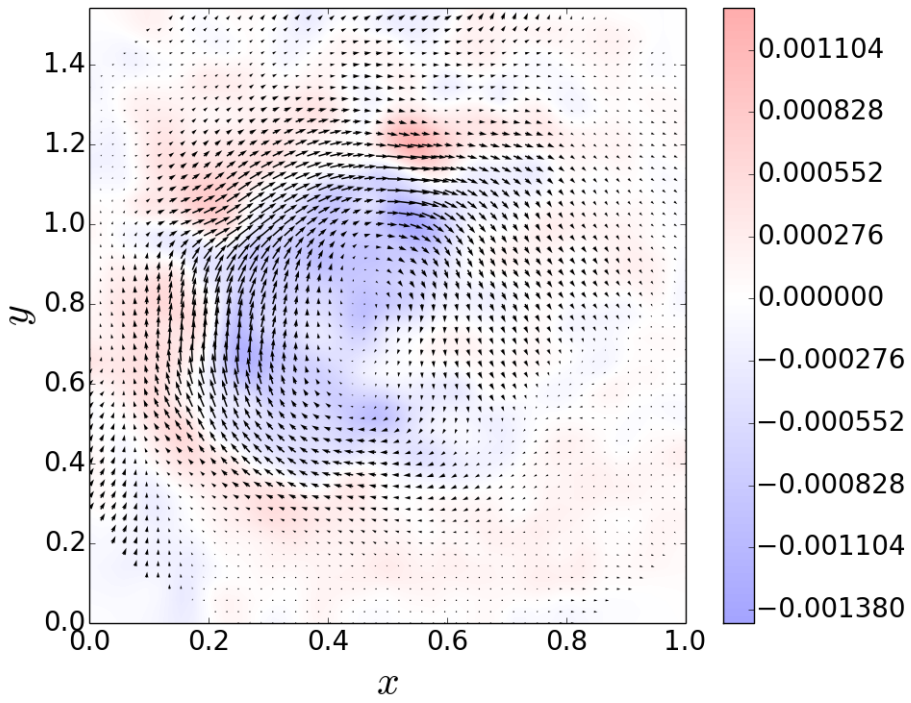

(d) $Ra = 2.38 \times Ra_c$

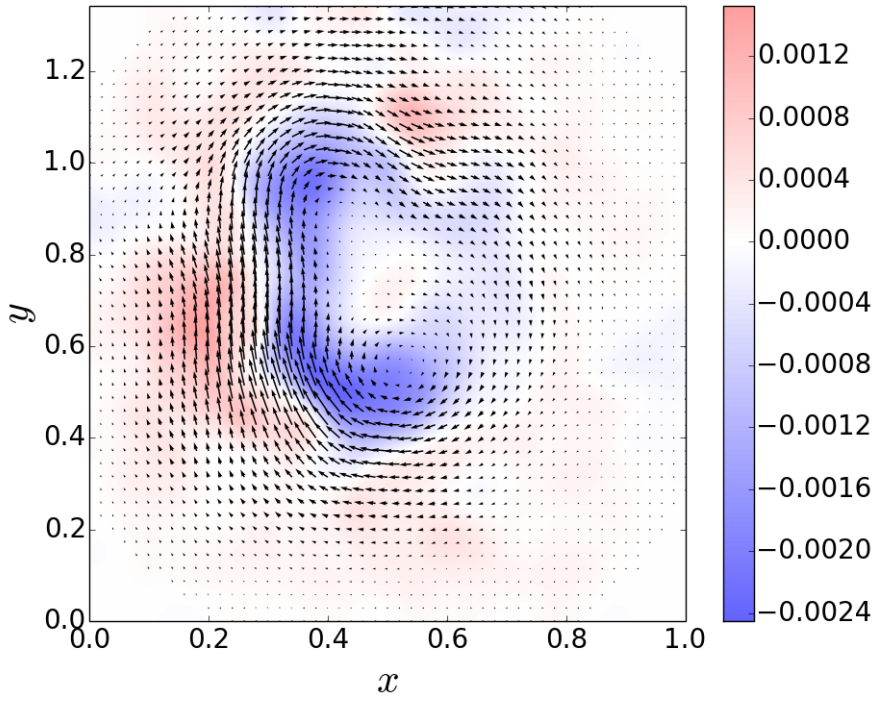

(e) $Ra = 4.26 \times Ra_c$

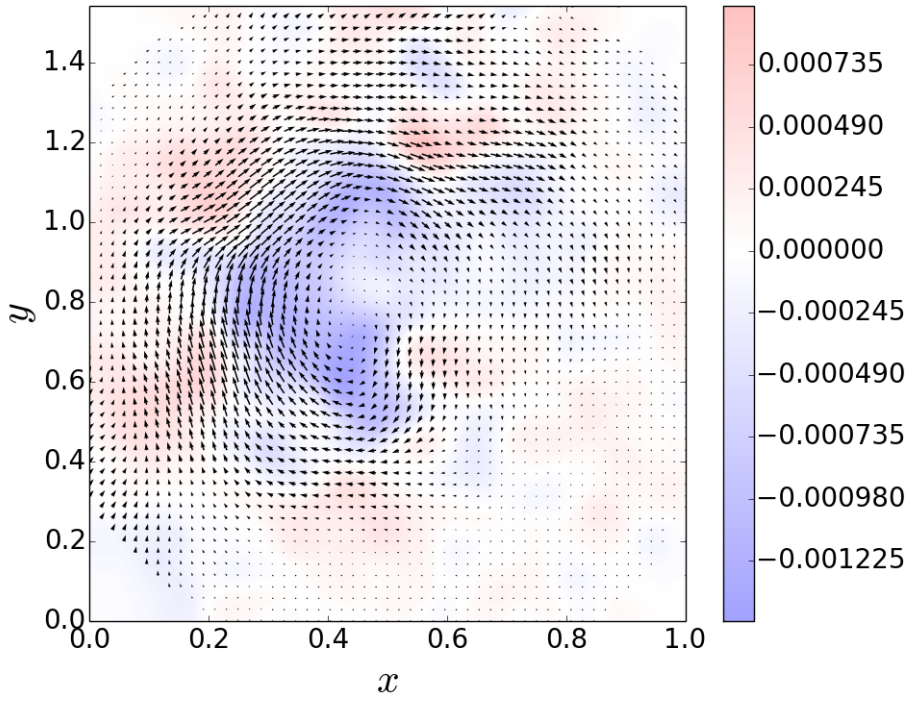

(f) $Ra = 4.39 \times Ra_c$

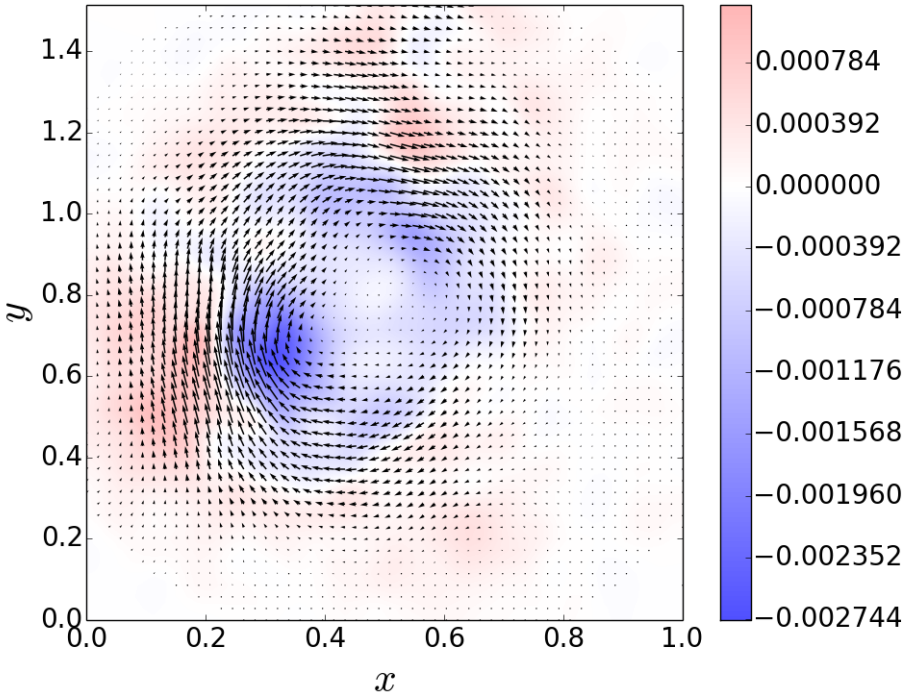

(g) $Ra = 7.98 \times Ra_c$

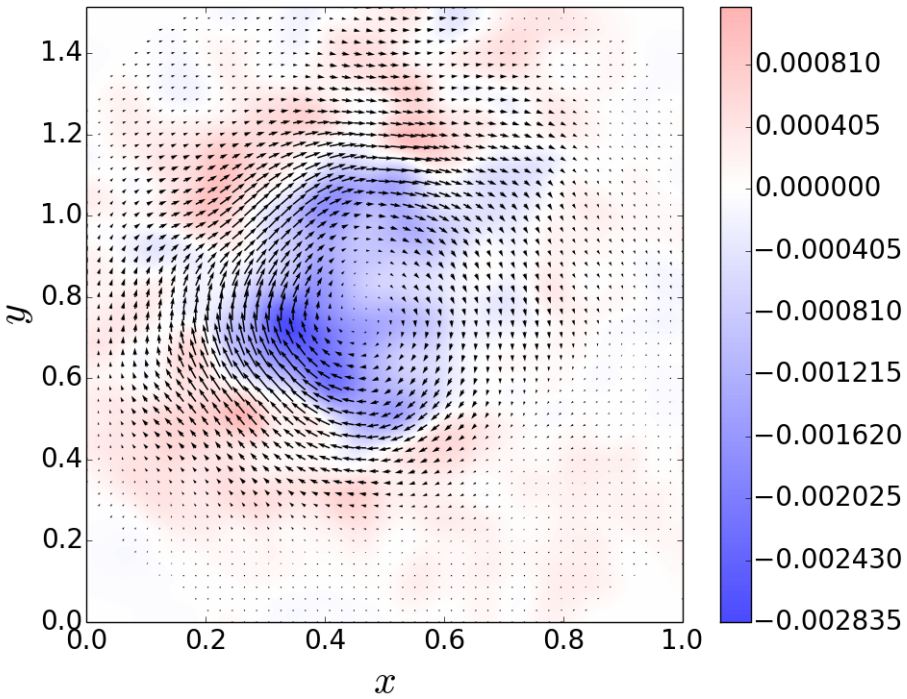

(h) $Ra = 8.09 \times Ra_c$

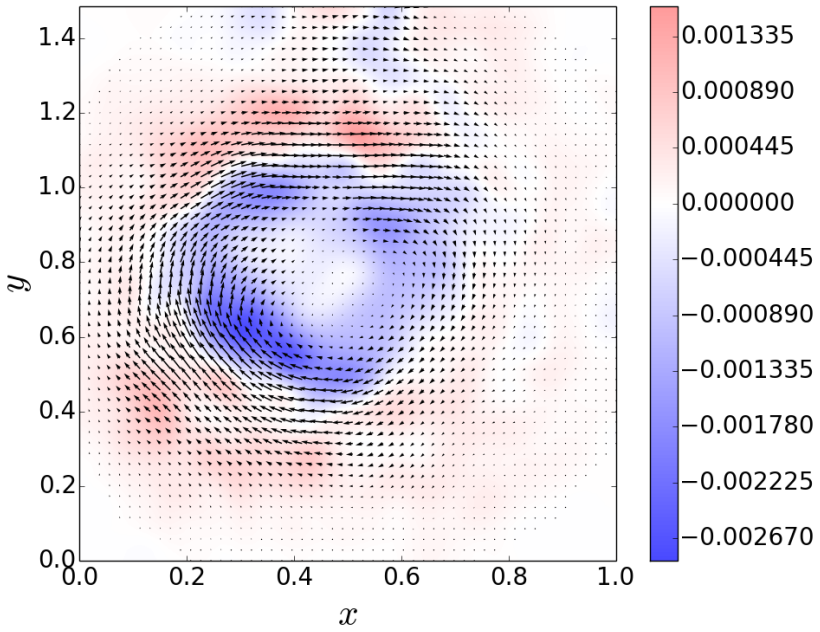

(i) $Ra = 12.58 \times Ra_c$

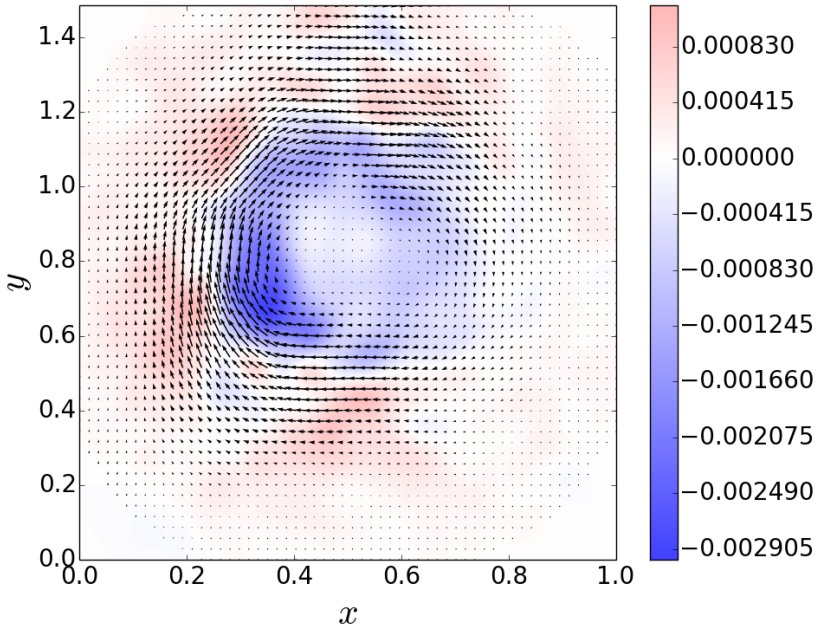

(j) $Ra = 12.67 \times Ra_c$

Figure 4.26: Average velocity fields (arrows) with vorticity field (colorbar) in the horizontal plane for different Rayleigh numbers with $E = 1.15 \times 10^{-5}$ and $\Lambda = 0.33$. On the figures, x and y are normalized by the diameter of the heater d. The center of the heater corresponds to the center of the pictures. Additionally, y is often larger than 1 because the area of interest in the PIV software was larger than the heater in that direction.

show how the flow evolves from a stage close to onset to a clearly supercritical regime with Rayleigh number such as: $Ra = [1.91 \times Ra_c, 11.85 \times Ra_c]$. The present cases need to be presented as they correspond to a mixed case rather than a purely magnetic case. Our results here show that around the onset the flow behaves quite similarly to the former non-magnetic case going from small structures to a spiraling pattern. This evolution is in agreement with [64] as the flow evolves from the onset, some central helical plumes, some central helical plumes mixed with parietal modes to finally a central vortex on axis. Nevertheless, we observe a significant difference with the previous non-magnetic results. Indeed earlier, we report that the Taylor-Proudman constraint was eventually broken by the convection, whereas in these present cases the Taylor-Proudman constraint does not appear broken for supercritical Rayleigh numbers. This is interesting, as the magnetic mode and the viscous mode at onset are comparable in these cases. In fact, this suggests that even if the role of the Lorentz force is not significant at onset it plays a crucial role in supercritical regimes. Our explanation is that the MHD characteristic surfaces are parallel to the isobar in the Tangent Cylinder. Hence the Taylor-Proudman constraint becomes much stronger.

4.4 Global Quantities

In this section, we describe global quantities in our results such as the energy and the fluctuation of the velocity. The energy presents the different type of flow structures occurring beyond the onset of convection. The fluctuations aim to evaluate the turbulence in our results.

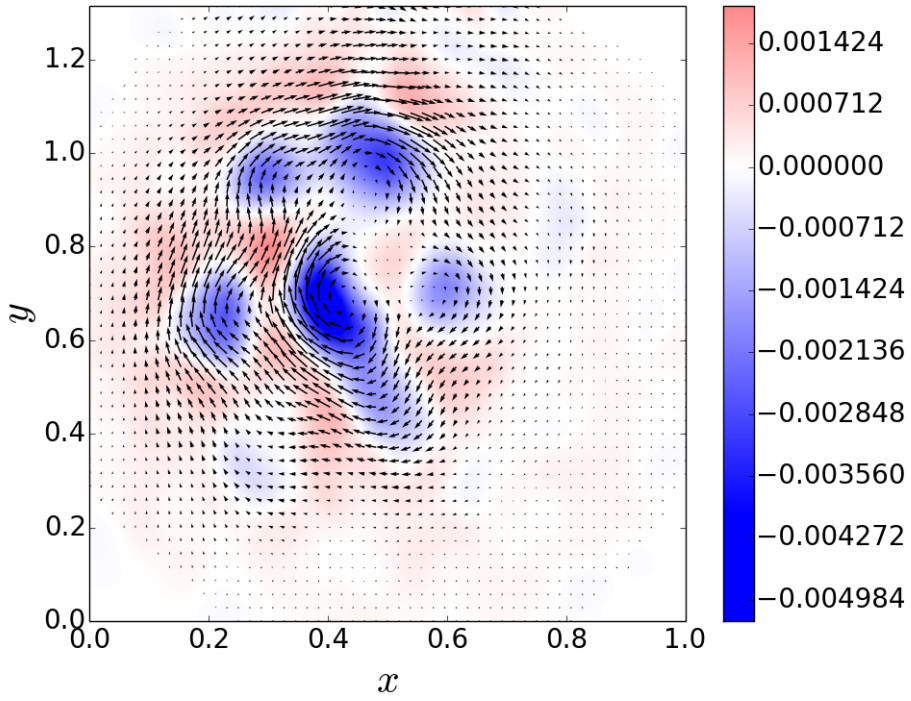

(a) $Ra = 1.91 \times Ra_c$

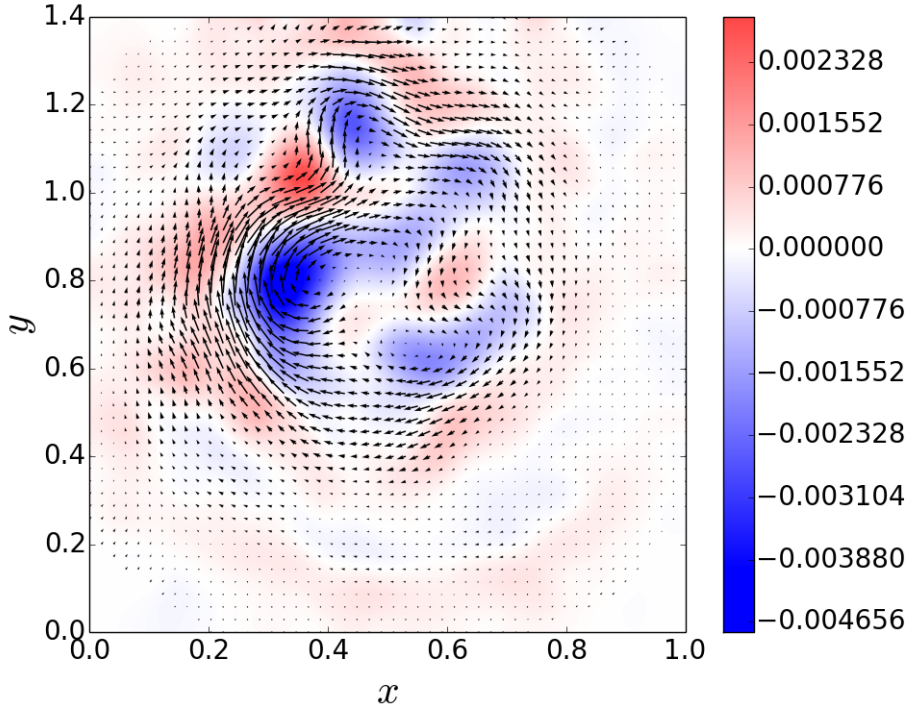

(b) $Ra = 2.23 \times Ra_c$

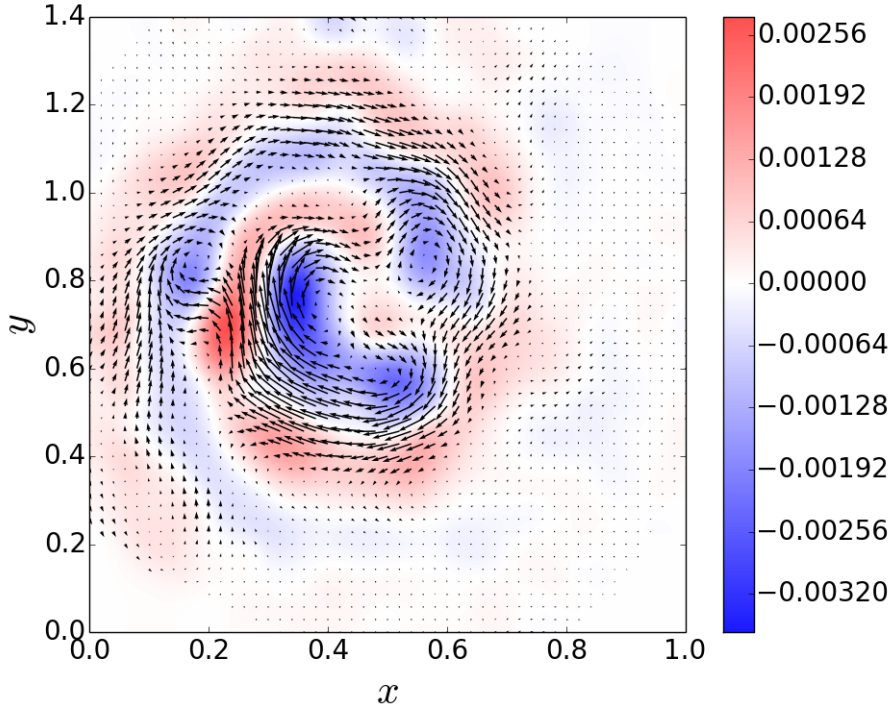

(c) $Ra = 3.19 \times Ra_c$

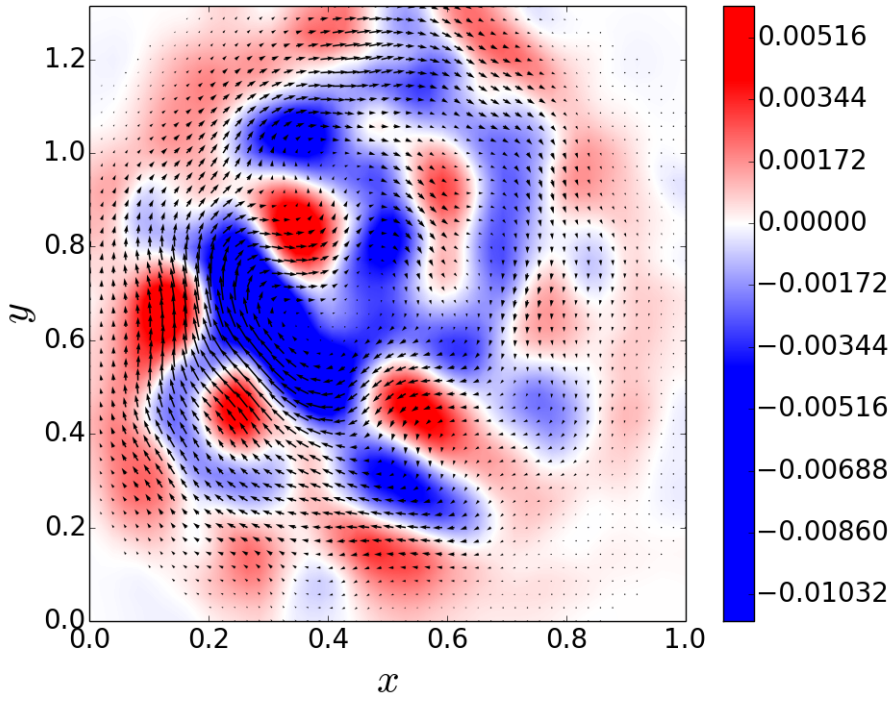

(d) $Ra = 4.70 \times Ra_c$

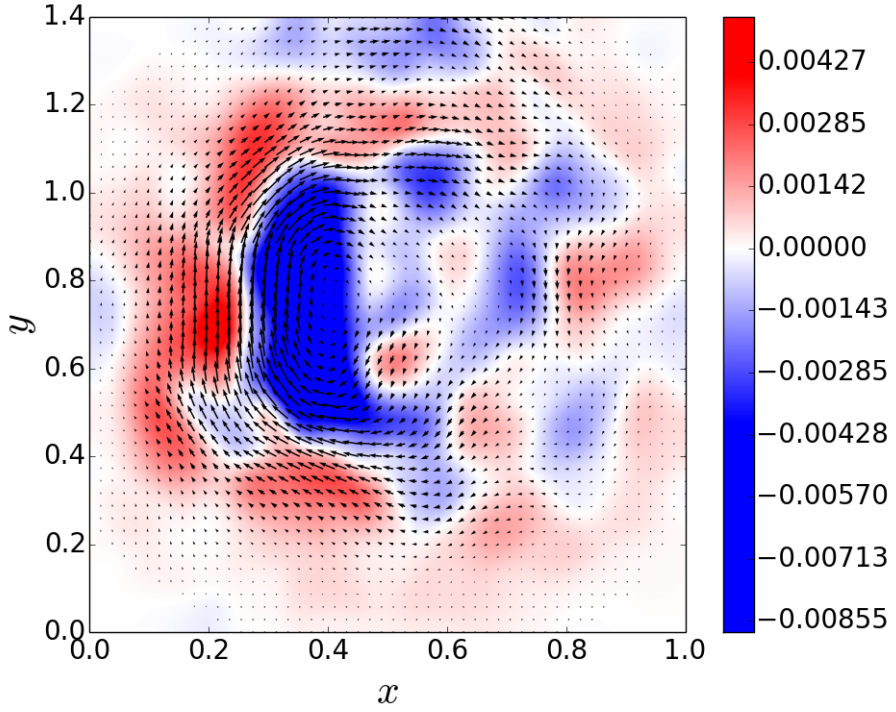

(e) $Ra = 4.91 \times Ra_c$

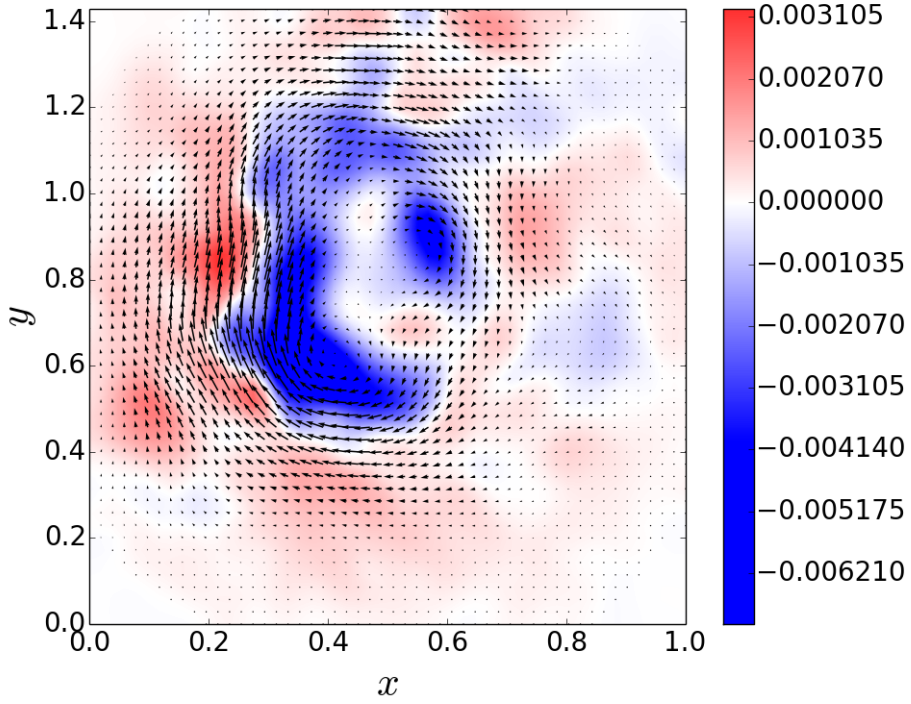

(f) $Ra = 7.65 \times Ra_c$

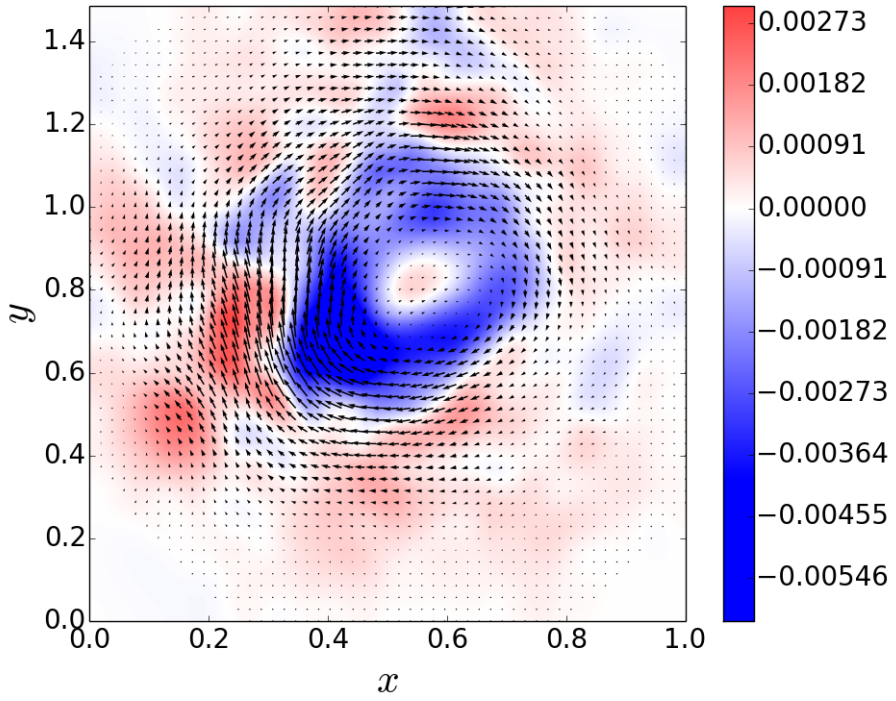

(g) $Ra = 7.91 \times Ra_c$

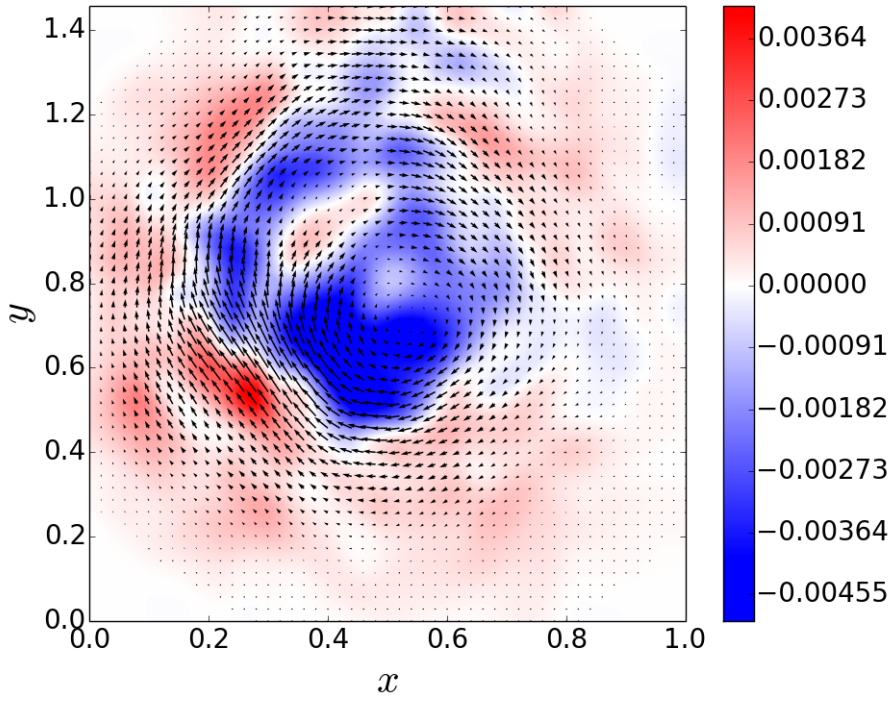

(h) $Ra = 11.32 \times Ra_c$

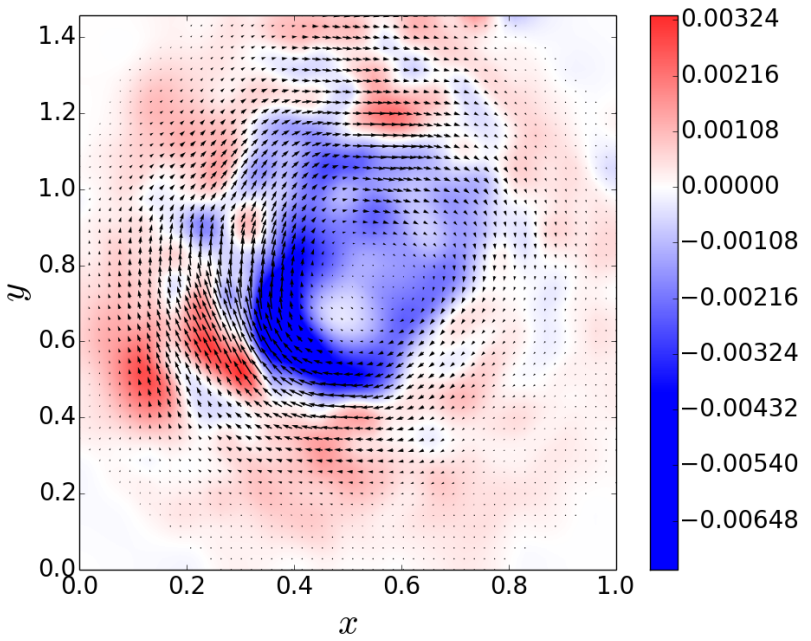

(i) $Ra = 11.63 \times Ra_c$

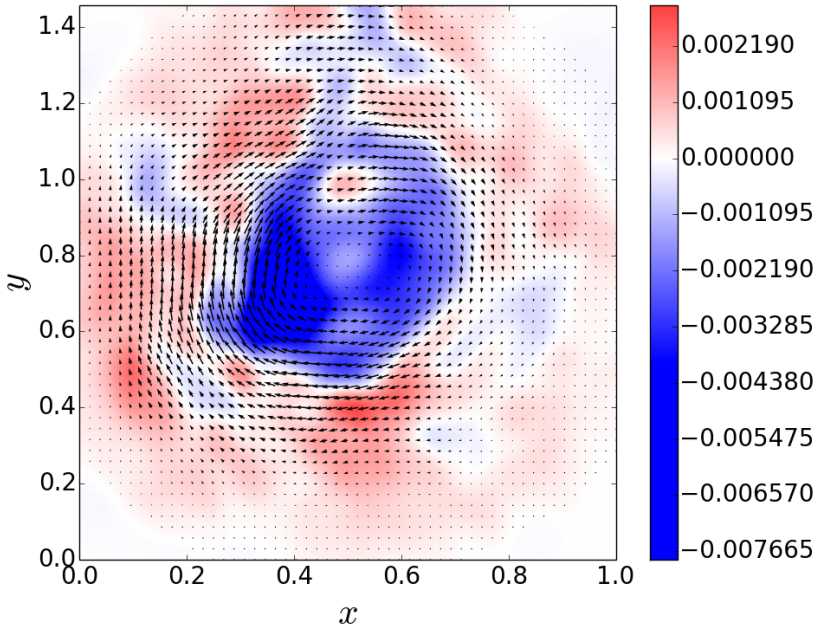

(j) $Ra = 11.85 \times Ra_c$

Figure 4.27: Average velocity fields (arrows) with vorticity field (colorbar) in the horizontal plane for different Rayleigh numbers with $E = 6.36 \times 10^{-6}$ and $\Lambda = 0.15$. On the figures, x and y are normalized by the diameter of the heater d. The center of the heater corresponds to the center of the pictures. Additionally, y is often larger than 1 because the area of interest in the PIV software was larger than the heater in that direction.

4.4.1 Energy

In order to summarize the previous results, we calculated at the total energy in the horizontal plane on the time average of the flow. It is a partial image of the energy as we investigated only one horizontal plane and we have only access to the r and θ-component of velocity. On figure 4.28, we highlight different regimes mainly corresponding to the viscous case ($\Lambda = 0$). Indeed in the previous results we observe four different stages in the flow corresponding to [8] and [64]. Although the distinction between the different modes of the flow is not particularly clear in [8] because of the measurement technique they used, the authors in [64] showed several consecutive modes. The modes in our case evolve with respect to the Rayleigh number with: the onset of convection, some central helical plumes, some central helical plumes mixed with parietal modes to finally one central vortex. Interestingly, we observe that these four stages don't correspond to the dynamics of the flow with magnetic field. Indeed instead of evolving from small structures at onset to a system of plumes to one large central vortex, the magnetic case shows very few large structures at onset that exists for all Rayleigh number (in our regime) and drives the flow.

4.4.2 Velocity fluctuations

Finally we looked at the fluctuation of velocity in order to determine if the cases we are investigating are turbulent. On figure 4.29, we show the ratio of the fluctuation's energy over the mean flow energy. It highlights that the energy of the fluctuations is much smaller than the average energy in our results. Nevertheless although it would be wrong to establish that at high Rayleigh number we observe turbulence, we can safely remark that the system in all case goes toward a large increase of the energy of the fluctuations. In

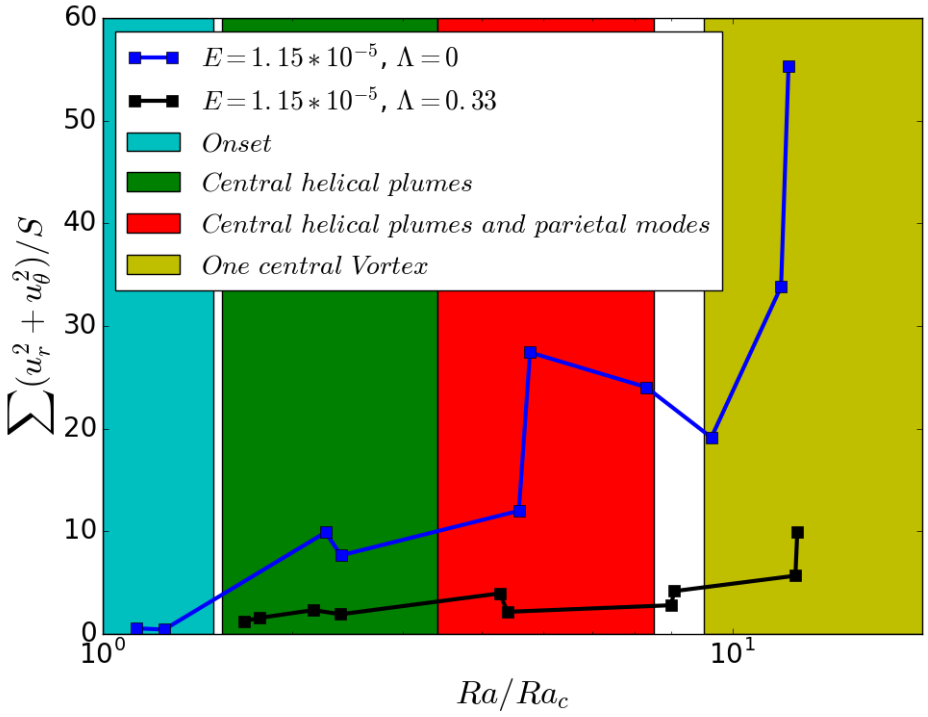

Figure 4.28: Energy in the horizontal plane with respect to the ratio of the Rayleigh number over the critical Rayleigh number. We are not adding the value of u_z^2 as we do not measure simultaneously the three component of velocity with our laser plane.

the non-magnetic cases, we note that for Ekman number, $E = 1.15 \times 10^{-5}$, the fluctuations start increasing for a Rayleigh number of approximately 4×10^8. When the Ekman number is lowered to $E = 6.36 \times 10^{-6}$ the fluctuations start increasing for a larger value of the Rayleigh number (approximatively 7×10^8). This was expected as the system is more supercritical for high Ekman number with respect to comparable Rayleigh number. In the magnetic cases, the same behaviour is observed. Additionally by comparing the cases for one value of the Ekman number but with and without magnetic field, we remark that the magnetic field generally lowers the fluctuations and delays their increase with respect to the Rayleigh number.

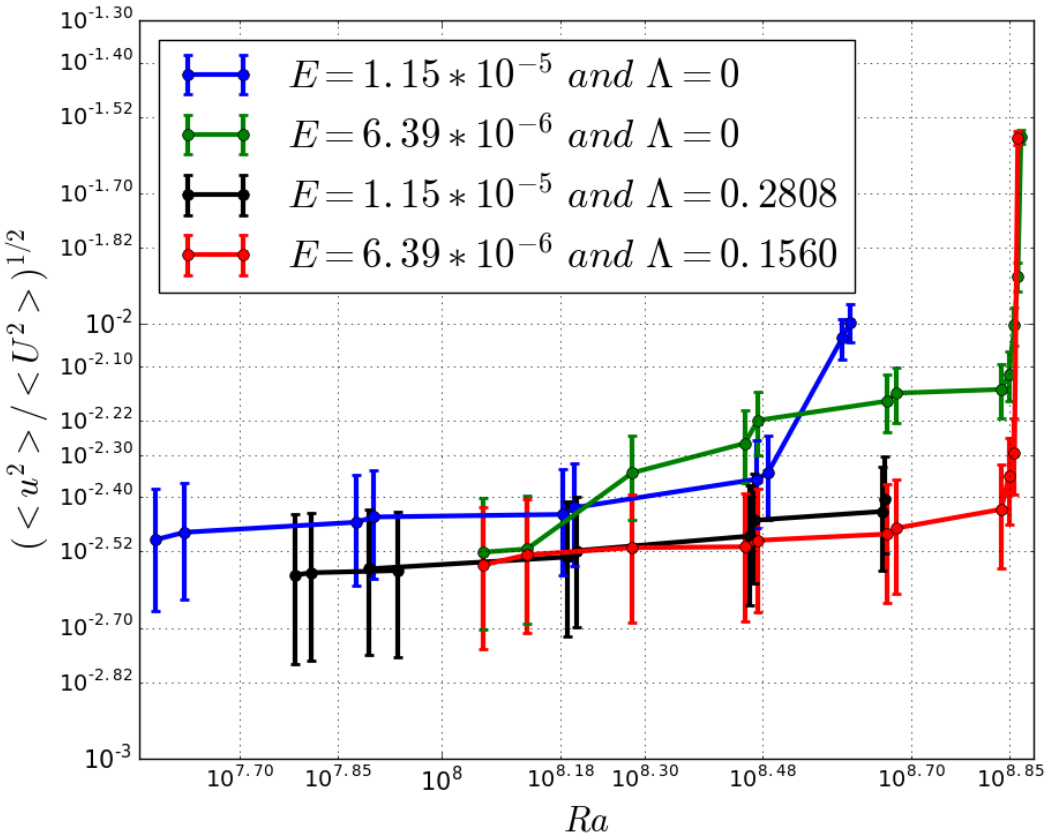

Figure 4.29: Ratio of the relative energy fluctuation over the average energy with respect to the Rayleigh number of the system. u is the fluctuation velocities averaged in space and time. U is the mean velocity of the averaged velocities in space and time.

4.5 Conclusion

In this chapter, we compared our experiment to established results in previous non-magnetic experiments or simulations. We obtained several results:

- for non-magnetic cases, we show that the convection is strongly constrained by the Taylor-Proudman constraint and has more similarity with the convection in cylindrical geometry rather than plane layer geometry.

- we confirmed the scalings of the Rayleigh number and the wave number at the onset of purely rotating convection. Although we observed sig-

nificant differences to the infinite plane layer theory, we recovered the results of [64]. This confirms the important role of the confinement on a geometry such as the Tangent Cylinder.

- in the magnetic cases, we confirmed with quantitative data the results found by [43] on the drastic decrease of structure numbers above a certain magnetic field.

- we showed the transition between viscous to magnetic regimes at around $\Lambda = 0.2$ at the onset of convection.

- we investigated the flow in the horizontal plane highlighting different behaviours whereas the case is magnetic or non-magnetic. We showed that in the magnetic cases a single vortex prevails between onset and ten time supercritical regimes. Without magnetic field, we obtained regimes with several vortices regrouping into a large central vortex.

- finally, we conclude this chapter with the study of the energy and the fluctuation of velocity. The energy showed a large discrepancy between magnetic and non-magnetic cases. Indeed even for a heavily convective system, the magnetic case seems to correspond to the structure at onset. On the other hand, without magnetic field, we observed several distinct modes of convection following the onset. The velocity fluctuations were not sufficient to conclude on the development of the convection but they were enough to say that our cases were steady or very weakly turbulent.

Chapter 5

Geophysical implications of the magnetoconvection in a Tangent Cylinder

5.1 Introduction

In this chapter, we present our results from the geophysical point of view. We are interested in three typical results for the Tangent Cylinder: the heat flux behaviour, the zonal flow and the polar vortex. Firstly, we will introduce the results for heat flux. The heat flux is essential to clarify the general behaviour of the convection in the core and to investigate the global heat flux through the Tangent Cylinder. Then we will introduce our findings concerning the effect of the magnetic field on the zonal flow which we believe is linked to the presence of a polar vortex. The zonal flow plays a significant role in the geodynamo mechanism and its shape has multiple consequences for the dynamics of the Earth core ([32] and [37]). Finally, before we conclude the present chapter, we will present that the polar vortex is a direct consequence of how the convection is affected by the magnetic field. In particular, we will attempt to compare our results to those of [36] and [56] established for spherical shells.

5.2 Heat flux

In order to investigate the heat flux within in the Tangent Cylinder we looked at the behaviour of the Nusselt number. This gives us an estimation of the intensity of the convection with respect to a conductive system. Indeed the Nusselt number is commonly defined as:

$$Nu = \frac{QD}{k\Delta T}, \tag{5.1}$$

with Q the heat flux through a thickness D of fluid with a thermal conductivity k and under a difference of temperature ΔT. To measure the heat flux in our experiment we measured the temperature loss in the coolant between the inlet and the outlet of the heater at the center of our dome. Figure 5.1 shows the different results we obtained for the scalings of Nusselt number with respect to Rayleigh numbers. These results were obtained for three different rotation rates and several intensities of the magnetic field.

In our results we observe two different trends. These trends appear for high values of the Rayleigh number, therefore away from the onset of convection. Without the magnetic field, we confirm a well known scaling of $Nu \sim Ra^{2/5}$. This scaling is consistent with the power law recovered experimentally by Sumita & Olson [58]. With the magnetic field, we measured a different tendency: $Nu \sim Ra^{2/3}$. This result is interesting. In the magnetic case the Rayleigh number at onset is a lot smaller; therefore the factor of critically of this curve is supposed to be higher. Theoretically the system should tend to scaling closer to the non-rotating scaling as the role of the rotation gets relatively weaker. Hence we could expect to recover a scaling such as $Nu \sim Ra^{2/5}$ instead of $Nu \sim Ra^{2/3}$. Nevertheless we must also consider the eventuality that this scaling of $Nu \sim Ra^{2/3}$ may be the transition between the scalings described

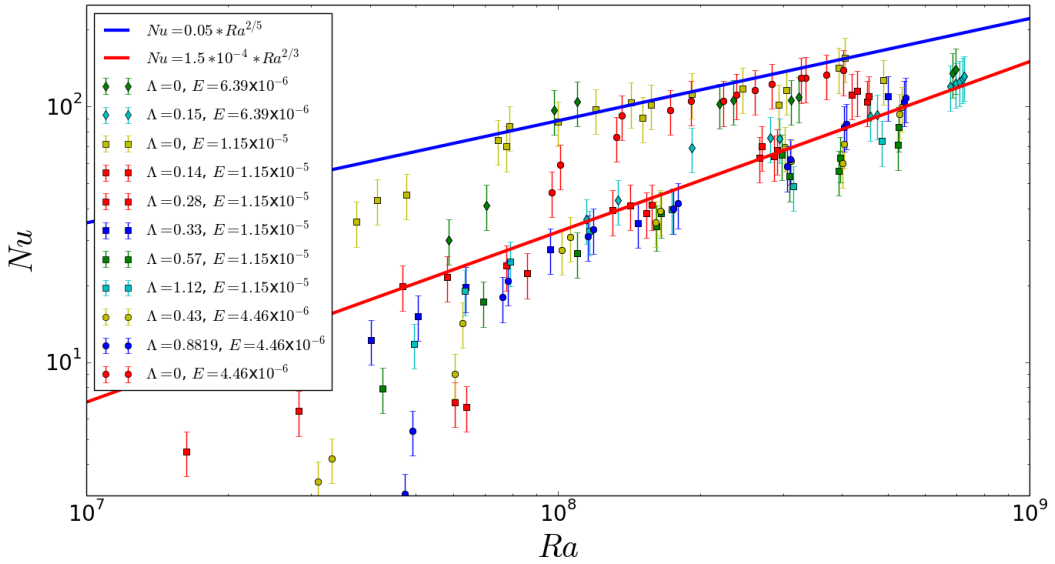

Figure 5.1: Scaling $Nu(Ra)$ for supercritical regime. The red continuous line is the trend with the magnetic field and the blue continuous line is the trend without magnetic field.

by Aurnou [7]. Indeed in this study the author shows a transition between $Nu \sim Ra^{1.14}$ to $Nu \sim Ra^{0.4}$.

Additionally, we connect our results to the typical results obtained in the literature by Aubert and Christensen on dynamo process [5], [22] and [6]. Therefore instead of using the classical Nusselt number we use Nu^*. It is defined as:

$$Nu^* = Nu \times E \times Pr^{-1}. \tag{5.2}$$

Likewise, we use a modified Rayleigh number based on the heat flux instead of the classical one. It can be written as:

$$Ra_Q^* = Ra^* Nu^*, \tag{5.3}$$

where Ra^* corresponds to:

$$Ra^* = Ra \times E^2 \times Pr^{-1}. \tag{5.4}$$

Nu^* and Ra^* correspond to diffusionless forms of the Nusselt number and the Rayleigh number respectively. Ra_Q^* is therefore a diffusionless Rayleigh number based on the heat flux. Using this formalism, in figure 5.2, although we were not able to recover the dependency with the Prandtl number (we used only Sulphuric acid here), we obtained results consistent with scaling laws such as $Nu^* \sim Ra_Q^{*0.29}$. This scaling was first obtained for non-magnetic rotating convection experimentally by [58] in a hemispherical shell. Our results confirm this finding experimentally and show the independence of this scaling to the magnetic field. With figure 5.2, we also observe an inflection of our data for Ra_Q^* larger than one. This interestingly corresponds to the limit defined in [7] between rapidly rotating regimes and buoyancy dominated regimes. Unfortunately, this inflection is not enough to extract an asymptotic scaling as presented in [7]. Nevertheless, our scaling suggests that the convection in the Tangent Cylinder and outside it essentially obey the same phenomenology.

5.3 Zonal flow: sign and intensity

In this second section, we discuss the question of the zonal flow. This corresponds to the analysis of the results obtained in the horizontal plane as presented in the previous chapter. The zonal flow has been thoroughly studied throughout numerical simulations and experiments such as [6], [21], [22], [56] and [10]. Indeed this type of flow is particularly common in planetary systems, for example geomagnetic observations of the Earth suggest its existence in the outer core region [46] or [31]. In the Earth's core, the zonal flow arises from

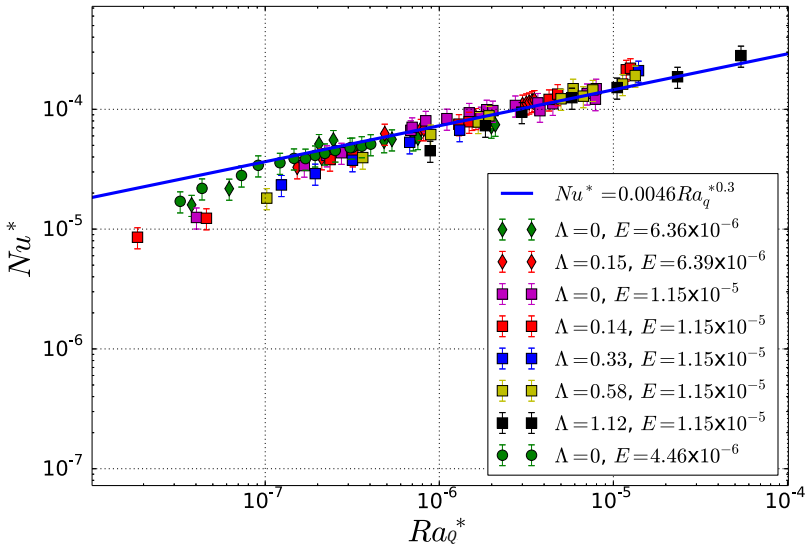

Figure 5.2: Scaling $Nu^*(Ra_Q^*)$ following [58].

the magnetogeostrophic balance which can be written as follows:

$$\mathbf{e}_z \times \mathbf{v} = -\nabla P + \Lambda(\nabla \times \mathbf{B}) \times \mathbf{B} + RaT\mathbf{r} \tag{5.5}$$

By taking the z-component of the curl of the magnetogeostrophic balance, we obtain the following expression for the azimuthal wind:

$$\frac{\partial u_\phi}{\partial z} = -\Lambda B \frac{\partial J_\phi}{\partial z} + Ra \frac{1}{r} \frac{\partial T}{\partial \theta}. \tag{5.6}$$

The azimuthal wind corresponds to the left hand side term. We note that the effect of the Lorentz force on the azimuthal wind is through the action of the azimuthal current (second term in the previous expression). This expression corresponds to the spherical coordinates expression. Nevertheless, in the following, we will discuss the θ-component of the velocity in cylindrical coordinates. Indeed our measurements limit us to this system of coordinates.

Before presenting our results it is necessary to emphazise once again how we obtained them. First the measurements of the θ-component of velocity were obtained in the horizontal plane as described in Chapter [3]. Therefore they correspond to the θ-component in cylindrical coordinates. Second our measurements are restricted to one plane at the latitude 68°. As a consequence it is impossible to deduce a clear picture of the shape of the zonal flow in the Tangent Cylinder with a X shape or as a prograde motion as described in [9]. Indeed along the vertical axis, the thermal wind is expected to change its rotation from anti-clockwise at the bottom of the cylinder to clockwise at the top.

5.3.1 Thermal Wind without magnetic field

Here, we present the results obtained in a non-magnetic situation. On figures 5.3a and 5.3b we plot, along the radius, the average of the θ-component of the velocity along the θ-direction. These results correspond to a factor of criticality between 1 and 10. The obvious result here is the general increase of the intensity of the velocity with the Ekman number. This is in agreement with the scaling described in [6] which give $u_\theta \sim E^{9/10}$. Unfortunately, we don't have enough cases to corroborate this result as we have only two different values of the Ekman number. Interestingly, we observe different other points in our results:

1. For factors of criticality smaller than 9, we observe an eastward flow on the outside of the Tangent Cylinder (large values of the radius)

2. In the case of $E = 1.15 \times 10^{-5}$, we found the onset through the fast mode identified by [33]. It is confirmed by the dark blue curve on figure

5.3a showing a large westward structure at the center surrounded by an eastward flow.

3. In the case of $E = 6.36 \times 10^{-6}$, we found a slow mode at onset. It is confirmed by the dark blue curve on figure 5.3b showing an eastward flow at the very center of the cylinder surrounded by a westward flow again surrounded by an eastward flow. This reveals small centered structures typical of the fast modes described in [33].

4. When the Rayleigh number increases, we note that our results take the form a sinusoidal functions (green curve and red curve respectively on figures 5.3a and 5.3b). This behaviour corresponds to what we described as central helical plumes in the previous chapter. In these cases, the liquid is pumped at the bottom from the center of the heater throughout the height of the Tangent Cylinder and them pushed out toward the edge of the cylinder.

5. When the Rayleigh number increases again, we remark that the zonal flow takes over the flow by wiping out the convective structures and pushing the surrounding eastward flow outside the Tangent Cylinder.

5.3.2 Thermal Wind with magnetic field

Here we present results obtained with the magnetic field. Our measurements correspond to two different Ekman numbers $E = 1.15 \times 10^{-5}$ and $E = 6.36 \times 10^{-6}$ at two different Elsasser number, respectively $\Lambda = 0.33$ and $\Lambda = 0.15$. On figures 5.4a and 5.4b, we plot again the average of the θ-coordinate of the velocity as a function of the radius. Our first obvious remark is that the flow is always oriented in the westward direction. Therefore there are no

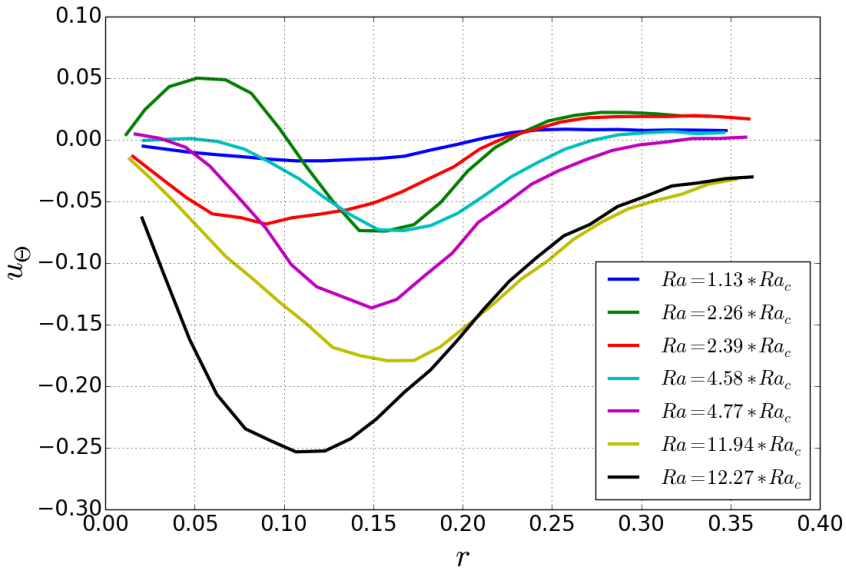

(a) $\Lambda = 0$ and $E = 1.15 \times 10^{-5}$

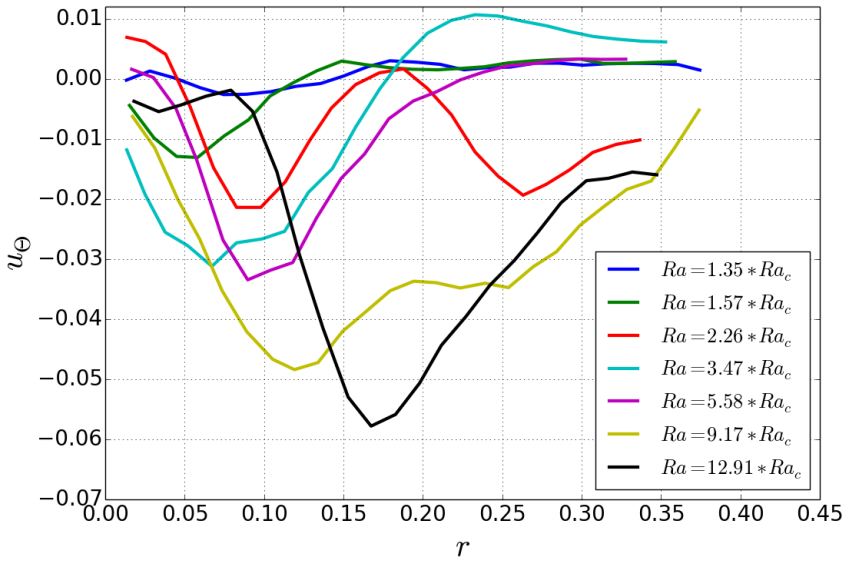

(b) $\Lambda = 0$ and $E = 6.36 \times 10^{-6}$

Figure 5.3: Average along θ of the time average θ-component of the velocity in dm/s as a function of r normalized by the diameter of the heater

trace of central helical plume as in the non-magnetic cases. This confirms the results already obtained in the previous section supporting the existence of a Polar vortex. The second interesting point is the lower velocity obtained with the magnetic field with $\Lambda = 0.33$. This could suggest at first sight that the magnetic field acts as a brake on the flow by resisting the westward motion. But to our interpretation, what we observe is the Taylor-Proudman constraint becoming more rigid as the characteristic surfaces of the magnetic field are parallel to the isobar in our Tangent Cylinder [2] and [40]. The final point on these results is the position of the maximum of velocity. In the case at $\Lambda = 0.15$ we don't observe a significant difference with the non-magnetic results. This is probably because these parameters correspond to a hybrid case between magnetic and viscous behaviour as we showed in the previous Chapter, where the magnetic mode is not clearly distinct from the viscous mode at onset. Nevertheless in the case where $\Lambda = 0.33$, the maximum of the velocity tends to be pushed towards the outside of the Tangent Cylinder. Indeed instead of observing a radius of 0.1 for the maximum (figure 5.3a), we observe a maximum at a radius of 0.17 (figure 5.4a). On figures 5.5 and 5.6, we highlight how the vortex in the magnetic case pushes the maximum towards larger radius near the onset of convection and twelve times beyond it.

5.3.3 Scaling for the zonal flow

In this section, we show the scaling recovered for the local maximum of the azimuthal wind from our experimental results and we compare it to the scaling originated in [6] and improved in [21] and [22] with a dependence to the Prandtl number. On figure 5.7, we plot the Rossby number with respect to the Rayleigh

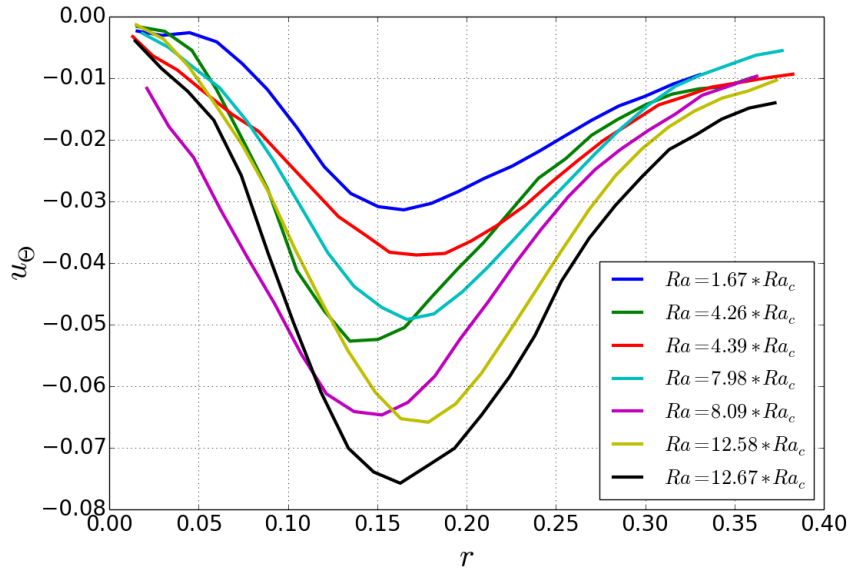

(a) $E = 1.15 \times 10^{-5}$ and $\Lambda = 0.33$

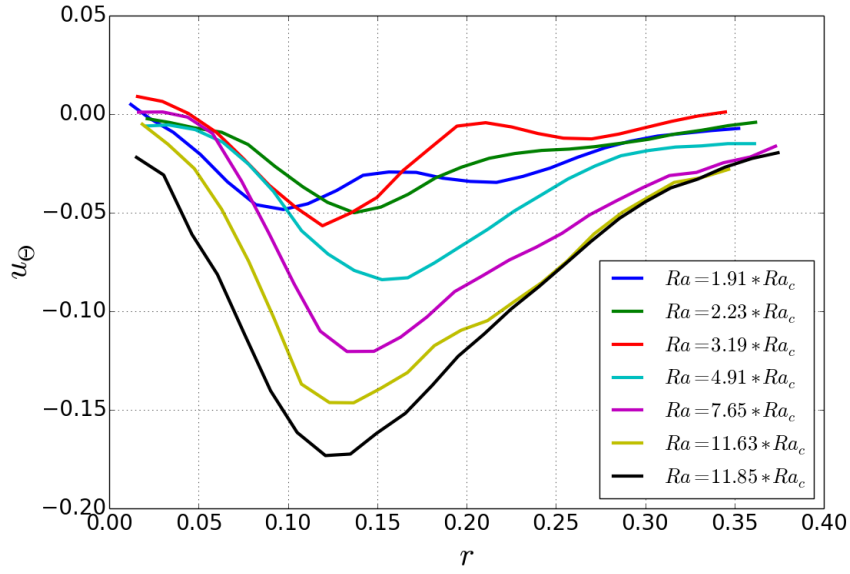

(b) $E = 6.36 \times 10^{-6}$ and $\Lambda = 0.15$

Figure 5.4: Average along θ of the time average θ-component of the velocity in dm/s as a function of r normalized by the diameter of the heater

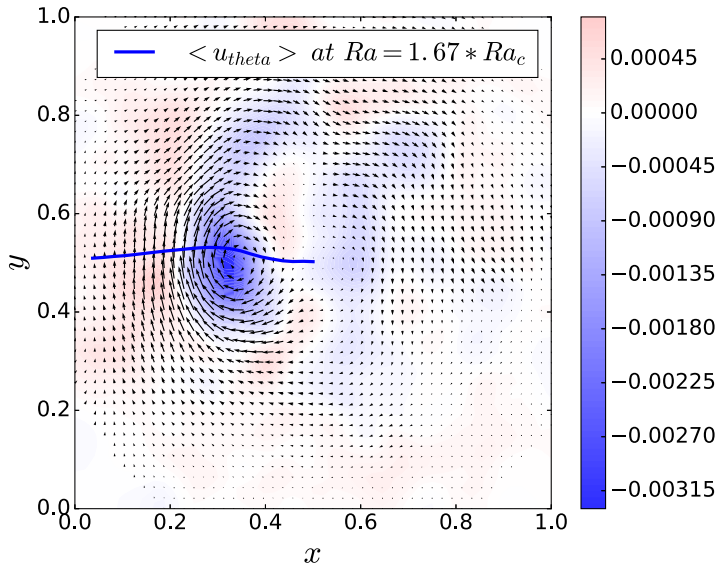

Figure 5.5: Average velocity fields (arrows) with vorticity field (colorbar) in the horizontal plane with $E = 1.15 \times 10^{-5}$ and $\Lambda = 0.33$ at $Ra = 1.67 \times Ra_c$. Superposed with average along θ of the time average θ-component of the velocity in dm/s as a function of r normalized by the diameter of the heater

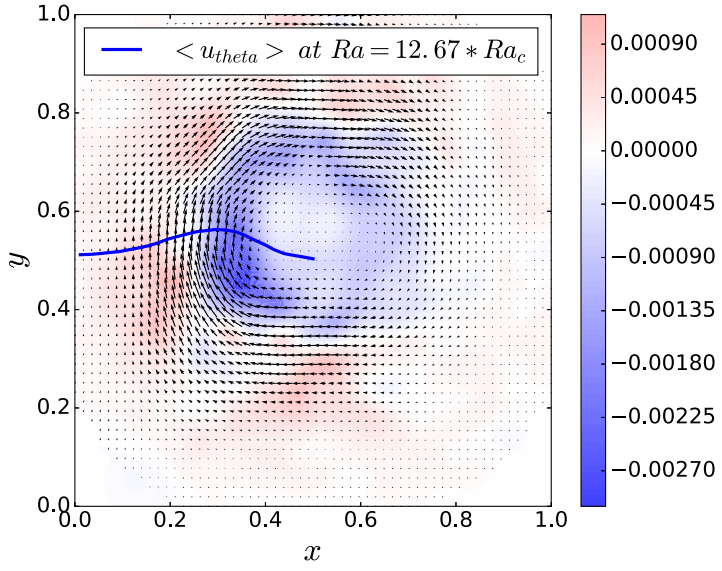

Figure 5.6: Average velocity fields (arrows) with vorticity field (colorbar) in the horizontal plane with $E = 1.15 \times 10^{-5}$ and $\Lambda = 0.33$ at $Ra = 12.67 \times Ra_c$. Superposed with average along θ of the time average θ-component of the velocity in dm/s as a function of r normalized by the diameter of the heater

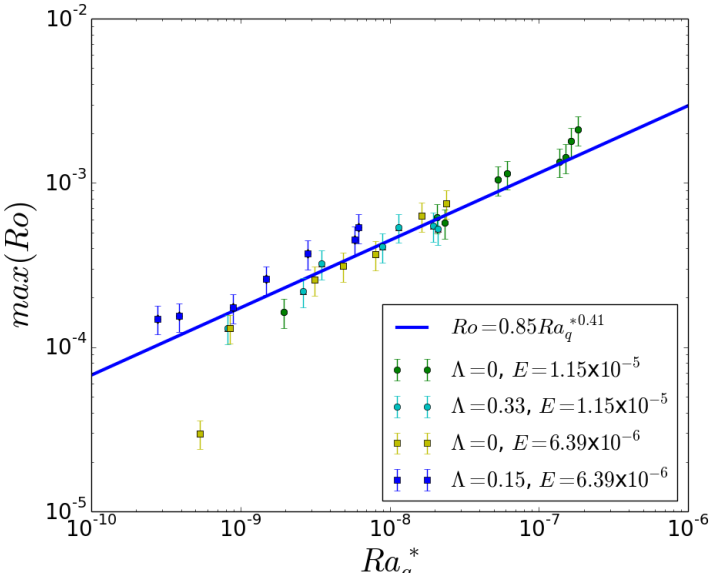

Figure 5.7: Scaling between the Rossby number based on the max of u_θ and the Rayleigh number normalized by the critical Rayleigh number (in plane theory)

number Ra_Q^*. The Rossby number is defined as:

$$Ro = \frac{U}{Lf}, \tag{5.7}$$

where U is characteristic velocity of the flow, L is a significant length in the system (here we used the diameter of the heater) and f is the frequency of Coriolis. Therefore the Rossby number is a measure of the role of inertia over the Coriolis force. A flow dominated by the Coriolis forces will be characterized by a small Rossby number. The scaling was derived by [21] and confirmed experimentally by [6]. This scaling is of the form $Ro \sim Ra_Q^{*0.4}$. A former form of the scaling was derived on the amplitude of the θ-component of the velocity by [6]. Their argument arises first from [16] and is based on the conservation of potential vorticity in columnar flows. On figure 5.7, we were able to recover the scaling derived by [6].

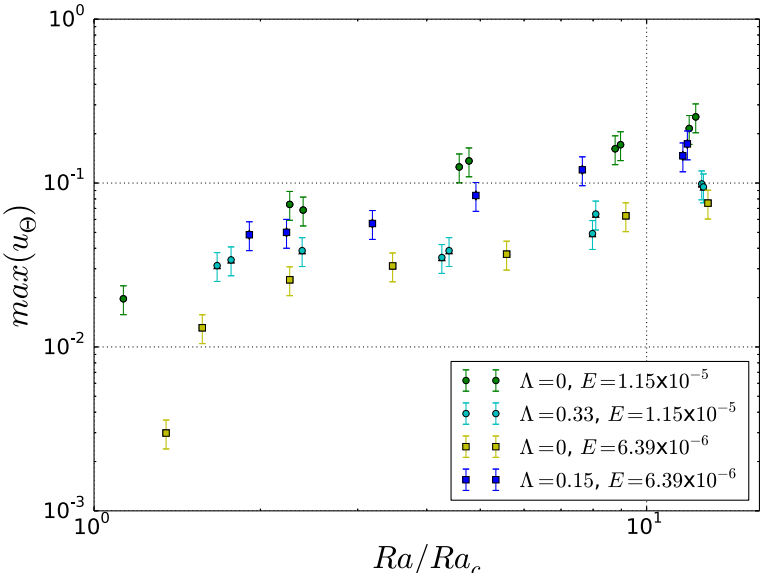

Figure 5.8: u_θ with respect to the modified Rayleigh number

In the previous scaling, the effects of the magnetic field are hidden by the choice of non-dimensional numbers. Therefore, on figure 5.8, we illustrate the behaviour of the maximum of u_θ with respect to the factor of criticality of the system. Interestingly we observe two types of behaviours. The magnetic field either damps (points with $\Lambda = 0.33$) or enhances the zonal flow (points with $\Lambda = 0.15$). The enhancement of the zonal flow confirms the results obtained by [56]. We cannot yet conclude on these two behaviours as we need more points to find out the exact regimes of parameters they correspond to and their exact border in the $E - \Lambda$ plane.

5.4 Polar vortex

In this third section we discuss the Polar Vortex and the relevance of our results to it. The existence of the Polar vortex was first deduced from magnetic measurements by satellites orbiting the Earth [36]. In this study, the authors were able to show the presence of a specific feature of the magnetic field in

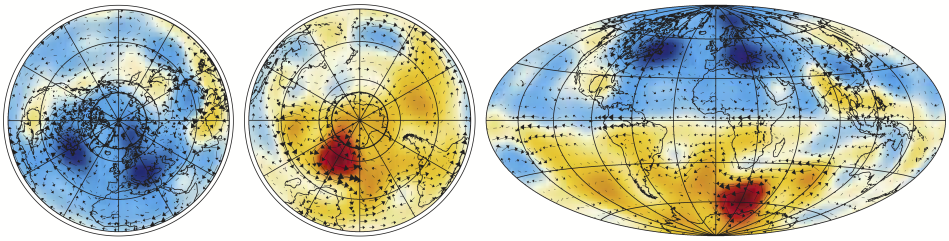

Figure 5.9: Results obtained by [36] for the total core surface flow in 1990. From left to right: North pole, South pole and side view of the Earth. The authors presented anomalies within the Earth Tangent Cylinder.

the Earth Tangent Cylinder under the south and the north pole. Their results highlight a persistent deficit in radial magnetic field near the North pole and the South pole, which the authors attribute to the presence of a large off-center vortex in the Earth polar regions. These two vortices are off-axis and rotating clockwise in the northern hemisphere and anti clockwise in the southern hemisphere. The southern vortex sits below Africa and the northern vortex is located underneath the East coast of Canada. These vortices appear to be embedded in a strong westward flow. The last interesting feature concerning these vortices and emphasized in [36] is their drift approximately evaluated at 0.9° per year and their maximum velocity calculated is around 65km/y. On figure 5.9, we show the results observed by [36].

As we observed in Chapter 4, when the magnetic field is present our measurements in the horizontal plane show only very few convective structures in the upper part of the Tangent Cylinder. With figures 5.10 and 5.11, we show the results we obtained in the horizontal plane with $E = 1.15 \times 10^{-5}$ and $\Lambda = 0.33$ in our least and most supercritical cases. In both cases we clearly observe the presence of a single counterrotating vortex above the Tangent Cylinder present throughtout the range of supercritical regimes we investigated. Therefore our results show some similarity with the geophysical data.

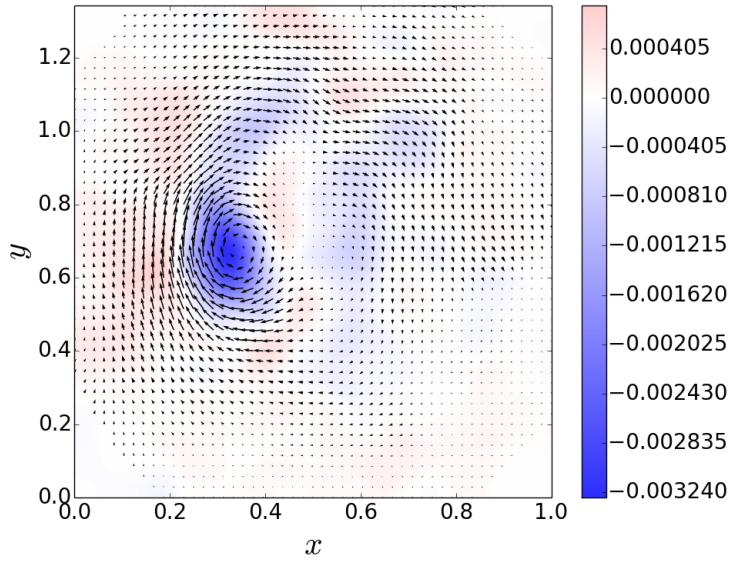

Figure 5.10: Average velocity fields (arrows) with vorticity field (colorbar) in the horizontal plane with $E = 1.15 \times 10^{-5}$ and $\Lambda = 0.33$ at $Ra = 1.67 \times Ra_c$.

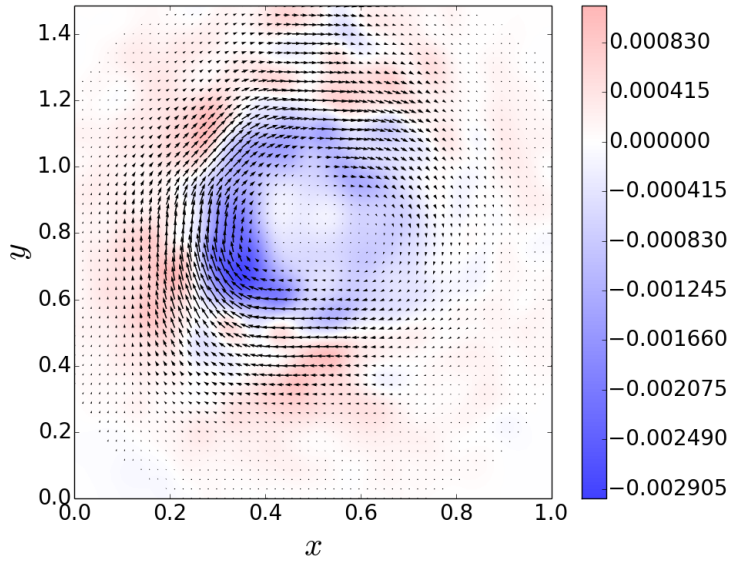

Figure 5.11: Average velocity fields (arrows) with vorticity field (colorbar) in the horizontal plane with $E = 1.15 \times 10^{-5}$ and $\Lambda = 0.33$ at $Ra = 12.67 \times Ra_c$.

To try to confirm further these observations we investigated the maximum velocity within the polar vortex in our system and translated it to what would be the corresponding data in a system of the size of the Earth based on a time scale of $1/\Omega$. In the case with $Ra = 1.67 \times Ra_c$ we measured a maximum velocity that corresponds to 6.46km/y. In the second case with $Ra = 12.67 \times Ra_c$, we recovered a velocity of 12.92km/y. We give the values in km/y to be easily comparable to [36] Both values are well below those measured by [36]. Nonetheless we can still roughly evaluate the criticality we would need to achieve in the experiment to obtain velocity close to the Earth's velocity. On one hand, we can assume that the maximum velocity is linked to the intensity of the zonal flow which seems reasonable as the Polar Vortex is embedded in the zonal flow. On the other hand, we can use [6]'s scaling for the velocity of the zonal flow $u \sim Ra^{2/5}$ assuming it holds for large enough range of parameters. By applying it to our values of the velocity we can estimate the criticality we would require in the experiment to obtain the same magnitude as in the Earth. We found that we would need to have a factor of criticality between 20 and 30 with $E = 1.15 \times 10^{-5}$ and $\Lambda = 0.33$.

Our last point concerning the Polar Vortex is its drift. Our results correspond to early results as our campaigns of measurements were not initially designed to chase the drift of the polar vortex. On figure 5.12, we present the displacement of the center of the vortex in the Tangent Cylinder. These results are extracted from the case presented on figure 5.10. Indeed in this case with $E = 1.15 \times 10^{-5}$, $\Lambda = 0.33$ and $Ra = 1.67 \times Ra_c$, we calculated averages every 25 seconds and looked at the position of the center of the vortex. Based on these preliminary results we recovered an eastward drift of 13° angle per year. Therefore, the polar vortex observed in our system does not behave in the same way as the Earth Polar Vortex [36]. Indeed, our vortex rotates in

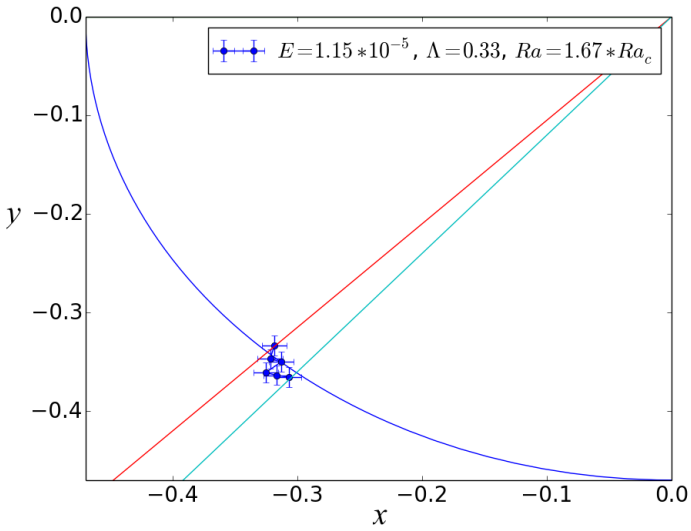

Figure 5.12: Position of the vortex center with $E = 1.15 \times 10^{-5}$ and $\Lambda = 0.33$ at $Ra = 1.67 \times Ra_c$. The red and light blue lines highlight the angular displacement of our vortex.

the opposite direction and around thirteen times faster. These result needs to be confirmed by much longer acquisition in time. At the moment, we are averaging over approximately a year in real time. Additionally, we would need to investigate the problem by varying the value on the Elsasser number and Ekman number as we showed earlier that the magnetic field can have either an enhancing or a damping effect on the zonal flow.

5.5 Conclusion

In this Chapter, we linked our results to geophysical questions. Our points of interest were the heat transfer through the Tangent Cylinder, the polar vortex and the zonal flow. Concerning the heat transfer, we were able to recover the scaling of [58] $Nu^* \sim Ra_Q^{*0.29}$. Interestingly, by using the classical definition of the Rayleigh number and the Nusselt number, our results showed the effect of the magnetic field. Indeed we obtained $Nu \sim Ra^{2/5}$ and $Nu \sim Ra^{2/3}$ without

and with magnetic field respectively. Concerning the Polar vortex, we showed that with a sufficiently strong magnetic field the flow is ruled by a single off-axis vortex very similar to the Polar Vortex reported by [36]. This corresponds to our knowledge to the first experimental evidence of a Polar vortex in a configuration close to a Tangent Cylinder. Nevertheless the velocities observed in our experiment suggest that we operated with factors of criticality that are too low to reproduce dynamics relevant to the Earth. Additionally, we were unfortunately not able to recover satisfactory results for the drift of the vortex for lack of sufficient data. Finally, we studied the behaviour of the zonal flow in the Tangent Cylinder. Although, we only had access to partial results and not all the velocity field inside the Tangent Cylinder, we were able to recover scaling for the Rossby number and the Rayleigh number such as $max(Ro) \sim Ra_q^{*0.4}$. The scalings for the heat flux and the zonal flow using diffusionless number Nu^* and Ra_q show that these quantities are governed by the available buoyancy, in other word the heat flux. The main effect of the magnetic field is to alter the structure of the flow and therefore the heat flux through the Tangent Cylinder for a given temperature difference at the boundaries.

Chapter 6

Discussion

In Geophysics and Magnetohydrodynamics, a great interest and dedication is devoted to convective flow in rotation permeated by a magnetic field. Up until now, the understanding of dynamo process in celestial body remains a very open question due to the multiple physical effects involved. This challenge comes from the complexity and the diversity of effects involved in the magnetic field generation. In the case of the Earth, the difficulties arise for example from the size of the Earth core, the difficulties to evaluate its composition or the heat flux, the impossibility to have direct measurements of the flow in the outer core or the vague knowledge of the boundary condition. These questions lead to the impossibility at the moment to have a clear comprehensive picture of the flow inside the outer region of the Earth core. Especially, the question of the nature of the flow, magnetic or viscous, at the onset of convection and above in the Tangent Cylinder was yet to be investigated experimentally. Furthermore, experimental visualizations of the flow with magnetic effects were missing in the literature. The choice made in this dissertation was to compare the magnetic and non-magnetic flow experimentally with a geometry relevant to the Earth Tangent Cylinder. Our aim was to bring a new contribution on the development of convection under high magnetic field with a new experimental approach.

In order to reach and produce new information on the Earth Tangent Cylinder, we built a new experimental setup. It consists in an hemispherical dome filled with sulphuric acid heated on the inside, cooled on the outside and spun in a high magnetic field. The novelty of our experiment was to use highly concentrated electrolyte to generate MHD effects and to allow for particle image velocimetry measurements at the same time. The size of the apparatus (approximately 30 cm in diameter) and the rotation rate 1 rps authorized us to explore regimes of the order of $E \sim 10^{-6}$, $Ra \in [Ra_c, 12 \times Ra_c]$ and $\Lambda \in [0, 1]$. Therefore our experimental setup opens new opportunities for the magnetohydrodynamic community as well as the geophysics community. Indeed by using concentrated electrolyte instead off liquid metal, we contributed to a new way to study magnetohydrodynamic flows allowing for traditional hydrodynamic measurement technics such as particle image velocimetry. Likewise by having a setup operating in a relevant parameter and with the right geometry, we were able to study geophysically relevant phenomena such as the planetary heat flux, the polar vortex or the thermal wind.

Using this new apparatus, the original point of this work was to study the onset of convection only and to compare the effect with and without magnetic field. Nevertheless with this dissertation, we chose to clarify the convection at onset and beyond under rotation with and without magnetic field in the Tangent Cylinder (see Chapter 4). Without magnetic field, we were able to show that the convection in the Tangent Cylinder does not behave as in a plane layer geometry only. In [64], the authors showed that the aspect ratio of the cylinder plays an important role in the way the convection behave at onset and depart from it. With our work we were able to bridge between our results

and the work from [8] and [64]. Specifically, we showed that convection in the Tangent Cylinder resembles to that in a cylinder with solid walls at its lateral boundaries. This emphasizes the crucial influence of the Taylor-Proudmann constraint on the structure of the convection in the Tangent Cylinder. Equally beyond the onset of convection our study and these two former studies were linked to describe the different stages that occur as the convection goes further and further away from its onset. With magnetic field, we showed the first laboratory results for the Tangent Cylinder. These results showed significant evidence of the effect of the magnetic field. We observed that the number of convective structures is greatly affected resulting in one main off-axis vortex stretching within the Tangent Cylinder. In Chapter 5 we explored the geophysical implications of our work. Concerning the heat flux throughout the tangent cylinder, we verified the empirical scaling law of $Nu \sim Ra^{2/5}$ without magnetic field and we showed that this law changes to $Nu \sim Ra^{2/3}$ with the magnetic field. Generally, we recovered scalings corresponding to [58]: $Nu^* \sim (Ra_Q^*)^{1/3}$. Similarly, we confirmed the results obtained by King & Aurnou [38] who found that the magnetic field either enhances or suppresses the convection depending on the value of the Elsasser number. Concerning the flow patterns, we showed that the magnetic field tends to organize the flow around one large vortex. This feature is very similar to the so called Polar Vortex although we have not yet been able to show regimes where the Polar Vortex drifts in the same way as it does in the Earth core. Finally concerning the zonal flow, we showed that we were recovering the classical behaviour for non-magnetic case. With the magnetic field we observed evidences of different regimes enhancing or damping the azimuthal velocity. Nevertheless we recovered the scaling for the Rossby number with respect to the Rayleigh number: $Ro \sim (Ra_Q^*)^{0.4}$.

As a last point on our work, we would like to emphasize that the depth and the interest of the subject only lead to the perspective of new studies. For example, it would have been exciting to investigate the flow at the upper boundary of the Tangent Cylinder, this would give us results easily comparable with geophysical data. Another idea that we hope will be pursued, would be to use particles that change color with the surrounding temperature. Although this would be challenging it would represent a very promising insight on the temperature field within the bulk of the Tangent Cylinder. These ideas are mainly technical. From a more theoretical point of view, it seems necessary to find an answer to the degree of criticality of the Earth core and evaluate the type of regimes this corresponds to.

Finally, we note that the theoretical aspect of this dissertation was published last year in *Physics of fluids* and the experimental setup was published this year in *Review of Scientific Instruments*. Both papers can be found in the Annex of the present dissertation.

Bibliography

[1] D. J. Acheson and R. Hide. Hydromagnetics of rotating fluids. *Reports on Progress in Physics*, 36:159–221, Feb. 1973.

[2] T. Alboussiere, J. Garandet, and R. Moreau. Asymptotic analysis and symmetry in mhd convection. *Physics of Fluids*, 8(8):2215–2226, 1996.

[3] O. Andreev, Y. Kolesnikov, and A. Thess. Visualization of the ludford column. *Journal of Fluid Mechanics*, 721:438–453, 2013.

[4] O. Andreev, A. Thess, and C. Haberstroh. Visualization of magnetoconvection. *Physics of Fluids*, 15(12):3886–3889, 2003.

[5] J. Aubert. Steady zonal flows in spherical shell dynamos. *Journal of Fluid Mechanics*, 542:53–67, 2005.

[6] J. Aubert, D. Brito, H.-C. Nataf, P. Cardin, and J.-P. Masson. A systematic experimental study of rapidly rotating spherical convection in water and liquid gallium. *Physics of the Earth and Planetary Interiors*, 128(1):51–74, 2001.

[7] J. Aurnou. Planetary core dynamics and convective heat transfer scaling. *Geophysical and Astrophysical Fluid Dynamics*, 101(5-6):327–345, 2007.

[8] J. Aurnou, S. Andreadis, L. Zhu, and P. Olson. Experiments on convection in Earth's core tangent cylinder. *Earth and Planetary Science Letters*, 212(1):119–134, 2003.

[9] J. Aurnou, D. Brito, and P. Olson. Anomalous rotation of the inner core and the toroidal magnetic field. *Journal of Geophysical Research: Solid Earth*, 103(B5):9721–9738, 1998.

[10] J. M. Aurnou and P. L. Olson. Experiments on Rayleigh–Bénard convection, magnetoconvection and rotating magnetoconvection in liquid gallium. *Journal of Fluid Mechanics*, 430:283–307, 2001.

[11] J. Boussinesq. *Théorie de l'écoulement tourbillonnant et tumultueux des liquides dans les lits rectilignes à grande section*, volume 1. Gauthier-Villars, 1897.

[12] S. I. Braginsky and P. H. Roberts. Equations governing convection in earth's core and the geodynamo. *Geophysical & Astrophysical Fluid Dynamics*, 79(1-4):1–97, 1995.

[13] U. Burr and U. Müller. Rayleigh–Bénard convection in liquid metal layers under the influence of a vertical magnetic field. *Physics of Fluids*, 13(11):3247–3257, 2001.

[14] F. H. Busse. Thermal instabilities in rapidly rotating systems. *Journal of Fluid Mechanics*, 44(03):441–460, 1970.

[15] F. H. Busse and R. M. Clever. Stability of convection rolls in the presence of a vertical magnetic field. *Physics of Fluids*, 25(6):931–935, 1982.

[16] P. Cardin and P. Olson. Chaotic thermal convection in a rapidly rotating spherical shell: consequences for flow in the outer core. *Physics of the earth and planetary interiors*, 82(3-4):235–259, 1994.

[17] C. R. Carrigan and F. H. Busse. An experimental and theoretical investigation of the onset of convection in rotating spherical shells. *Journal of Fluid Mechanics*, 126:287–305, 1983.

[18] B. Castaing, G. Gunaratne, F. Heslot, L. Kadanoff, A. Libchaber, S. Thomae, X.-Z. Wu, S. Zaleski, and G. Zanetti. Scaling of hard thermal turbulence in rayleigh-bénard convection. *Journal of Fluid Mechanics*, 204:1–30, 1989.

[19] S. Chandrasekhar. *Hydrodynamic and hydromagnetic stability*. Clarendon Press, Oxford, 1961.

[20] A. Chiffaudel, S. Fauve, and B. Perrin. Viscous and inertial convection at low prandtl number: Experimental study. *EPL (Europhysics Letters)*, 4(5):555, 1987.

[21] U. Christensen. Zonal flow driven by strongly supercritical convection in rotating spherical shells. *Journal of Fluid Mechanics*, 470:115–133, 2002.

[22] U. Christensen and J. Aubert. Scaling properties of convection-driven dynamos in rotating spherical shells and application to planetary magnetic fields. *Geophysical Journal International*, 166(1):97–114, 2006.

[23] S. Cioni, S. Chaumat, and J. Sommeria. Effect of a vertical magnetic field on turbulent Rayleigh–Bénard convection. *Physical Review E*, 62(4):R4520, 2000.

[24] H. Darling. Conductivity of sulfuric acid solutions. *Journal of Chemical & Engineering Data*, 9(3):421–426, 1964.

[25] P. A. Davidson. *An introduction to magnetohydrodynamics*, volume 25. Cambridge university press, 2001.

[26] P. A. Davidson. *Turbulence in Rotating, Stratified and Electrically Conducting Fluids*. Cambridge University Press, 2013.

[27] I. A. Eltayeb. Hydromagnetic convection in a rapidly rotating fluid layer. *Proceedings of the Royal Society A*, 326(1565):229–254, 1972.

[28] I. A. Eltayeb and S. Kumar. Hydromagnetic convective instability of a rotating, self-gravitating fluid sphere containing a uniform distribution of heat sources. *Proceedings of the Royal Society A*, 353(1673):145–162, 1977.

[29] I. A. Eltayeb and P. H. Roberts. On the hydromagnetics of rotating fluids. In A. M. Soward, editor, *Magnetohydrodynamics and the Earth's Core: Selected Works of Paul Roberts*, volume 162, page 229. CRC Press, 2002.

[30] D. Fearn. Thermally driven hydromagnetic convection in a rapidly rotating sphere. *Proceedings of the Royal Society A*, 369(1737):227–242, 1979.

[31] C. C. Finlay and A. Jackson. Equatorially dominated magnetic field change at the surface of earth's core. *Science*, 300(5628):2084–2086, 2003.

[32] G. A. Glatzmaier and P. H. Roberts. Rotation and magnetism of earth's inner core. *Magnetohydrodynamics and the Earth's Core: Selected Works by Paul Roberts*, page 141, 2002.

[33] H. Goldstein, E. Knobloch, I. Mercader, and M. Net. Convection in a rotating cylinder. part 1 linear theory for moderate prandtl numbers. *Journal of Fluid Mechanics*, 248:583–604, 1993.

[34] R. Hide and P. Roberts. The origin of the main geomagnetic field. *Physics and Chemistry of the Earth*, 4:27–98, 1961.

[35] B. C. Houchens, L. Witkowski, and J. S. Walker. Rayleigh–Bénard instability in a vertical cylinder with a vertical magnetic field. *Journal of Fluid Mechanics*, 469:189–207, 2002.

[36] G. Hulot, C. Eymin, B. Langlais, M. Mandea, and N. Olsen. Small-scale structure of the geodynamo inferred from Oersted and Magsat satellite data. *Nature*, 416(6881):620–623, 2002.

[37] D. Jault, C. Gire, and J. Le Mouël. Westward drift, core motions and exchanges of angular momentum between core and mantle. *Nature*, 333(6171):353–356, 1988.

[38] E. M. King and J. M. Aurnou. Magnetostrophic balance as the optimal state for turbulent magnetoconvection. *Proceedings of the National Academy of Sciences*, 112(4):990–994, 2015.

[39] R. H. Kraichnan. Turbulent thermal convection at arbitrary prandtl number. *Physics of Fluids (1958-1988)*, 5(11):1374–1389, 1962.

[40] A. Kulikovskii. Flows of a conducting incompressible liquid in an arbitrary region with a strong magnetic field. *Fluid Dynamics*, 8(3):462–467, 1973.

[41] T. Lay, Q. Williams, and E. J. Garnero. The core–mantle boundary layer and deep earth dynamics. *Nature*, 392(6675):461–468, 1998.

[42] S. McEnroe, L. Brown, and P. Robinson. Earth analog for martian magnetic anomalies: remanence properties of hemo-ilmenite norites in the bjerkreim-sokndal intrusion, rogaland, norway. *Journal of Applied Geophysics*, 56(3):195–212, 2004.

[43] Y. Nakagawa. Experiments on the instability of a layer of mercury heated from below and subject to the simultaneous action of a magnetic field and rotation. *Proceedings of the Royal Society A*, 242(1228):81–88, 1957.

[44] P. Olson. Laboratory experiments on the dynamics of the core. *Physics of the Earth and Planetary Interiors*, 187(1):1–18, 2011.

[45] M. Ozisik. *Heat Conduction*. Wiley, New York, 1980.

[46] A. Pais and G. Hulot. Length of day decade variations, torsional oscillations and inner core superrotation: evidence from recovered core surface zonal flows. *Physics of the Earth and Planetary Interiors*, 118(3):291–316, 2000.

[47] O. Podvigina. Stability of rolls in rotating magnetoconvection in a layer with no-slip electrically insulating horizontal boundaries. *Physical Review E*, 81(5):056322, 2010.

[48] M. Raffel, C. Willert, J. Kompenhans, et al. *Particle image velocimetry: a practical guide*. Springer, 2013.

[49] P. H. Roberts. Magnetoconvection in a rapidly rotating fluid. In P. H. Roberts and A. M. Soward, editors, *Rotating Fluids in Geophysics*, pages 421–435. Academic Press, 1978.

[50] P. H. Roberts and E. M. King. On the genesis of the Earth's magnetism. *Reports on Progress in Physics*, 76(9):096801, 2013.

[51] P. H. Roberts and K. Zhang. Thermal generation of Alfvén waves in oscillatory magnetoconvection. *Journal of Fluid Mechanics*, 420:201–223, 2000.

[52] G. Rüdiger and R. Hollerbach. *The Magnetic Universe: Geophysical and Astrophysical Dynamo Theory*. John Wiley & Sons, 2006.

[53] P. J. Schmid and D. S. Henningson. *Stability and transition in shear flows*. Springer, 2001.

[54] G. Schubert and K. Soderlund. Planetary magnetic fields: Observations and models. *Physics of the Earth and Planetary Interiors*, 187(3):92–108, 2011.

[55] B. Sreenivasan and C. A. Jones. Structure and dynamics of the polar vortex in the earth's core. *Geophysical Research Letters*, 32:L20301, 2005.

[56] B. Sreenivasan and C. A. Jones. Azimuthal winds, convection and dynamo action in the polar regions of planetary cores. *Geophysical & Astrophysical Fluid Dynamics*, 100(4-5):319–339, 2006.

[57] B. Sreenivasan and C. A. Jones. Helicity generation and subcritical behaviour in rapidly rotating dynamos. *Journal of Fluid Mechanics*, 688:5–30, 2011.

[58] I. Sumita and P. Olson. Experiments on highly supercritical thermal convection in a rapidly rotating hemispherical shell. *Journal of Fluid Mechanics*, 492:271–287, 2003.

[59] M. Takashima, M. Hirasawa, and H. Nozaki. Buoyancy driven instability in a horizontal layer of electrically conducting fluid in the presence of a

vertical magnetic field. *International Journal of Heat and Mass Transfer*, 42(9):1689–1706, 1999.

[60] M. P. Volz and K. Mazuruk. Thermoconvective instability in a rotating magnetic field. *International Journal of Heat and Mass Transfer*, 42(6):1037–1045, 1999.

[61] S. A. Wilde, J. W. Valley, W. H. Peck, and C. M. Graham. Evidence from detrital zircons for the existence of continental crust and oceans on the earth 4.4 gyr ago. *Nature*, 409(6817):175–178, 2001.

[62] T. Yanagisawa, Y. Hamano, T. Miyagoshi, Y. Yamagishi, Y. Tasaka, and Y. Takeda. Convection patterns in a liquid metal under an imposed horizontal magnetic field. *Physical Review E*, 88(6):063020, 2013.

[63] K. Zhang and G. Schubert. Magnetohydrodynamics in rapidly rotating spherical systems. *Annual Review of Fluid Mechanics*, 32(1):409–443, 2000.

[64] F. Zhong, R. Ecke, and V. Steinberg. Asymmetric modes and the transition to vortex structures in rotating rayleigh-bénard convection. *Physical Review Letters*, 67(18):2473, 1991.

[65] F. Zhong, R. E. Ecke, and V. Steinberg. Rotating rayleigh–bénard convection: asymmetric modes and vortex states. *Journal of Fluid Mechanics*, 249:135–159, 1993.

Part III

Appendixes and Annexes

Chapter 7

Derivation of the inhomogeneous model

In this chapter, we show how to linearize the equations in the case of an inhomogeneous fluid. Starting form the eqs.[2.4-2.8] and following [19], we derive five new equations as follow.

First equation: the z-component of the curl of eq.[2.4] As we take the curl and consider stationarity, we can write eq.[2.4] without the inertial term, and the pressure term:

$$2\hat{\mathbf{z}} \times \mathbf{u} = RaT + \Lambda(\boldsymbol{\nabla} \times \mathbf{B}) \times \mathbf{B} + E\nabla^2\mathbf{u}, \tag{7.1}$$

The first term coming from the Coriolis force becomes:

$$2\boldsymbol{\nabla} \times (\hat{\mathbf{z}} \times \mathbf{u}) = -\frac{\partial \mathbf{u}}{\partial z}, \tag{7.2}$$

So the z-component is: $-2Du_z$. For the second term, the z-component is:

$$\boldsymbol{\nabla} \times (RaT).\mathbf{e_z} = 0. \tag{7.3}$$

For the third term, we keep in mind that in non-dimensional units $\boldsymbol{\nabla} \times \mathbf{B} = \mathbf{J}$ and that we only carry the first order terms. Then we write:

$$\boldsymbol{\nabla} \times (\Lambda(\boldsymbol{\nabla} \times \mathbf{B}) \times \mathbf{B}) = \Lambda \boldsymbol{\nabla} \times (\mathbf{J} \times \mathbf{B}). \tag{7.4}$$

The z-component is then:

$$\Lambda B_0 (\frac{\partial j_x}{\partial x} + \frac{\partial j_y}{\partial y}). \tag{7.5}$$

As the divergence of $\mathbf{J}$ is zero and B_0 is considered equal to 1, we write: $\Lambda D j_z$ In the last term, we use $\boldsymbol{\nabla} \times \mathbf{u} = \omega$, therefore it becomes:

$$E\nabla^2 \mathbf{u} = E\nabla^2(\boldsymbol{\nabla} \times \omega), \tag{7.6}$$

which is: $E(D^2 - a^2)\omega_z$ with our notation. The remaining terms form the following equation:

$$E(D^2 - a^2)\hat{\omega_z} + 2D\hat{u_z} + \Lambda D\hat{j_z} = 0 \tag{7.7}$$

Second equation: the z-component of the curl of the curl of eq.[2.4]

In the light of the above, we look at the curl of the curl of:

$$2\hat{\mathbf{z}} \times \mathbf{u} = RaT + \Lambda(\boldsymbol{\nabla} \times \mathbf{B}) \times \mathbf{B} + E\nabla^2 \mathbf{u}, \tag{7.8}$$

The first is express as:

$$2\boldsymbol{\nabla} \times \boldsymbol{\nabla} \times (\hat{\mathbf{z}} \times \mathbf{u}) = -\frac{\partial \boldsymbol{\nabla} \times \mathbf{u}}{\partial z} = -\frac{\partial \omega}{\partial z}, \tag{7.9}$$

which becomes: $-2D\omega_z$ with our notation. The second term is defined as:

$$\boldsymbol{\nabla} \times \boldsymbol{\nabla} \times (RaT).\mathbf{e_z} = -(\frac{\partial^2 T'}{\partial x^2} + \frac{\partial^2 T'}{\partial y^2}), \tag{7.10}$$

which is: $-Raa^2T'$ with our notations. Keeping in mind that $\boldsymbol{\nabla} \times \boldsymbol{\nabla} \times (\mathbf{B}) = -\nabla^2 B$, the third term is expressed as:

$$\boldsymbol{\nabla} \times \boldsymbol{\nabla} \times (\Lambda(\boldsymbol{\nabla} \times \mathbf{B}) \times \mathbf{B}) = \Lambda B_0 \boldsymbol{\nabla} \times (\frac{\partial \mathbf{J}}{\partial z}) = \Lambda B_0 (\frac{\partial \nabla^2 \mathbf{B}}{\partial z}), \tag{7.11}$$

which is: $\Lambda B_0(D^2 - a^2)Db_z$ with our notations. Lastly, the fourth term is derived as:

$$\boldsymbol{\nabla} \times \boldsymbol{\nabla} \times (\nabla^2 \mathbf{u}) = \nabla^2(\boldsymbol{\nabla} \times \boldsymbol{\nabla} \times \mathbf{u}) = -\nabla^2 \nabla^2 \mathbf{u}, \tag{7.12}$$

which becomes: $(D^2 - a^2)^2 u_z$. It follows the remaining equation:

$$-2D\omega_z - Raa^2T' + E(D^2 - a^2)^2 u_z + \Lambda B_0(D^2 - a^2)Db_z = 0, \tag{7.13}$$

Interestingly, we note that the inhomogeneous model does not change the first two equations compared to the classic case.

Third equation: the z-component of eq.[2.5] Again, we consider the flow stationary hence the induction equation becomes:

$$\boldsymbol{\nabla} \times (\mathbf{u} \times \mathbf{B}) + \eta(T)\nabla^2 \mathbf{B} + \nabla\Sigma \times \frac{\boldsymbol{\nabla} \times \mathbf{B}}{\Sigma^2} = 0, \tag{7.14}$$

Having in mind that the divergence of $\mathbf{u} = 0$, we can write the z-component of the first term as:

$$\boldsymbol{\nabla} \times (\mathbf{u} \times \mathbf{B}).\mathbf{e_z} = B_0 \frac{\partial u_z}{\partial z}, \tag{7.15}$$

which is $B_0 D u_z$ with our notations. The second term, the diffusion term, without the non-linear terms naturally produces: $\eta(T)(D^2 - a^2)b_z$. And the third term remains void, indeed as Σ is only along the z-direction so the cross product is zero in the z-component. So the final form of our third equation is:

$$\eta(T)(D^2 - a^2)b_z + B_0 D u_z = 0 \tag{7.16}$$

Fourth equation: the z-component of the curl of eq.[2.5] Following the same logic, we start with:

$$\boldsymbol{\nabla} \times (\mathbf{u} \times \mathbf{B}) + \eta(T)\nabla^2 \mathbf{B} + \nabla\Sigma \times \frac{\boldsymbol{\nabla} \times \mathbf{B}}{\Sigma^2} = 0, \tag{7.17}$$

Remembering that the curl of $\mathbf{u}$ is ω and the curl of $\mathbf{B}$ is $\mathbf{J}$ modulo μ_0, the first two terms becomes:

$$\mathbf{e_z}.(\boldsymbol{\nabla} \times (\boldsymbol{\nabla} \times (\mathbf{u} \times \mathbf{B}))) = B_0 \frac{\partial \omega_z}{\partial z}, \tag{7.18}$$

which is $B_0 D\omega_z$ with our notation, and $\eta(T)(D^2 - a^2)j_z$. The third term is then:

$$\boldsymbol{\nabla} \times (\nabla\Sigma \times \frac{\boldsymbol{\nabla} \times \mathbf{B}}{\Sigma^2}).\mathbf{e_z}, \tag{7.19}$$

It can be decomposed into two new terms. The first term can be neglected as we are only interested in the z-component. The second term is then written:

$$(\frac{\nabla\Sigma}{\Sigma^2} \times \boldsymbol{\nabla} \times \mathbf{B}).\mathbf{e_z} = -(\frac{\partial \eta}{\partial T_0}\frac{\partial T_0}{\partial z})(\frac{\partial j_x}{\partial x} + \frac{\partial j_y}{\partial y}), \tag{7.20}$$

which becomes $\frac{d\eta(T)}{dT_0} DT_0 Dj_z$ with our notations and the zero divergence of the current. Ultimately the remaining equation is:

$$B_0 D\omega_z + \eta(T)(D^2 - a^2)j_z + \frac{d\eta(T)}{dT_0} DT_0 Dj_z = 0, \tag{7.21}$$

From eq.[2.6] Finally, we treat the energy equation. Just as previously, we neglect the time-dependent term. Thereafter eq.[2.6] is now written:

$$(\mathbf{u} \cdot \boldsymbol{\nabla})T = PmPr^{-1}\boldsymbol{\nabla}.(\kappa \boldsymbol{\nabla} T), \tag{7.22}$$

The first term (the advection term) is derived neglecting again the non-linear terms and bearing in mind that the basic state of the velocity is zero. It becomes:

$$(\mathbf{u} \cdot \boldsymbol{\nabla})T \sim u_z \boldsymbol{\nabla} T_0, \tag{7.23}$$

which is $u_z DT_0$ with respect to our notations. The second term (the diffusion term) gives an extra term as the thermal diffusivity is dependent of the temperature. Considering the same rescaling of T' and Ra with Pm and Pr, it is written:

$$\boldsymbol{\nabla}.(\kappa \boldsymbol{\nabla} T) = \frac{\partial T'}{\partial z}\left(\frac{\partial \kappa}{\partial T_0}\frac{\partial T_0}{\partial z}\right) + \kappa\left(\frac{\partial^2}{\partial z^2} - a^2\right)T', \tag{7.24}$$

which is with our notations: $\frac{d\kappa}{dT_0} DT_0 DT' + \kappa(D^2 - a^2)T'$. Therefore the remaining equation is:

$$\frac{d\kappa}{dT_0} DT_0 DT' + \kappa(D^2 - a^2)T' + u_z DT_0 = 0. \tag{7.25}$$

For this equation to be true, we need to make sure and assume the $T_0(z)$ satisfies $\boldsymbol{\nabla}.(\kappa \boldsymbol{\nabla} T_0) = 0$. In other words, the basic state should be stationary.

Summary of the final form of the model Finally, assuming $\sigma_i = 0$, this leads to the following five equations with $B_0 = 1$:

$$E(D^2 - a^2)\hat{\omega_z} + 2D\hat{u_z} + \Lambda D\hat{j_z} = 0 \tag{7.26}$$

$$-2D\hat{\omega_z} - Raa^2\hat{T'} + E(D^2 - a^2)^2\hat{u_z} + \Lambda(D^2 - a^2)D\hat{b_z} = 0 \tag{7.27}$$

$$\eta(T)(D^2 - a^2)\hat{b_z} + D\hat{u_z} = 0 \tag{7.28}$$

$$D\hat{\omega_z} + \eta(T)(D^2 - a^2)\hat{j_z} + \frac{d\eta(T)}{dT_0}DT_0D\hat{j_z} = 0 \tag{7.29}$$

$$\frac{d\kappa}{dT_0}DT_0D\hat{T'} + \kappa(D^2 - a^2)\hat{T'} + \hat{u_z}DT_0 = 0 = 0 \tag{7.30}$$

Chapter 8

Article: Onset of plane layer magnetoconvection at low Ekman number

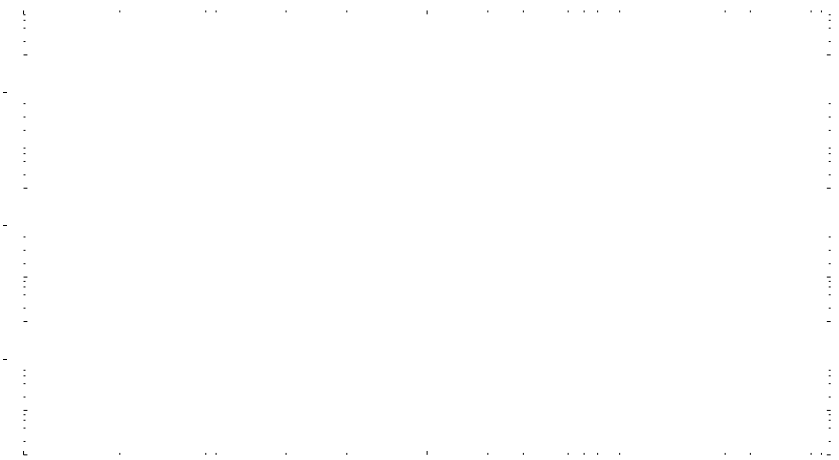

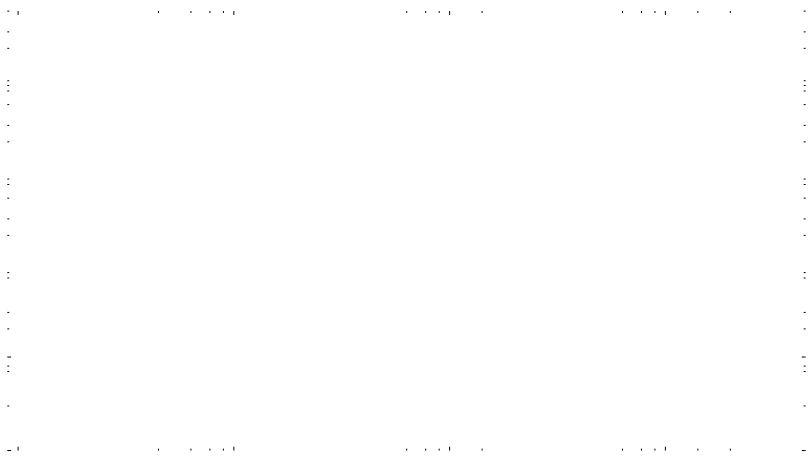

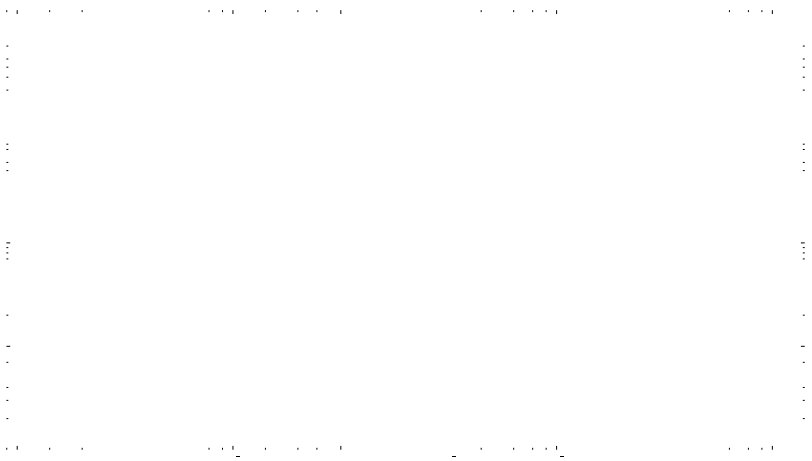

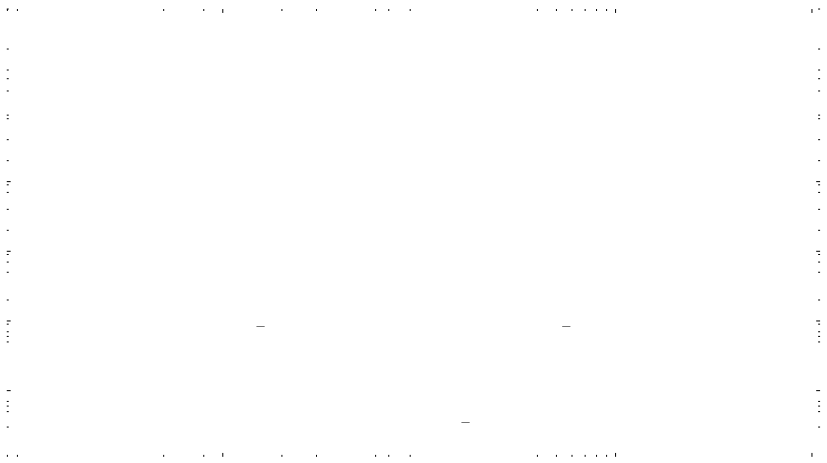

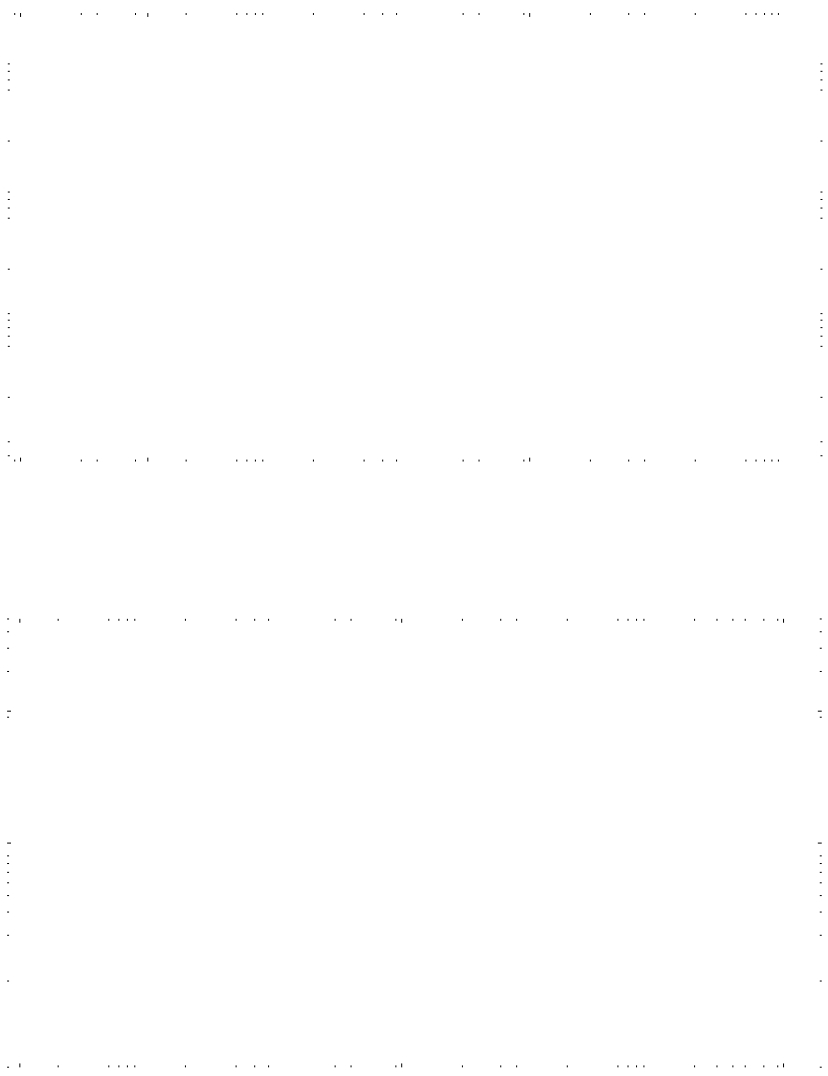

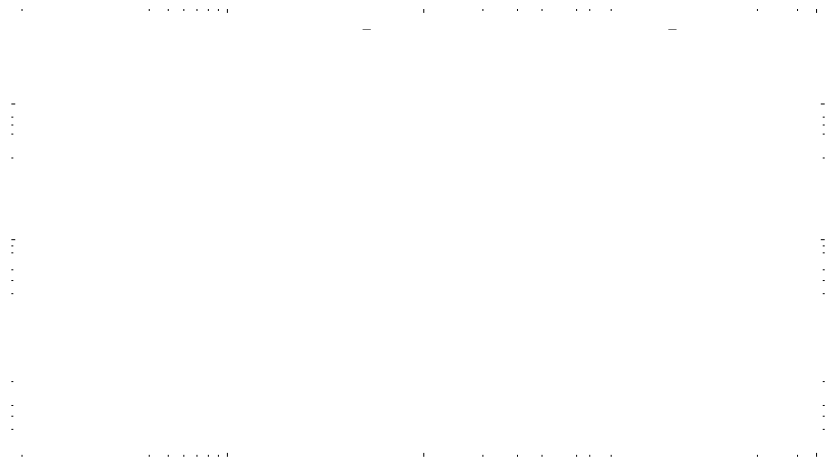

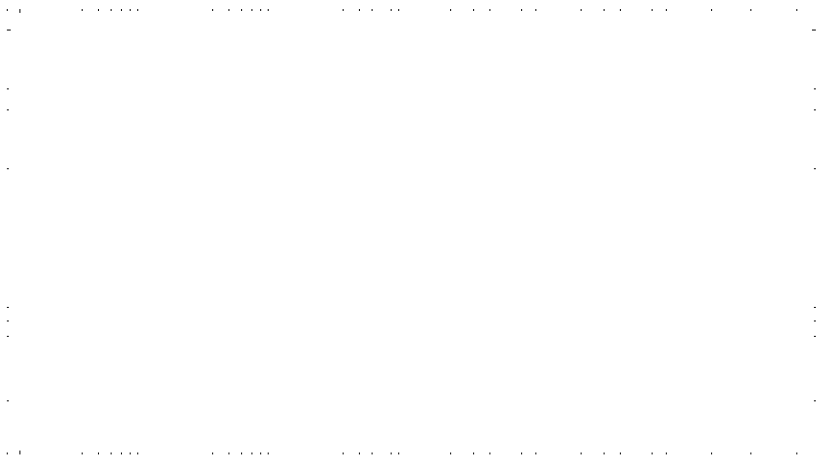

Chapter 9

Article: Little Earth Experiment: an instrument to model planetary cores